

Aus der Klinik für Neurochirurgie
der medizinischen Fakultät
der Universität des Saarlandes, Homburg/Saar
und dem Service National de Neurochirurgie
des Centre Hospitalier, Luxemburg

**„Evaluation der Wertigkeit der Raman-Spektroskopie in Bezug
auf Fixations-Methoden sowie die Unterscheidung verschiedener
Tumoren des menschlichen Nervensystems“**

*„Evaluation of the value of Raman-Spectroscopy in relation to fixation methods
and the differentiation of various tumors of the human nervous system“*

**Dissertation zur Erlangung des Grades eines Doktors der Medizin
der Medizinischen Fakultät
der UNIVERSITÄT DES SAARLANDES
2022**

Vorgelegt von: Giulia Mirizzi
Geboren am 01.05.1996 in Luxemburg

Betreut von: Prof. Dr. med. Frank Hertel

Table of Contents

1	Zusammenfassung	8
2	Introduction.....	12
2.1	Braintumors	12
2.1.1	Classification.....	12
2.1.1.1	Meningiomas.....	13
2.1.1.2	Gliomas.....	15
2.1.1.3	Lymphomas.....	16
2.1.1.4	Metastases	17
2.1.1.5	Further CNS tumors	17
2.2	Raman-Spectroscopy.....	18
2.2.1	Historical background.....	18
2.2.2	Physical background.....	19
2.2.3	Raman variants	21
2.2.3.1	Spontaneous Raman spectroscopy.....	21
2.2.3.2	Enhanced Raman spectroscopy	21
2.2.3.3	Non-linear Raman spectroscopy/coherent Raman-spectroscopy	21
2.2.4	Current applications.....	23
2.3	Fixation-methods in neuropathology	24
2.3.1	Formalin fixation	24
2.3.2	Cryofixation	25
2.3.3	Paraffin embedding.....	26
3	Questioning and objective of the study	27
4	Material and methods	28
4.1	Patient-data acquisition and handling.....	28
4.2	Solais	29
4.3	Samples.....	33
4.4	RS-data acquisition and handling	36
4.4.1	Machine learning.....	36
4.4.1.1	K-means-clustering and visualization techniques.....	36
4.4.1.2	RamanLabeler.....	38
4.4.1.3	T-distributed stochastic Neighbor Embedding.....	39
4.4.1.4	Support vector machine classifier	40
4.4.2	Pre-processing and filtering of the data	43
4.4.3	Different wavenumber regions	46
4.4.4	Statistical tests.....	48
4.4.5	Sample evaluation	50
5	Results.....	53
5.1	Fixation Study	53
5.1.1	Statistics	53
5.1.2	Fixation-study results.....	54
5.1.3	Paper submission.....	64
5.2	Meningioma-Study.....	65
5.2.1	Statistics	65
5.2.2	Meningioma-study results.....	67
5.2.3	Publication.....	75

6	<i>Outlooks</i>	76
7	<i>Discussion</i>	77
7.1	General discussion and limitations of the study	77
7.2	Fixation study	84
7.3	Meningioma study	87
8	<i>Conclusion</i>	91
9	<i>Conflict of interest</i>	93
10	<i>References</i>	93
11	<i>Acknowledgements</i>	106
12	<i>Supplements</i>	107
12.1	Supplement1: WHO-Classification of CNS tumors 2016 and 2021	107
12.2	Supplement2: Informed Consent	111
12.3	Supplement3: List of used abbreviations	114
12.4	Supplement4: Published meningioma paper	115
13	<i>Curriculum vitae</i>	125

Table of Contents for included figures and tables:

- Figure1** Physical principles of the Raman effect **p.20**
- Figure2** Polystyrene spectrum **p.20**
- Figure3** Chemical structure of formaldehyde **p.25**
- Figure4** Chemical structure of liquid nitrogen **p.26**
- Figure5** Chemical structure of dry-ice (carbon dioxide) **p.26**
- Figure6** Fully robotized Raman-spectroscopic system (Solais™, Synaptive®, Toronto, Canada) **p.29**
- Figure7** Raman spectrum of pure aluminium **p.30**
- Figure8** Schematic representation of the inside of the Solais™, the spectrum synthesis **p.31**
- Figure9** Photo of the screen of the Solais™ **p.32**
- Figure10** Workflow **p.33**
- Figure11** K-means-clustering over different samples **p.37**
- Figure12** Pseudo-colour image over different samples **p.38**
- Figure13** RamanLabeler **p.39**
- Figure14** A TSNE-Cluster of different samples **p.40**
- Figure15** SVM spectrum of meningioma samples versus dura mater samples **p.41**
- Figure16** Schematic and simplified representation of the different hyperplanes of a SVM classifier algorithm **p.42**
- Figure17** Schematic representation of data smoothing by the use of a Savitzky-Golay filter **p.44**
- Figure18** Summary of different spectral analyses with the nitrogen peak **p.45**
- Figure19** Raman spectrum of polystyrene divided into the different spectral regions **p.47**
- Figure20** Summary of statistical tests **p.48**
- Figure21** Comparative spectrum of collagen type I and IV **p.51**
- Figure22** Spectra of different lipids **p.52**
- Figure23** Raman spectrum of pure substances **p.52**
- Figure24** Mean spectra of native versus formalin-fixed data **p.55-57**
- Figure25** Mean spectra of native versus cryofixed data **p.58-61**
- Figure26** SVM-Classifer results of native, formalin-fixed and cryofixed meningioma and dura mater data **p.62**
- Figure27** Classifier results when natively trained classifier is applied onto formalin-fixed data with the use of a correction-factor **p.63**
- Figure28** Mean spectrum underlaid by the standard deviation of dura mater and meningioma with zoomed-in intervals **p.67**
- Figure29** TSNE over the entire spectrum as well as over the HWNR spectrum between dura mater and meningioma subtypes **p.68**
- Figure30** Same as figure29 but patient-based **p.69**
- Figure31** Mean spectra of dura mater and meningioma subtypes with annotated collagen peaks **p.69**
- Figure32** TSNE over the collagen peak spectrum between dura mater and meningioma **p.70**
- Figure33** Same as figure32 but patient-based **p.71**
- Figure34** Collagenase experiment **p.72**
- Figure35** TSNE cluster visualization with focus on the lipid peaks **p.73**
- Figure36** Histological verification of the trained classifier **p.74**
- Figure37** Different averages **p.79**
- Figure38** Different acquisition times **p.79**

Table1 Statistic of the fixation study **p.54**

Table2 Statistic of the meningioma study **p.66**

Table3 Results of different classifiers produced with the Matlab® Classification Learner app **p.81**

Table4 Main collagen peaks extracted from literature **p.88**

Abbreviation-list:

5-ALA	5-aminolevulinic acid
AKT1	Serine/threonine-protein kinases
BAP1	Breastcancer1-associated protein-1
CARS	Coherent anti-stokes Raman spectroscopy
CCD	Charged-coupled device detector
CDKN2A/B	Cyclin-dependent kinase inhibitor 2A/B
CHL	Centre Hospitalier du Luxembourg
CNER	Comité National d’Ethique de Recherche
CNS	Central nervous system
CT	Computer tomography
DNA	Deoxyribonucleic Acid
FFPE	Formalin-fixed paraffin embedded
FLAIR	Fluid-attenuated inversion recovery
FOR	Formalin-fixed
FRO	Frozen, cryopreserved
H&E	Haematoxylin and eosin
H3K27me3	Tri-methylation of lysine 27 on histone H3 protein
HWNR	High wavenumber region
IDH-Mutation	Isocitrate dehydrogenase-Mutation
KLF4	Krüppel-like factor 4
LNS	Laboratoire National de Santé Luxembourg
MAPK pathway	Mitagen-activated protein kinases pathway
MP	Measuring point
MRI	Magnetic resonance imaging
NAT	Native
NF2	Neurofibromatosis type 2
OCT	Optical Coherence Tomography
ODG	Oligodendroglioma
P	Patient
PIK3CA	Phosphatidylinositol-4,5-Bisphosphate 3-Kinase Catalytic Subunit Alpha
RS	Raman spectroscopy
SERS	Surface-enhanced Raman spectroscopy
SMARCE1	SWI/SNF-related matrix-associated actin-dependent regulator of chromatin subfamily E member 1
SMO	Smoothened, frizzled class receptor

SRS	Stimulated Raman spectroscopy
SVM	Support vector machine
TERS	Tip-enhanced Raman spectroscopy
TERT promoter	Catalytic subunit of telomerase
TRAF7	Tumor necrosis factor Receptor Associated Factor 7
TSNE	T-distributed Stochastic Neighbor Embedding
VLI	Visible-light image
WHO	World Health Organization

For tissue specific abbreviations see *suppelement3*.

1 Zusammenfassung

In diesem Manuskript wird eine neue Methode, basierend auf der Raman Spektroskopie, zur Diagnostik von Hirntumoren vorgestellt. Bei der Raman Spektroskopie werden die zu untersuchenden Gewebe mit einem Laser bestrahlt und das eingehende Licht wird dann zu einem kleinen Teil in einer veränderten Wellenlänge reflektiert. Dies wird als Ramaneffekt bezeichnet und ermöglicht einen genauen Rückschluss auf die biochemische Gewebeentität. Durch dieses spektroskopische Verfahren entsteht die Möglichkeit eine neue gewebserhaltende Untersuchungsmethode für den Neurochirurgen/Neuropathologen verifizieren zu können. Mithilfe von maschinellem Lernen soll ein SVM-Klassifizier (Support vector machine Klassifizier) trainiert werden, um möglichst schnell und unkompliziert verschiedene Gewebetypen unterscheiden zu können. Ein besonderes Merkmal wurde hierbei auf die Analyse und Differenzierung von fixiertem Gewebe gelegt. Es werden native Gewebeproben direkt nach der Entnahme aus dem Operationssitus verwendet und mit Hilfe eines speziellen Raman Spektroskops analysiert. Dabei wird immer ein visible light image (VLI) der Probe sowie der gesetzten Messpunkte festgehalten, was eine retrospektive Zuordnung jedes einzelnen Spektrums zu einem bestimmten Punkt erlaubt. Anschließend wird die Gewebeprobe von einem Neuropathologen interpretiert. Für die Fixierungsanalysen werden die Proben einmal im nativen Zustand gemessen und dann durch Trockeneis kryofixiert und/oder durch eine 4%-ige Formalin-Mischung haltbar gemacht. Auch diese Proben werden wiederum von einem Neuropathologen untersucht. Für die Fixierung wurde in dieser Arbeit zunächst festgehalten, dass die Kryofixierung mit Trockeneis die Raman-Spektren nicht wesentlich beeinflusst. Daraus folgt die Möglichkeit Klassifizier, die auf native Daten trainiert wurden, zur Analyse von kryofixierten Gewebeproben zu nutzen. Somit könnte die Raman Spektroskopie verwendet werden, um bereits bestehende Tumor-Banken zu explorieren ohne die wertvollen Proben zu zerstören. Auf der anderen Seite bringt die Formalin-Fixierung größere Änderungen auf biochemischer Ebene mit sich. Das macht die Handhabung Formalin-fixierter Proben schwieriger. Die Klassifizier-Ergebnisse konnten durch Differenzbildung zwischen dem reinen Formalin-Spektrum und dem Spektrum der Formalin-fixierten Daten verbessert werden.

Ein zweiter Punkt dieser Studie basiert auf der Differenzierung von Dura mater und Meningeomen. Dieser wird zuerst in der Unterscheidung der verschiedenen Raman-Spektren und anhand der klar differenzierbaren TSNE-Plots (T-distributed Stochastic Neighbor Embedding Plots) festgestellt. Nach einigen weiteren Analysen kann dann festgestellt werden, dass diese Abweichung zu einem gewissen Anteil durch den ungleichen Kollagengehalt sowie die variierende Lipid-Zusammensetzung dieser beiden

Gewebstypen zustande kommt. Zuletzt wird ein SVM-Klassifizierer mit den vorliegenden Daten trainiert. Mit diesen Ergebnissen kann eine virtuelle Einfärbung (heat map) des Probenbildes realisiert werden. Dabei wird ein Filter über das Bild gelegt, welcher Meningeom-enthaltende sowie Nicht-Meningeom-enthaltende Bereiche in unterschiedlichen Farben kennzeichnet. Dies könnte dem Neurochirurgen erlauben, Rückschlüsse auf den Gewebeerstamm mit einer Sensitivität von 93,0% und einer Spezifität von 89,7% zu ziehen. Die Resultate konnten auf histologischer Ebene verifiziert werden.

Zusammenfassend kann festgehalten werden, dass sich diese neue geweberhaltende und schnelle Methode für die intraoperative Gewebe-Diagnostik sowie die retrospektive Analyse von bereits fixierten Proben eignet. Die Raman-Spektroskopie könnte den klinischen Alltag als schnell durchführbares und einfaches diagnostisches Verfahren bereichern. Weitere und tiefgreifende Studien an weiteren Gewebeentitäten sollten mit der Raman Spektroskopie vorgenommen werden, um einen noch besseren Einblick in das mögliche Potential der Raman Spektroskopie zu erhalten. Die Ergebnisse der Fixierungs-Analyse, also die Möglichkeit einen auf native Daten trainierten Klassifizierer auf kryofixierten Daten anzuwenden, eröffnet die Möglichkeit zur Exploration von Tumor-Banken. Hierbei könnten auf schnelle Art und Weise sehr viele Daten, auch Daten bezüglich seltener Tumoren gesammelt werden, was wiederum die Präzision und Genauigkeit der trainierten Klassifizierer erhöhen könnte. Ausblickend könnte außerdem ein sogenannter Omniclass-Klassifizierer trainiert werden, ein Klassifizierer der zwischen allen möglichen Gewebearten unterscheiden könnte. An der Weiterentwicklung dieses Verfahrens wird gearbeitet, zusätzliche Tumorentitäten werden untersucht und Ziel ist es, das Verfahren in das Operationsmikroskop des Neurochirurgen zu integrieren. Dies könnte bereits intraoperativ ein direktes Feedback über das eventuell zu resezierende Gewebe geben.

Summary

This manuscript introduces a new method, based on Raman spectroscopy, for the diagnosis of brain tumors. In the field of Raman spectroscopy, the tissues are irradiated with a laser and the incoming light is afterwards reflected to a small extent in a modified wavelength. This is called the Raman effect and allows accurate conclusion of the biochemical tissue entity. This spectroscopic technique creates the possibility of verifying a new, potentially powerful, and tissue-preserving examination method for the neurosurgeons/neuropathologists. With the help of machine learning, a SVM classifier (Support vector machine classifier) is trained to distinguish different tissue types as quickly and easily as possible.

Special emphasis is put on the analysis and differentiation of fixed tissue. Native tissue samples are used directly after removal from the surgical site and analysed using a special Raman spectroscope. A visible light image (VLI) of the sample as well as of the bevor set measuring points is always recorded, which allows a retrospective assignment of each individual spectrum to a specific measuring point. Afterwards, the tissue sample is interpreted by a neuropathologist. For fixation analyses, samples are measured once in the native state and then cryofixed by dry ice and/or preserved by a 4% formalin mixture. These samples are again analysed by a neuropathologist.

For fixation, it is first noted that cryofixation with dry ice does not significantly affect the Raman spectra. From this follows the possibility of using classifiers trained on native data to analyse cryofixed tissue samples. Therefore, Raman spectroscopy could be used to explore pre-existing tumor-banks without destroying the valuable samples. Formalin fixation implicates major biochemical changes. This makes the handling of formalin-fixed samples more difficult. The classifier results could be improved by difference formation between the pure formalin spectrum and the spectrum of the formalin-fixed data.

A second point of this study is based on the differentiation of dura mater and meningioma. This is first established in the differentiation of the various Raman spectra and in the clearly differentiable TSNE plots (T-distributed Stochastic Neighbor Embedding plots). After some further analyses, it can then be concluded that this discrepancy is to some extent due to the unequal collagen content as well as the varying lipid composition of these two tissue types. Last, a support vector machine classifier is trained with the available data. With these results, a virtual colouring of the sample image can be realized. Thereby, a kind of filter (heat map) is superimposed on the image, which marks meningioma-containing as well as non-meningioma-containing areas in different colours. This could allow the neurosurgeon

to draw conclusions about the tissue origin with a sensitivity of 93.0% and a specificity of 89.7%. The results could be verified at a histological level.

In conclusion, this new tissue-preserving and fast method is suitable for intraoperative tissue diagnostics as well as retrospective analysis of already fixed samples. Raman spectroscopy could enrich the clinical routine as a fast performable and thus simple diagnostic method. Further and in-depth studies on additional tissue entities should be performed with Raman spectroscopy to gain even more insight into its promising potential. The results of the fixation analysis, i.e., the ability to apply a classifier trained on native data to cryofixed data, opens the possibility for the exploration of tumor-banks. A large amount of data, including data on rare tumors, could be collected in a fast way, which in turn could increase the precision and accuracy of the trained classifier. In the future, a so-called omniclass classifier could be trained, a classifier that could distinguish between all possible tissue types. Further development of this method is underway, additional tumor entities are being investigated, and the goal is to integrate this method into the neurosurgeon's operating microscope. This could provide direct intraoperative feedback about the tissue that may need to be removed.

2 Introduction

2.1 Braintumors

2.1.1 Classification

Tumors of the human central nervous system (CNS) are categorised by the WHO classification. Originally, the researchers wanted to establish an easy usable and reproducible classification system mostly based on the commonly used H&E staining distinction of the tumors. The first edition was published in 1979 by Zülch et al..¹ Over the years, and with the fast-improving research technologies (especially in the field of molecular biology and personalized medicine), the need for a more precise classification system raised. Within the last years the WHO classification is concentrating more and more on specific genetic and epigenetic markers (DNA, methylation grade etc.) to precisely identify the tumor. This has also led to a reorganisation of the well-known and established classification system. The most recent 2021th WHO classification of CNS tumors handles this topic. The fifth edition of the WHO Classification of Tumors of the central nervous system replaces the fourth edition released in 2016.² In the 2021th edition, tumors are classified more and more alongside the molecular and epigenetic markers like IDH-mutation, MAPK pathway etc.³

In the next chapters the main tumor entities will be described with a special focus on their diagnostics, therapy and outcome. Because of the large amount of different CNS tumor entities, only the ones used in the further analyses of this project will be described in detail in the following sections. Since the here used tumor samples are mostly scanned before 2021, we will rely in our experimental setup mainly on the 2016th WHO-classification. *Supplement1* summarizes the subdivision of the WHO-classification of 2016 and 2021.

2.1.1.1 Meningiomas

Meningiomas are some of the most common intracranial and intraspinal tumors. They are more frequent in female patients.² Claus et al. described in 2013 a positive correlation between the incidence of meningioma and a high body-mass-index, smoking and exogenous hormones respectively.⁴ Meningiomas origin from the arachnoid cap cells and do mostly not tend to infiltrative growth. In the 2016 published WHO classification, meningiomas are classified in three grades. Grade I corresponds to the histological appearance of lymphoplasmacyte-rich, meningothelial, transitional, psammomatous, fibrous, angiomatous, microcystic and secretory meningioma. Metaplastic, chordoid, clear cell as well as atypical meningioma form grade II. The last grade includes papillary, rhabdoid and anaplastic meningiomas. The WHO grading is based on the probability of recurrence as well as the aggressivity of the tumor. As a conclusion, the WHO classification relies on the expected survival rate: a higher grade corresponds to a lower survival rate. Furthermore, numerous studies show a positive correlation between the proliferation index Ki67 and the risk for recurrences.^{5,6}

In the 2021th edition meningiomas are seen as a single type with 15 subtypes. Molecular biomarkers are used for a more detailed classification. For example BAP1, breastcancer1-associated protein-1 tumor suppressor gene, is used for grading the rhabdoid and papillary subtypes.³ The other molecular biomarkers are: KLF4, AKT1, TRAF7, SMARCE1, SMO, PIK3CA, H3K27me3, TERT promoter, NF2, and CDKN2A/B.³

Since meningiomas are slowly growing tumors the first symptoms, which appear often only lately, are frequently caused by their compressing nature. Depending on the location, symptoms may vary. They range from unspecific headaches, cranial nerve deficits, vision loss over to seizures.⁷

After the appearance of clinical symptoms, meningiomas are mostly diagnosed by computer tomography (CT) and/or magnet resonance imaging (MRI). CT shows a homogeneous, slightly hyperdense mass, not infiltrating the brain, which has a strong uptake of intravenous contrast. A homogeneous contrast uptake can also be observed in the diagnostic by MRI. Here meningiomas appear iso- to hypointense in the T1 sequence and hyperintense in the T2 sequence.⁷ Since meningiomas are originating from the dura mater, a 'tail sign' can often be observed.⁸ In special cases, an angiography can be used preoperatively to localize and visualize the vascular blood supply of the tumor, which can be important for minimization of blood loss during surgery. The therapy consists of a surgical resection of the tumor. The completer and more radical the surgery is, the lower is

the risk for tumor recurrence. To classify the grade of resection, the completeness, the Simpson grading has been introduced in 1957.⁸

The Simpson grading is split into five stages. Stage one corresponds to a complete excision and stage five is no excision at all, only a small tumor fragment, a biopsy has been taken for neuropathological analysis.

If the symptoms are of minor importance, not restricting the daily life of the patient or if the patient is of fragile health, a watchful waiting strategy can be applied. Furthermore, a therapy by stereotactic irradiation could be used.

Since the recurrence rate is directly proportional to the remaining tumor cells after surgical resection, an intraoperative method for resection control, like Raman spectroscopy, would be of great importance for direct tumor-border identification. This would allow a more precise tumor resection, meaning that the surgeon could remove more tumor tissue without the risk of removing too much healthy tissue.

2.1.1.2 Gliomas

In the group of gliomas, astrocytomas and oligodendrogliomas are combined. They represent tumors with a glial origin.

In the WHO classification from 2016 four different grades can be differentiated. A slowly growing pilocytic astrocytoma, mostly prominent in children, with the possibility of a curative resection is determined as WHO grade I. Grade II and III include the diffuse, as well as the anaplastic astrocytoma and at last, grade IV with the most dangerous one, the glioblastoma. Gliomas are mostly infiltrating tumors.

The group of oligodendrogliomas is divided into WHO grade II and III. The latter one is also known as anaplastic oligodendroglioma.

At a WHO grade higher than I, a curative resection is not possible. Therapy consists of resection as radically as possible, and radiochemotherapy. In the next paragraphs we will have a closer look at glioblastomas.

Glioblastomas are known to be among of the most frequent (15% of all intracranial neoplasms) and deadliest brain tumors.² Glioblastomas are fast growing and highly invasive. They are composed of a variety of different cellular components (central necrosis, hypercellularity, endothelial proliferation etc.), and different genetic backgrounds. The most common molecular/epigenetic markers are for example the isocitratdehydrogenase (IDH)-status and the methylguanine-DNA-methyltransferase (MGMT)-promotor-status. The MGMT-promotor-status is important, for example, because in its inactive form, the tumor tissue will be accessible for a chemotherapy by Temozolomide.⁹

In the latest WHO classification (2021) gliomas are newly divided into six different families: circumscribed astrocytic gliomas, adult-type diffuse gliomas (here included are the glioblastomas), paediatric-type diffuse low-grade gliomas, paediatric-type diffuse high-grade gliomas, glioneuronal and neuronal tumors and ependymomas.³

The symptoms vary depending on the location, ranging from seizures over headaches and paralysis. Symptoms may appear rapidly and worsen as the tumor grows quickly. Some symptoms are also provoked by the oedema surrounding the tumor, which compresses the healthy cells. This phenomenon is reflected in the rapid improvement of symptoms when these patients receive corticosteroids, which diminish the oedema and thus reduce the symptoms.¹⁰ Glioblastomas appear in the CT and MRI hypodense and infiltrative with a necrotic centre. Intravenous contrast forms characteristic rings around the tumor. On MRI analyses, glioblastomas appear hypodense in T1 and hyperdense in T2. FLAIR-MRI is particularly good at identifying glioblastomas. Surgical removal is the main component of therapy, involving radiation and chemotherapy (mostly Temozolomide). The malignant

glioblastoma therapy is summarized in the widely used Stupp protocol.^{11,12} In surgery, the tumor can be visualized by fluorescence, by the preoperative oral application of 5-aminolevulinic acid.^{13,14} A most recent conservative treatment method is the use of electromagnetic fields, established by an 'electrode-helmet' that the patient must wear around the clock. This therapy has been shown to be very successful, even in Phase III studies.^{15,16} Nevertheless, glioblastomas have a bad outcome with a median survival rate of approximately 15-18 month after diagnosis.² Therapy can prolong the survival time by some months up to some years, cure is nearly impossible.

Again, radical tumor removal is the most important for good patient outcome. The prognosis correlates strongly with the extend of resection. This is particularly difficult because of the widely infiltrating growth of the malignant cells. Complete neurosurgical tumor removal is currently nearly impossible because it would involve extensive tissue removal that could result in neurological deficits for the patient. Therefore, we need a new, non-destructive technology to identify these scattered malignant cells.

2.1.1.3 Lymphomas

Lymphomas are divided into primary lymphoma, which are lymphomas that fist appear in the CNS, and secondary lymphoma, which are lymphomas that are first diagnosed in a different region than the CNS with secondary infiltration of it. Since it is difficult to correctly identify a lymphoma by its clinical appearance or by CT/MRI (FLAIR) imaging, a biopsy is currently unavoidable. Therapy consists of aggressive treatment with chemotherapy and glucocorticosteroids, which induces a significant downsizing of the tumor.^{17,18} Second-line therapy consists of radiotherapy. RS would potentially allow a direct intraoperative confirmation of the sample's entity, reducing the need for an expensive and time-consuming biopsy. Furthermore, RS would allow to identify the biochemical composition of the tumor.

2.1.1.4 Metastases

Tumor diseases are often associated with the appearance of metastases. The increasing appearance of metastases is potentially due to the better and more effective oncological therapies of the primary tumors which allow a longer patient survival. A formation of malignant cells originating from the primary tumor is formed in another part of the body, often in the brain or bones.^{19,20} The most common cancers that metastasizes into the brain are bronchial carcinoma, breast cancer, melanoma and renal cell carcinoma.²¹ Metastases are no random formation of cell deposits, but dependent on certain influencing factors. The primary tumor must have a strong vascularization (angiogenesis), which allows the malignant cells to enter the blood stream and migrate to another part of the body. During the migration process, the metastatic cells must bond onto other cells/proteins. And finally, they need to invade and replicate in the new location.¹⁹

In an ensuing CT, a hypodense lesion (hyperdense if haemorrhages are present) with a perifocal oedema can be observed. Intravenous contrast can accumulate and multiple brain lesions can often be observed.²² Furthermore, an MRI/FLAIR can be used as a diagnostic tool. Once a metastasis is suspected, a biopsy for confirmation as well as a full body examination must follow to find the primary carcinoma. In addition to treatment of the primary tumor, the metastasis is surgically removed or irradiated (radiosurgery) when possible. Recent studies have identified specific molecular pathways in metastases, which could revolutionize the therapy toward individualized adapted medicine.^{23,24,25} RS would allow rapid identification of the tumor origin of the analysed metastasis, which is essential for a rapid tumor detection and immediate initiation of the appropriate therapy. Furthermore, an intraoperative resection control of the metastasis could be achieved by RS. Since RS could give a good insight in the biological background of the metastases it could be a helping tool for the identification of the before mentioned multiple molecular pathways.

2.1.1.5 Further CNS tumors

A list of other CNS tumor types, not yet described in the previous sections can be found in *supplement1*. *Supplement1* gives an overview of the tumor differentiation according to the WHO classification of 2016 and 2021. These tumor types are not within the focus of this thesis mostly because they are rare tumors and would not be of great relevance in this particular study.

2.2 Raman-Spectroscopy

2.2.1 Historical background

Raman spectroscopy was discovered in 1928 by the Indian professor Raman and his students, especially K.S. Krishnan and K.R. Ramanathan. Its theoretical predication was already made in 1923 by the scientist A. Smekal. Professor Raman had a special interest in the deeper understanding of the scattering of light. In April 1923 one of his students, K. R. Ramanathan, noticed that if sunlight passes through a violet glass containing a liquid, the emerging rays are not the same as the ones from the incident beam. In 1925, another one of his students, K. S. Krishnan observed the same phenomenon when analysing light scattering through different purified liquids. At this point, Raman claimed that there must be a new form of light scattering and took further experiments in exploring it. He putted a beam of sunlight onto a blue-violet filter which was succeeded by a container including different liquids. A scattering of light has been demonstrated for nearly 80 different liquids. He published his results in "Nature" on the 19th of February 1928 under the name "A new Type of Secondary Radiation". After further studies, he published again on the 28th of February 1928 a historical paper, by describing the fundamentals of RS. For his discovery, Prof. Raman won the Nobel prize in physics in 1930.

The discovery of the Raman-effect opened the door for multiple further studies in chemistry and physics. Or as described by Prof. Raman in his paper 'A new radiation' published in 1928 in the Indian J. Physics "*We are obviously only at the fringe of a fascinating new region of experimental research which promises to throw light on diverse problems relating to radiation and wave-theory, X-ray optics, atomic and molecular spectra, fluorescence and scattering, thermodynamics and chemistry.*"^{26,27}

2.2.2 Physical background

When a laser source emits an incident light beam onto a sample, more precisely a molecule, a part of the light is scattered. When the incident photon hits an electron, the electron gains energy and assumes a virtual energy state for a very short time. Then the electron falls down and emits the photon again. When this scattered light has the same energy as the energy gained by the incident laser beam, from its photon, it is called Rayleigh scattering. Since the amount of energy is the same, this is a phenomenon of elastic light scattering. A small fraction of electrons, approximately every $10^{7\text{th}}$ will be of a different energy level, higher (stokes) or lower (anti-stokes). This phenomenon is called Raman scattering, inelastic light scattering. These energy changes are expressed by the physical value of wavelength/Raman shift (cm^{-1}). The different wavelengths that apply to different molecular bonds can be viewed as the molecular footprint of the sample. In this way, specific molecules can be qualitatively identified by emitting a non-destructive laser beam onto a sample and measuring the scattered Raman waves.^{28,29,30} Each obtained Raman peak, a specific wavelength, corresponds to an individual chemical bond, such as C-C or a group of bonds, like benzene. In addition, we can make quantitative observations using the Raman effect. The value of a Raman line determines the concentration of a molecule in the analysed sample.

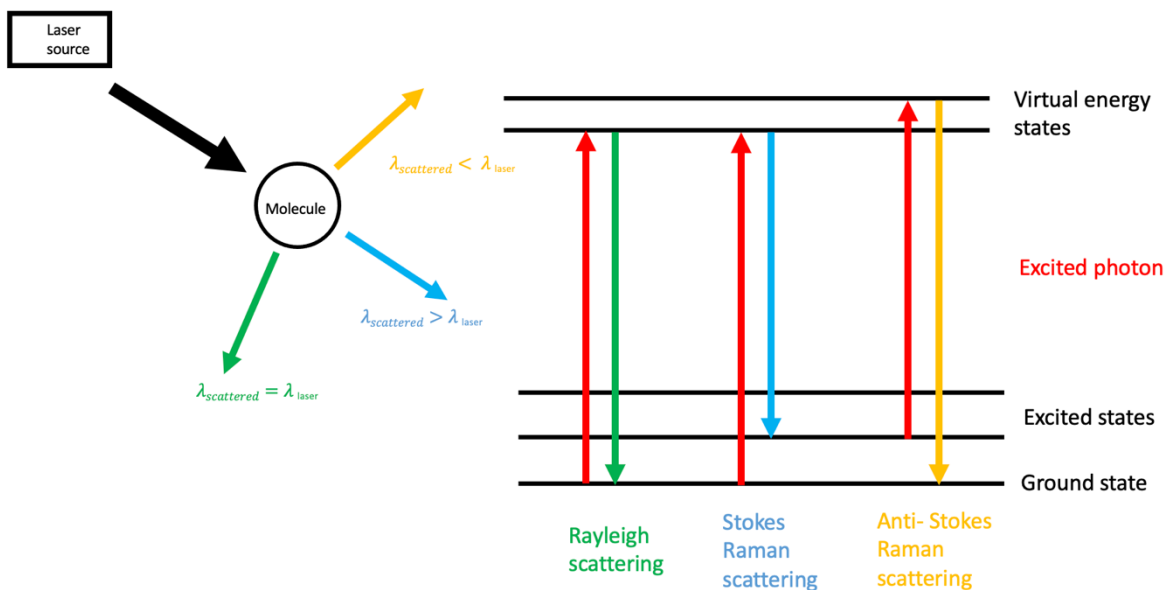


Figure1: Physical principles of the Raman effect. The red arrow represents the photon excited by the incident light of the laser source. The green arrow represents the Rayleigh scattering, the wavelength from the scattered light is the same as for the incident light. The blue arrow represents the Stokes Raman scattering where the scattered light is of higher frequency than of the incident light, gain of energy. The yellow arrow represents the anti-Stokes Raman scattering, where the scattered light is of lower frequency than of the incident light, loss of energy. Figure source: own production. Figure produced with PowerPoint®.

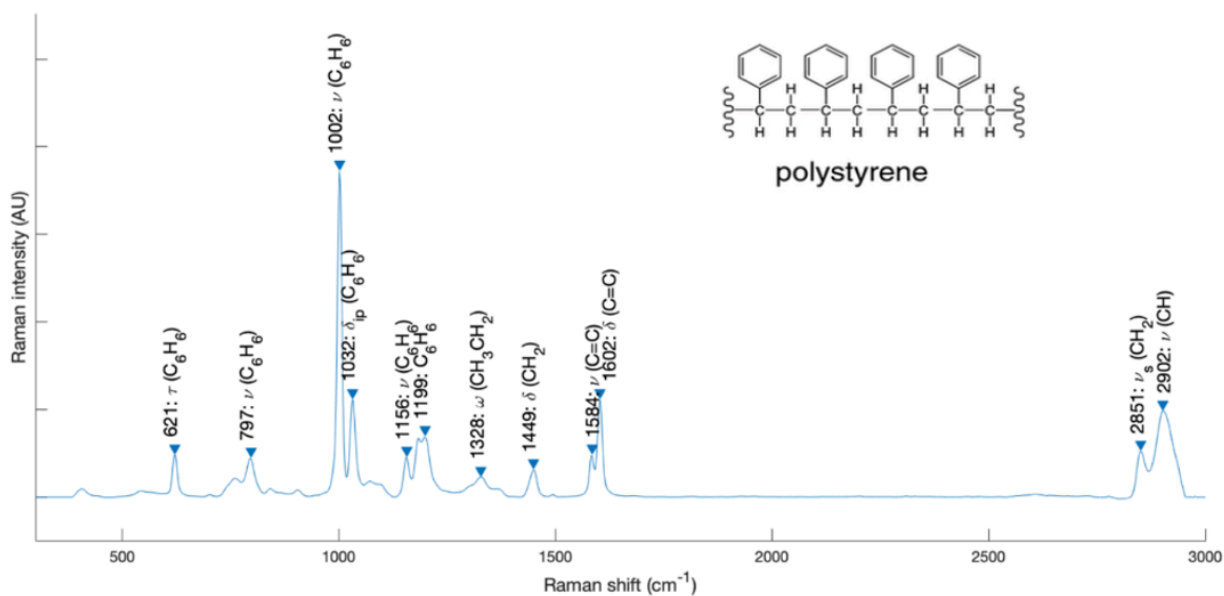


Figure2: Polystyrene spectrum. Each peak is annotated by its corresponding chemical bond. Upper right: Chemical structure of polystyrene. Figure source: own production. Figure produced with Solais™ and Matlab®.

2.2.3 Raman variants

Over 25 different techniques of RS variants are known.³¹ Here only some of the most important ones are highlighted.

2.2.3.1 *Spontaneous Raman spectroscopy*

The transition from the excited state (virtual state of energy) to the end state can happen at any time, so spontaneously. Since only a small part of the incident light is scattered here, it leads to a weak Raman effect.³¹ The physical principle is the same as mentioned above (2.2.2.). The term of normal Raman spectroscopy is often used synonymously for Spontaneous Raman spectroscopy.

2.2.3.2 *Enhanced Raman spectroscopy*

In the domain of the enhanced Raman spectroscopy, we differ between surface-enhanced Raman spectroscopy (SERS) and tip-enhanced Raman spectroscopy (TERS).

To increase the normally weak Raman signal nanoparticles of, for example, gold or silver can be added to the sample. When these nanoparticles are excited by the laser beam, a surrounding electric field is built up. And since Raman intensities are proportional to the strength of an electric field, the Raman signal of their direct environment is improved. This effect is made useful in the surface-enhanced Raman spectroscopy (SERS). SERS is a really potent Raman form, able to detect even single molecules which makes it a perfect fit for, for example, early cancer detection in serum samples.³²

The tip-enhanced Raman spectroscopy (TERS) is based on the same idea as the SERS but instead of nanoparticles, silver- and/or gold-coated peaks are used.^{33,31}

2.2.3.3 *Non-linear Raman spectroscopy/coherent Raman-spectroscopy*

Non-linear Raman spectroscopy includes, amongst others, the stimulated Raman spectroscopy (SRS) and the Coherent anti-stokes Raman spectroscopy (CARS).

In the case of the SRS, two different laser sources are used to obtain a stronger Raman signal. When two photons of two different frequencies (f_1 and f_2) interact simultaneously with the same molecule, this molecule will vibrate with a frequency of $f_3 = f_1 - f_2$. A higher sensibility is accomplished with this method but a much more complex instrumentation is needed. It is often used in material composition analyses and microscopic analyses.³⁴

For the realization of a coherent anti-stokes Raman spectroscopy (CARS), three different lasers are needed: a pulsed pump beam (f_1), a pulsed stokes beam at a lower, variable

frequency (f_2) and a probe beam at a higher, fixed frequency (f_3). Light at the anti-stoke frequency is produced at the interaction of these three beams ($f_3+f_1-f_2$).^{33,31} It is widely used in Raman microscopy since it is sensible for nuclear vibrations of chemical bonds.

2.2.4 Current applications

RS is used in a wide variety of fields, from medicine to physics, chemistry and even civil engineering. In the medical field, Raman spectroscopy is already established for cancer detection, especially in dermatology, skin cancer diagnostics and gynaecology, cervical cancer diagnostics.^{35,36} The already established cancer diagnostic by RS is mostly limited to easily accessible tissue samples. Direct measurements in situ are still in a clinical, an experimental phase. Huang et al. describe the utilization of a Raman spectroscope integrated into an endoscope to characterize body, corpus and antrum in the upper gastrointestinal tract.³⁷ In forensic medicine, RS is commonly used to identify various body fluids, gunshot residues, and culprit identification.³⁸ In the pharmaceutical field, each process step must to be controlled (concentrations, growth of cell cultures, biochemical factors in a specific cell culture etc.). The absence of contamination of the probes under investigation is critical, which urges the need for a direct measuring method, devoid of taking a probe and analysing it in a different containment. André et al. describe a RS process for direct prediction of antibody titer in a vaccine production by immersing a Raman spectroscope directly in the solution.³⁹

One more special example of the extra-clinical Raman utilization is the study of Cho et al. in which they demonstrate the possibility to identify toxic chemical substances in building walls using Raman spectroscopy.⁴⁰ Because toxic substances can be truly harmful to the health of building occupants, it is critical to identify them as quickly as possible. Raman spectroscopy with its non-destructive properties, is the ideal method for rapid identification without the need to destroy the walls.

In this study we use spontaneous Raman spectroscopy to analyse biological tissue and to investigate the influence of different fixation methods on the RS signals.

2.3 Fixation-methods in neuropathology

For successful specimen analysis in pathology, it is essential to preserve the sample for an extended period of time without altering its histological appearance. There are already well established and widely used methods ranging from chemical (formalin-fixation) to physical (cryopreservation) fixation to more complex fixation methods such as paraffin-embedding, all classical methods in pathology. Part of the here presented study focuses on the possibility to use Raman spectroscopy to identify fixed samples, such as samples from tumor banks, for inclusion in RS analyses. RS is important not only for intraoperative diagnostics but also for postoperative analyses (influence of radiation/chemo-therapy on the tumors), so it is imperative to further investigate the influence of stored samples on RS.

2.3.1 Formalin fixation

The nowadays used 4% formaldehyde solution was created by Blum (1892) after the discovery of formaldehyde by Butlerov in 1859.⁴¹

Formaldehyde is a trigonal planar structure composed of 2 hydrogen, one carbon and one oxygen atom (CH_2O) which is naturally in a gaseous form, but turns into a liquid solution by condensation and the formation of polymers (*figure3*). It is a highly reactive substance which interacts easily with other components. Formalin forms with primary amines Schiff bases, with amides hydroxymethyl groups, which in turn react with a second amide to methyl diamides. With alcoholic hydroxyl it forms acetals and with sulfhydro groups sulphydral acetal.

In pathology the property of cross-linking with different functional groups makes formaldehyde a tempting solution for sample fixation.^{42,43,41} The widely used formaldehyde solutions are mostly mixed with methanol for a first alcohol fixation (dehydration causing a hardening of the membranes and tissues) and only afterwards a formalin-fixation by cross-linking. Formaldehyde hydrates and forms methylene glycol, which implements molecules to react between each other by forming polymers. This methylene-glycol will dehydrate into carbonyl formaldehyde. The actual tissue fixation is accomplished by the hydrated and the non-hydrated form of formaldehyde. Furthermore, it is important to notice that the initial penetration of the formalin into the molecule, takes around 24h to 48h but the stable, irreversible, crosslinking comes only after about 30 days. Since different studies already tried RS on formalin-fixed samples it is possible to find literature describing the new appearance of RS peaks for formalin-fixation at multiple locations. Here some examples: 907cm^{-1} , 1041cm^{-1} , 1254cm^{-1} , 1490cm^{-1} , 1492cm^{-1} .^{44,45}



Figure3: Chemical structure of formaldehyde. Figure source: own production. Figure produced with PowerPoint®.

2.3.2 Cryofixation

The technic of cryofixation is based on a quick down-cooling of samples to very low temperatures in order to avoid any tissue destruction often caused by a slow, step-by-step heat dissipation. Two main methods of cryofixation can be distinguished. First, liquid nitrogen (-170 degrees Celsius) offers the possibility to continuously cooling a sample at very low temperatures (*figure4*). Since the “normal” air contains 78,08% of nitrogen, it is possible to isolate liquid nitrogen from liquid air (cooled down air) by different air separation techniques. It is a colourless, odourless and non-flammable gas. Since liquid nitrogen is extremely cold, it can provoke burns if not handled with care. Nevertheless, liquid nitrogen is commonly used for sample storage, such as in tumor banks, spermatocyte and egg conservation.⁴⁶ Also in medicine, liquid nitrogen is used on a daily basis for cryotherapy of warts and skin lesions.⁴⁷ Liquid nitrogen is known for its ability to rapidly cooling down a sample, avoiding mostly the formation of ice crystals.

Second, dry ice (-80 degrees), the solid form of carbon dioxide (CO₂) is often used for cryofixation, for example in embryology (spermatocytes and oocytes), tumor-sample storage and even in the alimentary industry (*figure5*).^{48,49,50} The chemical formula of dry-ice is composed of two oxygen atoms bound by double bonds to one carbon atom. Like liquid nitrogen, it is a colourless and non-flammable gas. The sublimation of gaseous CO₂ into the solid CO₂, without passing by its liquid phase, is accomplished at a temperature of -78,5 degrees and an atmospheric pressure of 5,13 atm. A limitation of the cryofixation is the unavoidable induced tissue destruction by the formation of ice crystals/freezing artefacts and the need for a constant temperature maintenance at very low levels since any thawing could irreversibly harm the sample.^{51,52} According to literature the freezing of samples

induces OH-stretching bonds at the spectral region over 3000cm^{-1} as well as some peaks at lower frequencies (205cm^{-1} , 215cm^{-1} , 601cm^{-1}).^{53,54,55}



Figure4: Chemical structure of liquid nitrogen

Figure source: own production.

Figure produced with PowerPoint®.

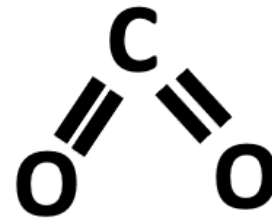


Figure5: Chemical structure of dry-ice (carbon dioxide).

Figure source: own production.

Figure produced with PowerPoint®.

2.3.3 Paraffin embedding

For a correct neuropathological examination, the samples have to be embedded in paraffin which allows to cut the prepared sample afterwards in thin slices, essential for sample storage and precise sample analysis under the microscope. Paraffin wax is derived from petroleum and consists of a soft, colourless texture. At room temperature it is solid and liquifies with heating. Since it is insoluble in water and relatively resistant towards a multitude of chemical substances, it is often used in the standard pathological workflow.^{56,57}

The sample preparation, consisting of formalin-fixation, dehydration, paraffin-embedding, microtomy, eventually staining and dewaxing as well as the interpretation of a neuropathologist, is a time-consuming, complex work.

Some studies have had a closer look onto the Raman spectroscopic changes induced by paraffin embedding, mostly when working with pathologically fixed samples, to see if paraffin-embedding would influence the results. It has been demonstrated that paraffin-embedding induces significant spectral changes at 1063cm^{-1} , 1133cm^{-1} , 1296cm^{-1} , 1441cm^{-1} , 1032cm^{-1} , 1203cm^{-1} , 1490cm^{-1} in RS.^{45,44}

3 Questioning and objective of the study

RS is a new, quick, easy-usable and non-destructive diagnostic tool which could change the handling of samples, in this case, neurosurgical samples. If successful, RS could reduce the need for complex and costly diagnostic procedures such as biopsies and specific neuropathological analyses. In addition, it could significantly improve patient outcome during surgical tumor resection by allowing a more precise and instantaneous detection of malignant cells. It could complement commonly used resection monitoring tools such as intraoperative quick-sections, ultrasound and MRI. This would significantly reduce the risk of tumor recurrence as well as the risk of removing healthy brain tissue during radical tumor removal. Therefore, we are interested in exploring the potential of RS. Is it possible to correctly identify a tumor entity? Can malignant and healthy cells be accurately distinguished by RS? Can we train a classifier based on these data? What are the strengths and what are the limitations of RS? Is it a usable tool for ubiquitous clinical use? In addition, we will take a closer look at the ability of RS to identify fixed, cryofixed and formalin-fixed samples. Is it possible to correctly identify the effect of formalin-fixation and cryofixation on the RS spectrum? What causes these spectral changes? And will it be possible to use these fixed samples for further RS analyses? This would open up the possibility of using already fixed samples for RS analyses, increasing the number of samples in a short amount of time and as a conclusion rapidly improve machine learning. This information could help to develop an omni-class classifier in the future. RS could be used to analyse existing tumor-banks and provide us important information on the biochemical impact of different fixation methods. This could complement the work of the neuropathologist and perhaps even expand the information gain. To analyse all these here enumerated questions and objectives, we are newly introducing machine learning into the RS data analysis procedure, which could facilitate and generalize the handling of the often complex RS data. This could enable the introduction of RS into the clinical routine.

4 Material and methods

We tried to answer the before mentioned study objectives by including formalin-fixed and cryofixed specimens to analyse the influence of fixation on RS. Furthermore, dura mater and meningioma samples were used to explore the potential of RS to differentiate between diverse tissue types and to correctly identify the infiltration zone. On the machine learning side, TSNE and SVM classifiers are used. In the following sections, a detailed overview of the used methods is given.

4.1 Patient-data acquisition and handling

The study is performed at the neurosurgical department of the Centre Hospitalier du Luxembourg (CHL). Only people assigned to the study-group and working in the CHL have directly handled patient data. Neuropathological sample analysis is done at the Laboratoire National de Santé Luxembourg (LNS). All samples are collected during routine neurosurgical interventions (mostly patients with brain tumors) and no supplement samples are extracted for the study. Patients all signed informed consent before participating and they are, at any point of the study, exposed to any additional risks. A copy of the informed consent form is attached at the end of this manuscript (*supplement2*). The Comité National d'Ethique de Recherche (CNER) approved the study on the 13.07.2018 under the number 201804/08. The study is handled according to the WMA Declaration of Helsinki-Ethical principles for medical research involving human subjects as well as to the law 'EU General Data Protection Regulation GDPR' of 01.08.2018.^{58,59} During the follow-up of the data analysis, all patient data are pseudonymized by a numeric code, no retracement from a diagnose/sample to the original patient can be done by a person outside of the study group. The results of the study are not, at any moment, influencing the treatment or the outcome of the patient.

4.2 Solais

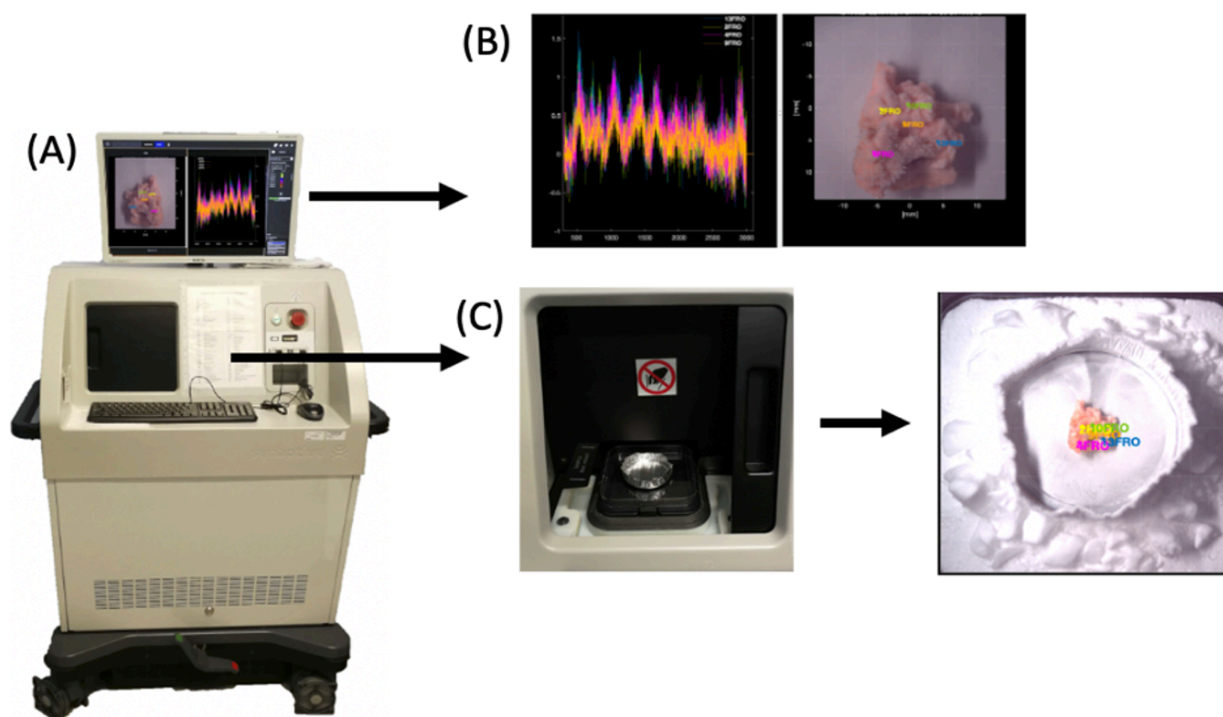


Figure6: (A) Fully robotized Raman-spectroscopic system (Solais™, Synaptive®, Toronto, Canada) equipped by a movable stage and a VLI-camera. (B) Zoom-in on a machine-screen showing a Raman spectrum and a VLI of a cryopreserved sample. (C) Zoom-in on the movable stage containing an aluminium-cup with a tissue sample as well as a VLI of the cryopreserved sample. Figure source: own production.

A fully robotized RS-machine (Solais™, Synaptive®, Toronto, Canada) is used, see *figure6*. The machine is equipped with a movable stage, a visible-light imaging camera (VLI-camera), a 785nm laser source as well as an optical coherence tomography (OCT). Every RS measurement is linked to a visible light image which allows a retrospective retracement of the exact position of the engraved measuring points. This allows us to review every single point, every single Raman spectrum to the original macroscopic sample area. Each spectrum is composed of 1602 single values, spread on a wavenumber scale from 314cm^{-1} to 2994cm^{-1} . The final spectrum, the spectral curve, is formed by an internal computerized system.

First, all samples were scanned on plastic cups, but since plastic has a very high Raman spectrum on its own, it interfered so strongly with the sample spectrum that the actual sample spectrum could no longer be interpreted. Since aluminium has a negligent Raman spectrum we decided to use this as the basis for the scans.^{60,61} An aluminium spectrum is

represented in *figure7*. The scans are done with 6-30 acquisitions and with an accumulation time between 800ms to 2000ms for each measuring point.

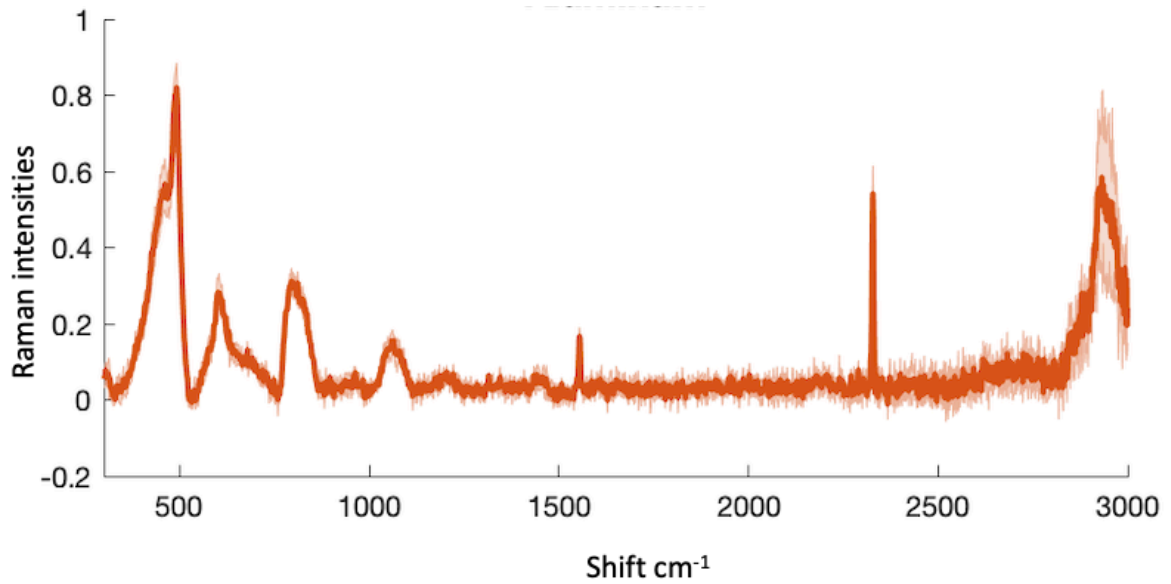


Figure7: Raman spectrum of pure aluminium. Y-axis represents the Raman intensities and the X-axis represents the Raman shift (cm⁻¹). Figure source: own production. Figure produced with Solais™

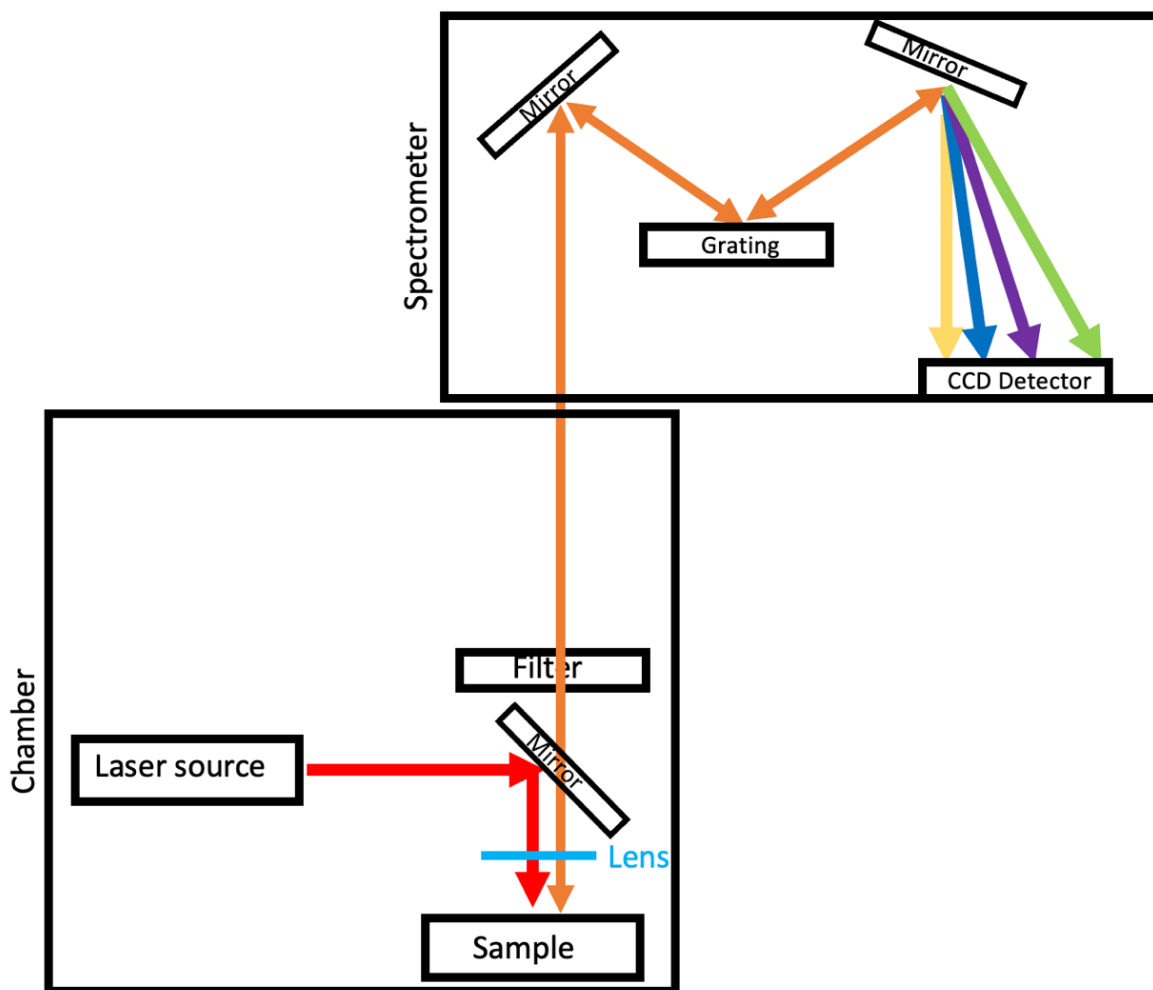


Figure8: Schematic representation of the inside of the Solais™, the spectrum synthesis. Figure source: own production. Figure produced with PowerPoint®.

A laser source enters the chamber where it is deflected by a splitter/mirror in order to reach the sample (*figure8*). The incident light is scattered in different wave lengths from the sample. The light first transverses a lens where it is focused, then it passes a filter, often band-stop or low-pass filter. Here the Rayleigh signal is divided from the Raman scattered light in order to obtain a stronger Raman signal. After passing through the filter, the scattered light arrives at the spectrometer. With the help of a mirror the light is shined onto a grating where it is decomposed into its different wavelengths. These are again transmitted on a CCD (charged-coupled device) detector which forms the final spectrum.^{62,63,64}

Furthermore, the Solais™ is able to perform an optical coherent tomography (OCT), see *figure9*. This could give further information on the sample composition, its thickness by the different reflection of light waves. It is standardly used in ophthalmology to examine the different layers of the retina.^{65,66} Since this study focuses on RS, the OCT data will not be further displayed in this thesis.

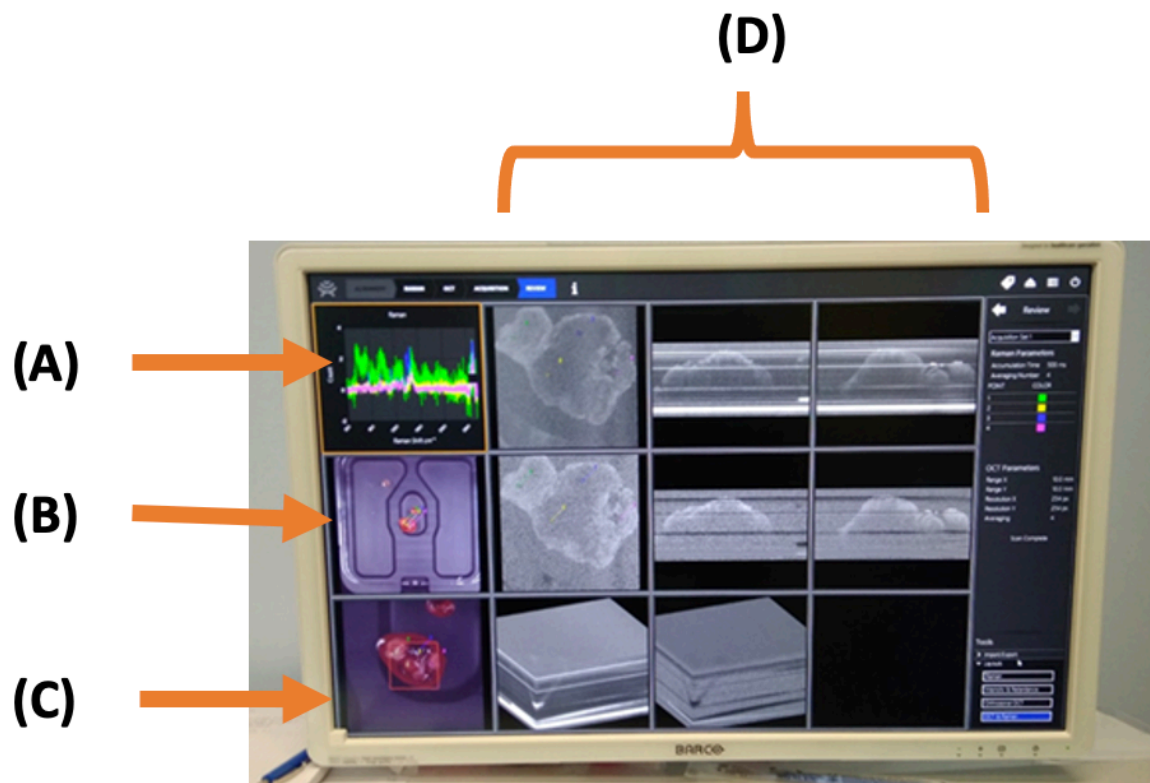


Figure9: Photo of the screen of the Solais™. **(A)** Raman spectrum; **(B)** VLI of the scanned sample on a plastic dish with the engraved measuring points; **(C)** zoomed-in VLI, same as in (B); **(D)** OCT-scans. Figure source: own production.

4.3 Samples

All used tissue materials are samples from human participants, collected during routine neurosurgical interventions from 2018 to 2021. No additional samples or probes are extracted during the surgery for the purpose of this study. We only use tissue of the removed tumors and/or tissue that has to be detached during the surgery either way in order to access to the point of interest, for example the tumor. Since it is an experimental setup and since we want to have 'real-life' conditions, the samples are scanned as they are without additional treatment. This leads to a more heterogenous sample surface, form and appearance. In order to guaranty a correct retrospective retrace of the pathological description and the measuring points, big samples are divided into smaller pieces of +/- 2mm to 5mm. Every sample is analysed individually by a specialist in neuropathology.

After a brief overview of the used RS-machine and the sample acquisition, we will take a closer look at each step of the scanning process, the workflow (*figure10*).

The native samples are only treated with some physiological water (NaCl). Physiological water is also used during the surgery, so that we can say that our samples are scanned natively.

For the fixation-study, some samples are fixed for different time laps (going from some minutes to multiple weeks) in a 4% formaldehyde solution and scanned afterwards again. For the cryopreservation we use dry ice instead of liquid nitrogen, for practical reasons since liquid nitrogen would evaporate during the scanning procedure without ensuring a constant freezing of the tissue. Dry-ice is placed under the aluminium cup to allow complete and constant sample freezing without having direct contact with the sample.

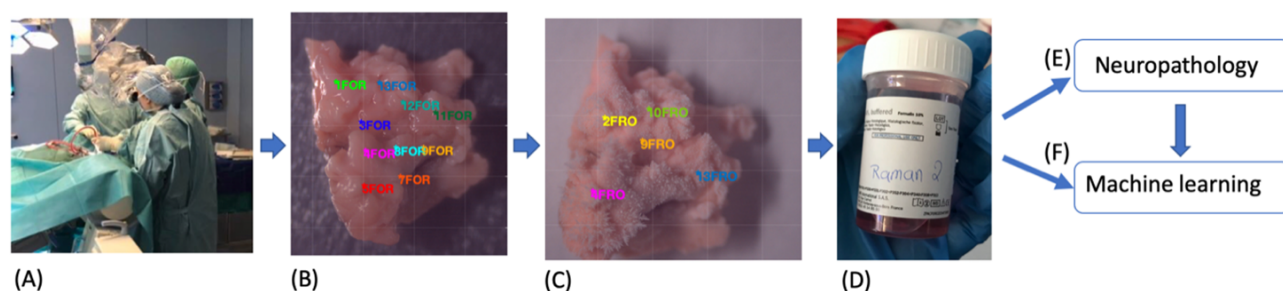


Figure10: Workflow (A) Intraoperative native sample acquisition (B) Native or formalin-fixed Raman scan (VLI) (C) Cryopreserved scanned sample (VLI) (D) Sample storage in a formalin solution (E) Neuropathology analysis (F) Machine learning. Figure source: own production.

All patients gave their informed consent to participate in the study. Directly after surgical removal the samples are taken to the RS-machine, situated directly besides the operation room. Here they are placed on an aluminium cup and humidified with some drops of

physiological water in order to avoid any tissue dehydration and, as a consequence to avoid any tissue destruction during the scanning procedure. The aluminium cup containing the sample is placed onto the movable stage. The door is closed. The user interface of the Solais™ allows to indicate some essential information which will be linked to the sample afterwards: subject ID (pseudonymized Patient ID), subject name (abbreviations to describe the underlying sample, see *supplement3*), date of birth (only the year of birth of the patient is indicated), gender (male, feminine, other) and the sample excision date and time. Afterwards, the sample is focused and the measuring points, up to 25 measuring points per measurement, can be distributed all over the sample. The last step before proceeding to the actual scanning process, is the indication of the acquisitions (how often one measuring point is scanned: 6-30x) and of the accumulation time (how long the scanning for every measuring point is: 800ms to 2000ms). Different parameters can have different influences on the afterwards obtained spectrum. For more information see *discussion*. Increasing the parameters will resolve in a clearer spectrum but since the duration of the scanning process itself will also significantly increase, this could lead to sample dehydration. Once the scanning procedure finished, the tissue sample is extracted from the RS-machine and put into a 4% formaldehyde solution. The samples are all precisely annotated and sent to the neuropathology (LNS). Here the tissues are, in a blinded manner, fixed and analysed by a specialist in neuropathology. Once the pathological report present (one separate report for each sample with a precise description for every single measuring point), we add the precise sample description to the corresponding measuring point.

If a sample fixation is wished, the native samples are, before being sent to neuropathology, fixed either by formalin or by dry-ice.

One sample containing meningioma and dura mater was specially prepared in neuropathology in order to do a histological verification of the results of the trained dualclass classifier (see section 5.2.). The native sample is first marked with three incisions which will allow at any time a perfect reorientation of the sample. Then it is put onto an aluminium cup and scanned with the Solais™ with approximately 110 measuring points, all done with the parameters of 2 seconds and 30 averages. The sample's surface is covered with a maximum of measuring points so that a precise sample overview can be achieved. Afterwards, the sample is put into the waxing cassette, containing a formalin solution. Once in pathology, the sample is embedded in paraffin and sectioned into 21 slices. This is to ensure that for each measurement, the corresponding area on the surface is histopathologically assessed, and no tissue underneath the surface that may have been different from the one analysed by spectroscopy, is investigated. A H&E (haematoxylin and eosin) staining is performed on each slide. The 21 slides are stack one upon the other with

respect to the three marker incisions. This allows to have an H&E image comparable to the VLI. A frame is traced around the margins of the VLI which is also fitting to the histological image. This frame is used as reference for the marking of the measuring points on the histological sample. Finally, each measuring point is checked for correct classification (i.e., the classifier's predicted identity was compared to the histopathological finding at the very same spot).

4.4 RS-data acquisition and handling

4.4.1 Machine learning

Machine learning (ML) is becoming increasingly important and consists of training an algorithm that can perform the task in a next step without any further programming. We need to distinguish two main types of machine learning. On the one hand, supervised learning, where the algorithm is trained to distinguish categories based on specific recognition features. On the other hand, unsupervised machine learning consists of repeated trainings in which the algorithm learns to find the best possible way to differentiate the desired categories.⁶⁷ Unsupervised machine learning does not require any prior labelling of the training data.⁶⁸

4.4.1.1 K-means-clustering and visualization techniques

K-means-clustering is an unsupervised machine learning algorithm, which can be used to visualize different clusters within a dataset. In K-means clustering, K is the number of wished clusters. The system tries to see which data (in this specific case the mean of data) are closest to the defined clusters. Once found, it will attribute all data to one of these specific clusters which results in a clear data split. Calculating the variance within these clusters, the assignment of the data points to the distinct clusters will be re-evaluated and might lead to the reassignment of data points to better fitting clusters. By repeating this until there is no reassignment necessary the data is sorted into clusters.^{69,70} The similarities between the spectra are visualized in *figure11* by a colour code, a correlation matrix, red represents high similarity and blue less similarity. This provides information on potential biochemical clustering between different spectra. In a designed pseudo-colour image, repeating random colour sequences can be observed (*figure12*). In our example yellow indicates a high spectral intensity and blue a low spectral intensity. Furthermore, we used a heat map to overlay the before mentioned special sample containing meningioma and dura mater to have a visual representation of the analysed tissue entity. A heat map is a visual representation of data quantity (see *figure36*).⁷¹

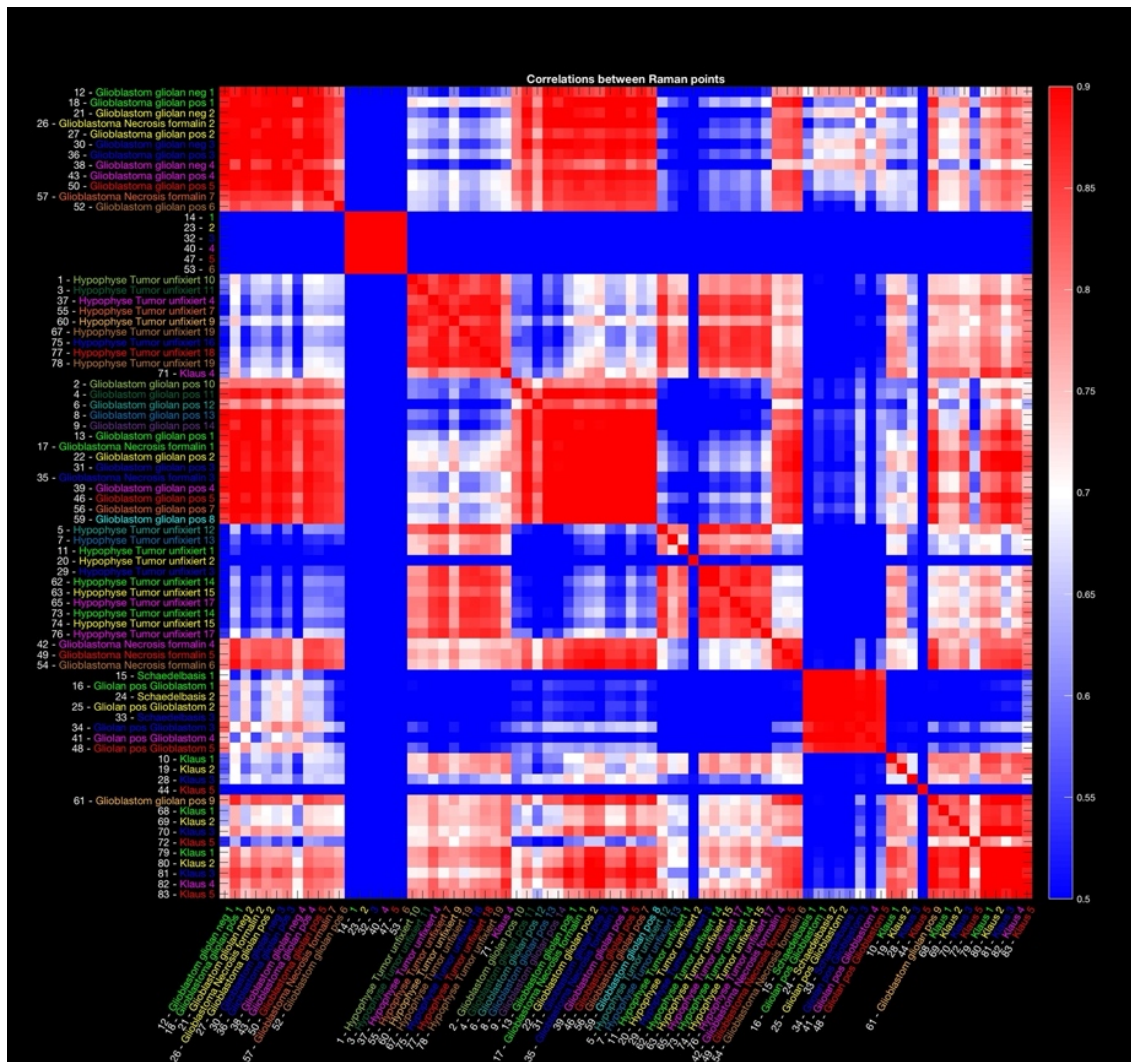


Figure11: Correlation matrix of a K-means-clustering over different samples (for example glioblastoma, hypophyses tumor, pieces from the base of the skull). In red, high correlation between the compared substances, in blue, low correlation. X-axis corresponds to an enumeration of the different samples. Y-axis is the same enumeration as on the X-axis in order to compare the samples one by one. Figure source: own production. Figure produced with Matlab®.

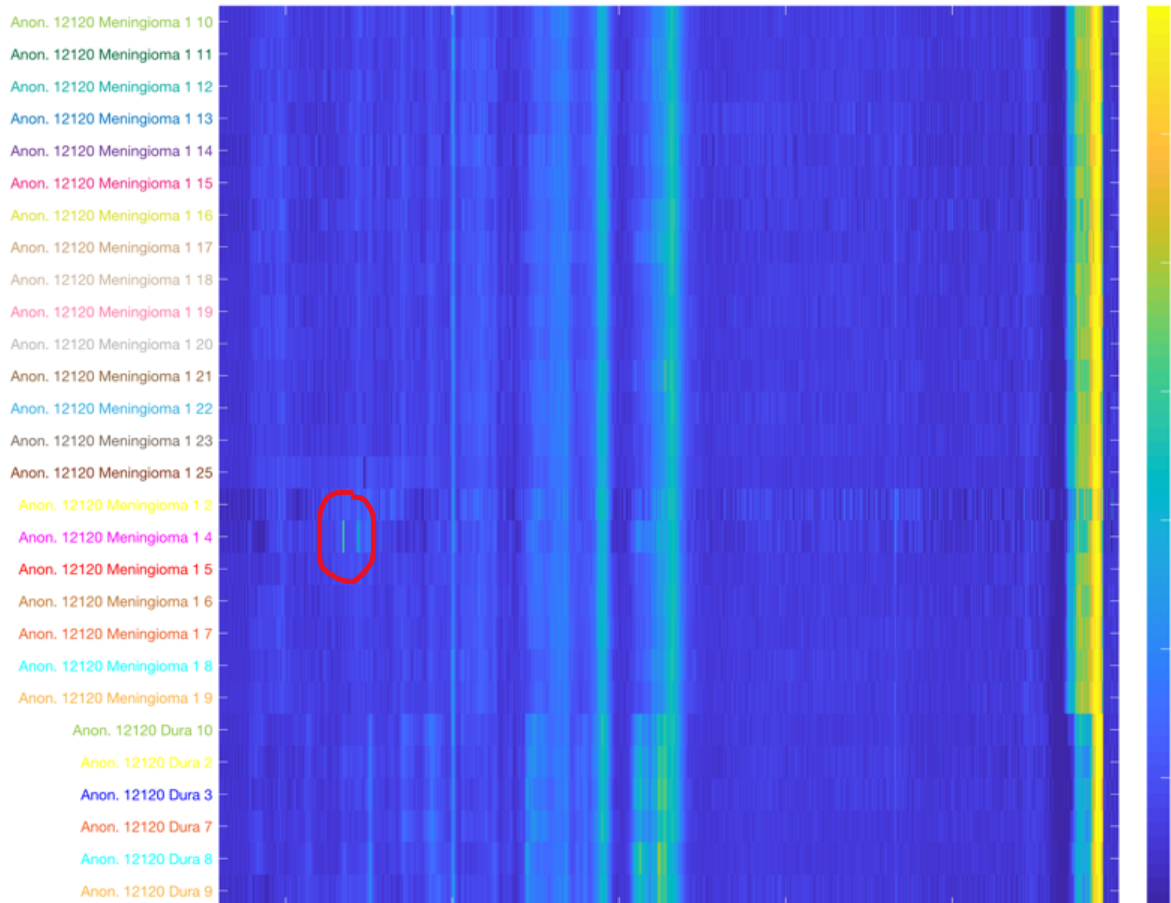


Figure12: Pseudo-colour image of different samples (meningioma, dura mater). In yellow, high spectral intensity. In blue, low spectral intensity. Red circle, one single yellow bare in the middle of blue bares, possible outlier, cosmic ray artifact. X-axis corresponds to the different wavenumbers and the Y-axis represents the here analysed samples. Figure source: own production. Figure produced with Matlab®.

4.4.1.2 RamanLabeler

In *figure13*, a screenshot of the inhouse-designed RamanLabeler is represented. It is a user interface for data visualization usable with Matlab®. By selecting one patient after the other (left side under Patient ID), it is possible to display on one side the visible light image with the engraved measuring points (right side) and on the other side the corresponding Raman spectra (left side). This allows to have an easy look on the macroscopic image, as well as simultaneously the Raman spectrum. This is essential for correct outlier sorting, cosmic ray removal and the fundamental understanding of the spectra. A concrete example would be the following: when an unexpected spectrum is observed, the VLI can show that the measuring point is directly on a blood vessel, bone fragment or other substance/location, which can explain the outstanding spectrum. In general, the RamanLabeler is used for visual analysis (comparison) of the included native and fixed samples, their macroscopic as well as their spectral appearance.

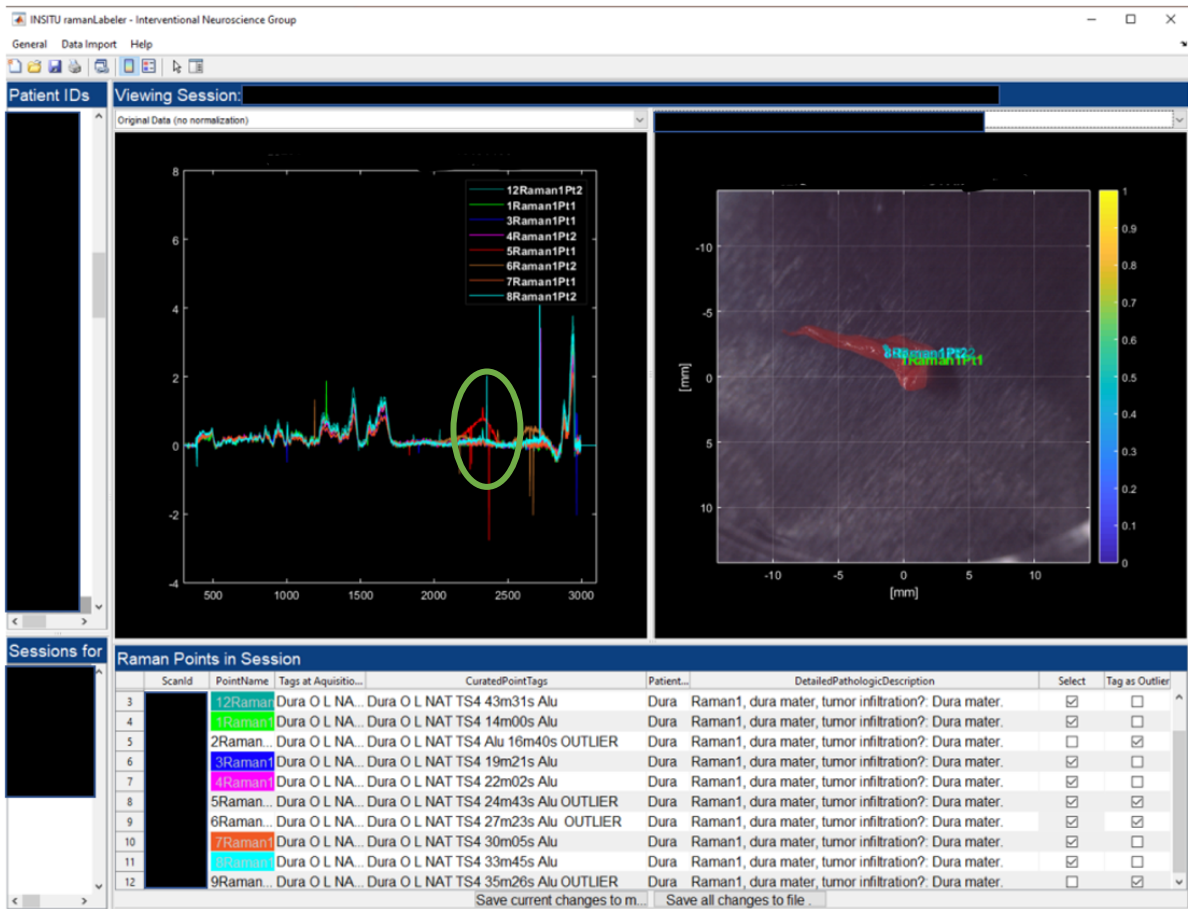


Figure13: RamanLabeler, a user interface for data visualization. Picture on the right side, visible light image of a scanned tumor piece. Picture on the left side, corresponding Raman spectra. The green circle indicates a cosmic ray artifact. The black-boxes are covering the confidential patient data. Figure source: own production.

4.4.1.3 *T-distributed stochastic Neighbor Embedding*

The t-distributed stochastic Neighbor Embedding (TSNE), *figure14*, is a visualization cluster with the objective to nonlinearly reduce a more-dimensional space (high dimensional data) into a two- or three-dimensional space.^{72,73} Similar data will be modelled and clustered by proximate points, non-similar data will be clustered by broad points. The t-distribution, also called Student's t-distribution, is a statistical test used for analyses on a small amount of data with a population of unknown variance. It is an approximation of the normal distribution.⁷⁴

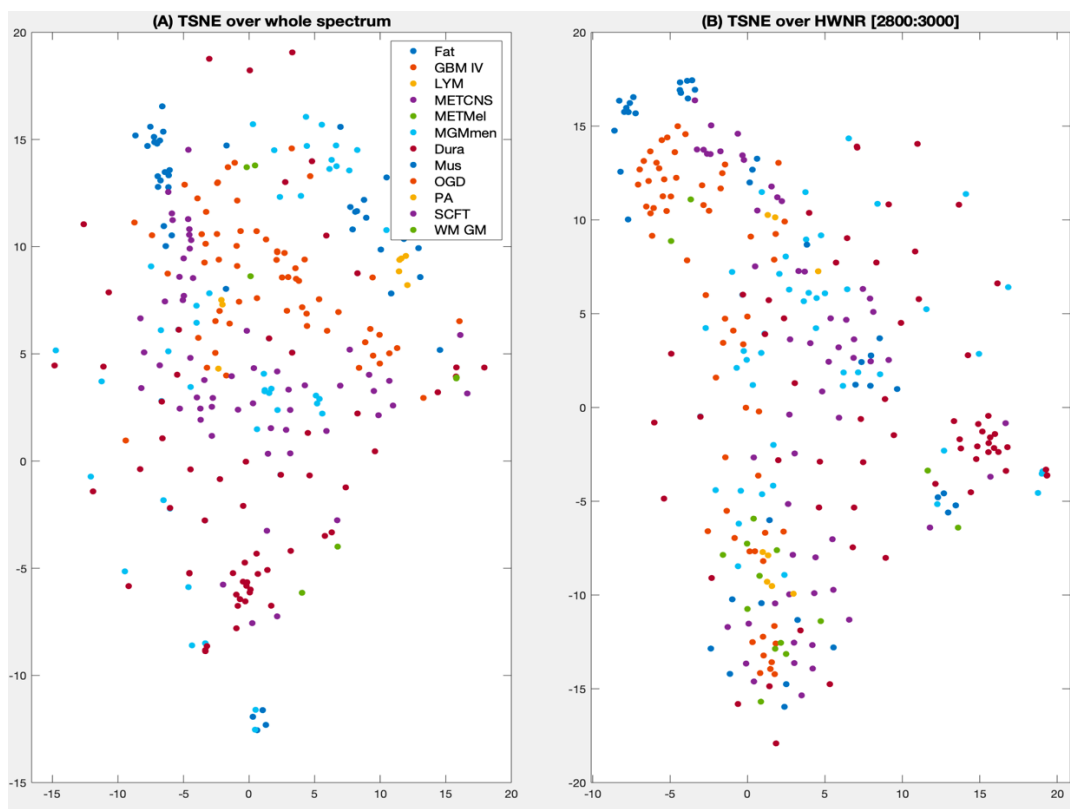


Figure14: A TSNE-Cluster of different samples: fat (Fat), glioblastoma (GBM), lymphoma (LYM), metastasis of the CNS (METCNS), metastasis of a melanoma (METMel), meningotheelial meningioma (MGMmen), Dura mater (Dura), muscle (Mus), oligodendrogloma (OGD), pilocytic astrocytoma (PA), subcutaneous fat tissue (SCFT), white and grey matter (WM GM) **(A)**, TSNE-Cluster of the entire Raman spectrum of the chosen entities **(B)** TSNE cluster over the high-wavenumber region (HWNR), interval 2800cm^{-1} to 3000cm^{-1} . No clear cluster formation can be observed here. Figure source: own production. Figure produced with Matlab®.

4.4.1.4 Support vector machine classifier

A support vector machine (SVM) classifier is an algorithm that is able to learn, by analysing a huge amount of different data to classify newly introduced data to the correct category in the future.^{76,77} It is a linear two-class classifier and since it needs a training set it is also a supervised learning algorithm, *figure15*. SVM tries to draw a hyperplane between the different categories, multiple choices are possible. The hyperplane with the maximal distance towards the different categories will be chosen (margins), see *figure16*. Here a precise, simplified example: We feed the SVM with 100 spectra of pathologically diagnosed meningiomas. It is trained to recognize that these specific spectral characteristics are assigned to a meningioma sample. If we give now a spectrum of unknown origin to the classifier it will be able to see if it is a meningioma or not. This can be repeated for multiple sample entities, which makes the SVM classifier more and more performant.

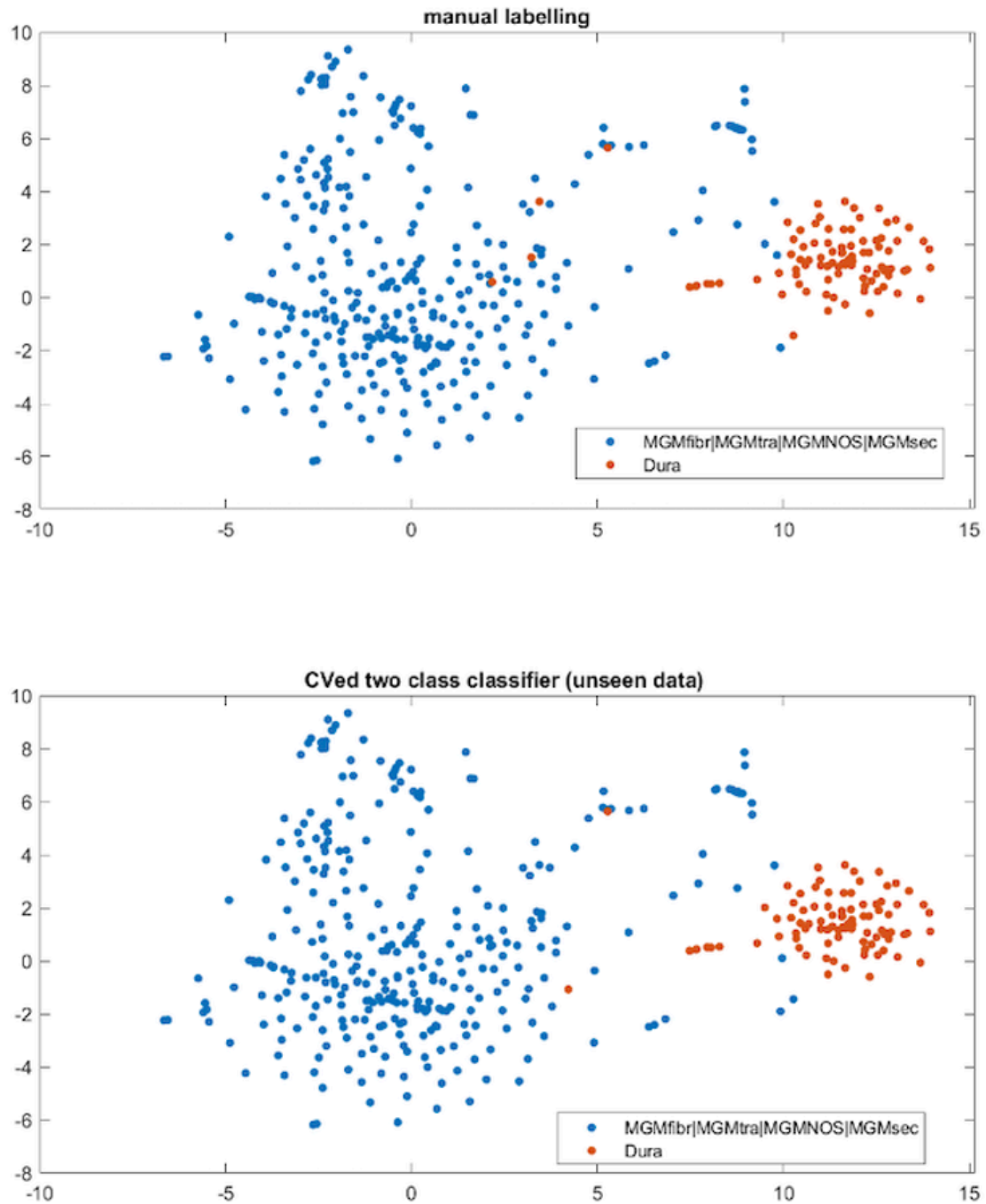


Figure15: SVM over the entire spectrum of meningioma subtypes and dura mater. The classifier is able to differentiate between the two classes. Top: manual labelling of different meningioma samples versus dura mater samples. Bottom: applied SVM on unseen, not yet used for ML, data. A differentiation between dura mater and meningioma subtypes is observable in the displayed clusters. Figure source: own production. Figure produced with Matlab®.

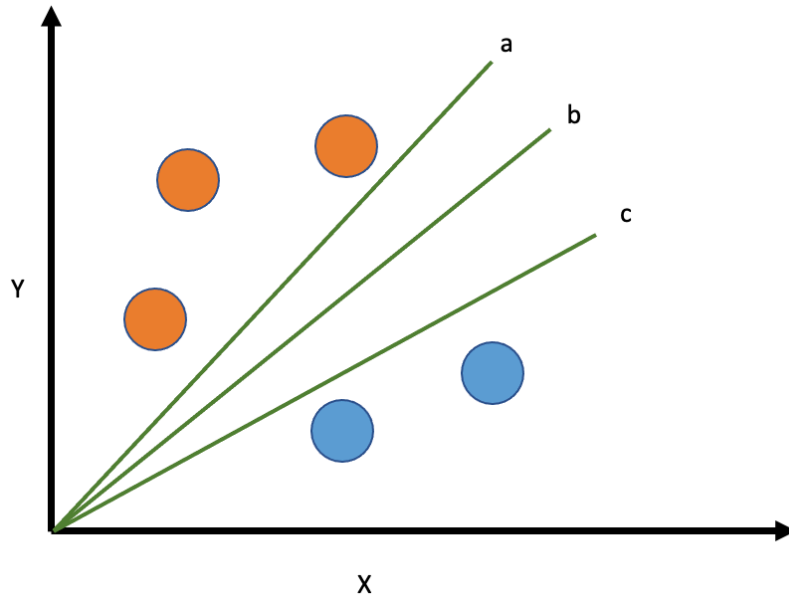


Figure16: Schematic and simplified representation of the different hyperplanes. In this case 'b' would be the hyperplane of choice since it forms maximal margins towards the two categories (towards the orange dots on the one side and towards the blue dots on the other side). Figure source: own production. Figure produced with PowerPoint®.

Based on the SVM training set, the affiliation probability is calculated. We visualized it by a blue to yellow colour code, which forms the basis of a colour mapping. This colour map, *figure36* in the result section, can be handled as an overlay to put on a visible light image. This forms the basis for one of the main objectives of this study, the possibility to implement a Raman spectroscope into the microscope of the neurosurgeon, allowing him to have a prompt and correct visual entity representation of the underlying tissue sample.

4.4.2 Pre-processing and filtering of the data

The data is pre-processed by the Raman spectroscope itself, using a background removal and a Savitzky-Golay filter, which are similar to the pre-processing of other commercial spectrometers.^{39,78,79} Furthermore, an outlier sorting, spectra normalization and cosmic ray removal are performed as described in the following chapter.

Cosmic ray artifacts are present in all photo-electric systems, especially if there is, like in the case of Raman spectroscopy, a CCD (charged-coupled device) included.⁸⁰ The spectral waves are split into different pixels on the CCD. Some arrive at non-orthogonal angles, provoking a mislead of the signal. For each measuring point, two measurements are done. One with the laser on and one just before, with turned-off laser (dark frame acquisition). If a cosmic ray artifact is happening during the 'laser-on' phase, the derived signal will be of positive intensity. Since we have in this phase multiple raw-individuals (these are the individual data corresponding to each wavenumber), a cosmic ray correction can be achieved by deleting this unique deriving raw individual and continuing the data processing with the remaining raw individuals. In the second case, in the dark frame acquisition, only one measurement is taken. If a cosmic ray artifact happens in this precise moment, the derived signal is of negative intensity. It is not possible to simply remove the misleading point, a replacement with a value of a corresponding scanning serie has to be done. These cosmic ray artifacts can also be called outliers. Furthermore, this precise cosmic-ray removal is integrated into the basic script for pre-processing of the data. See *figure13* for outlier demonstration.

A second type of outliers must be differentiated. By the 'real' outliers, we understand the spectral spikes where something other than the desired sample is scanned. This can happen once due to the translucent spectra of aluminium or because the sample moves during the scanning procedure. This can result in the originally defined measuring point no longer being on the sample. The correction of this type of outliers is achieved by the simple use of the standard deviations. If a value deviates significantly from the others, it is identified and deleted.

In a next step we have to focus on the 'background removal'. The background is composed of fluorescence as well as foreign (non-laser) light beam influencing the Raman spectrum. We are scanning inside of a 'black box' or 'dark chamber', because once the door of the Solais™ closed a dark chamber is formed. We will have nearly no interferences of the non-laser beams. The autofluorescence is composed of inevitable, mostly conjugated double

bounds of substances which are in every sample, like NADH (nicotinamide adenine dinucleotide bonded to an hydrogen atom) and heme (precursor of haemoglobin).^{81,82} Since the fluorescence spectrum is more prominent and strong than the Raman spectrum it is important to differentiate between the two spectra, to deal with the fluorescence.^{83,84,85} Here we use a Savitzky-Golay filter, a filter for spectral data smoothing. By the help of a polynomial, fitted on the raw data, a numerical derivative is calculated giving an approximative spectrum, easier to handle in further analyses. This polynomial is recalculated for every point of the raw spectrum resulting in an overall data smoothing. *Figure17* shows the data smoothing by the use of a Savitzky-Golay filter.⁸⁶ The 'intensity' of fluorescence is changing over time but since we are subtracting the fluorescence this should not interfere with our results.

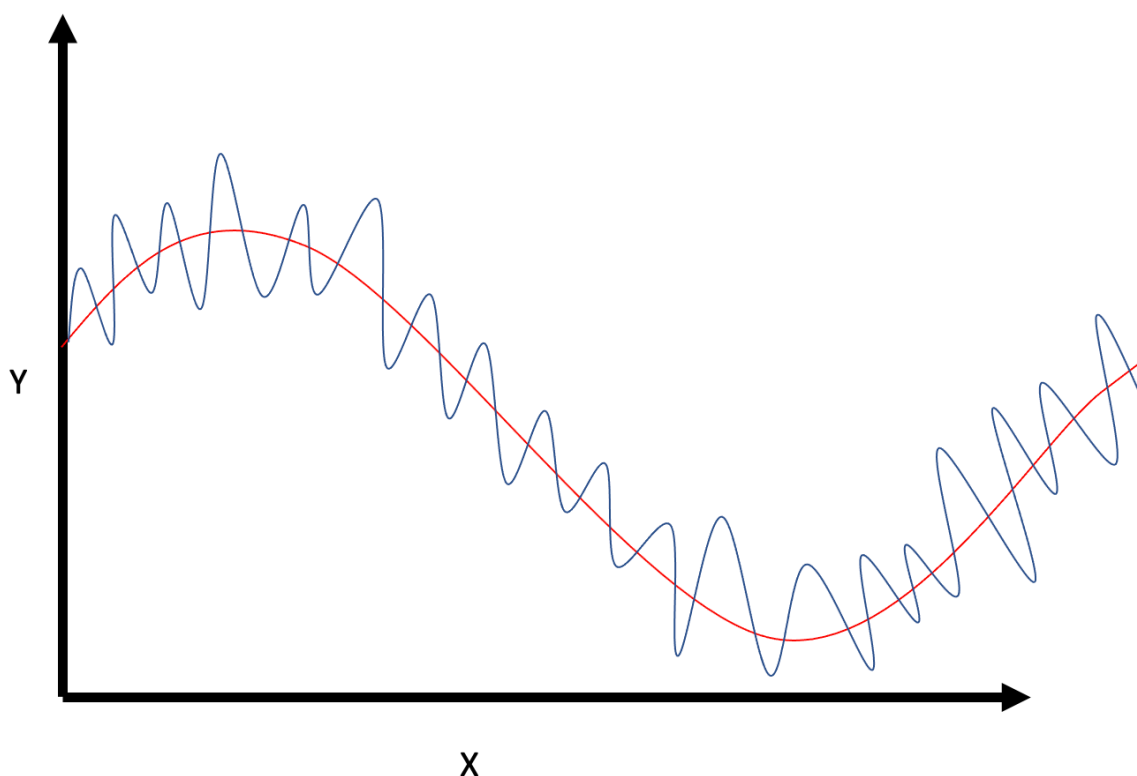


Figure17: Schematic representation of data smoothing by the use of a Savitzky-Golay filter. The RS spectrum is displayed in blue, the smoothen spectrum accomplished by a Savitzky-Golay filter in red. Figure source: own production. Figure produced with PowerPoint®.

The signal-to-noise ratio describes a relation between the desired signal and the signal of the background noise.⁸⁷ The background noise is a 'swoosh', no real signal but an oscillation of the spectra if its own intensity is weak. It is important to minimize the signal-to-noise ratio, for example by working with more averages (see *discussion*).

The spectra are normalized on the y-axis to allow better comparison. If a spectrum is of low intensities, it will be raised and vice-versa, if a spectrum is of high intensities, it will be lowered. This is an important step to be able to correctly compare and analyse different spectra. We can distinguish two different methods to accomplish the normalization. We can take one specific peak which is constant in every sample, like the nitrogen peak at 2330cm^{-1} .⁸⁸ See *figure 18*. Nitrogen is an important component of air and since ‘the amount of air’ or ‘the amount of nitrogen in the air’ will not change, we can take this peak as constant. If, for example, in one spectrum the nitrogen peak is extremely high after normalization we know that we have increased peaks composed mostly of noise, so no real signal. These spectra can be handled again as outliers. The second possibility for normalization is to define that, for one class of analysed spectra, the area under the spectrum (area under the curve) should be of same dimension. This allows to suggest that all presented peaks are in the same range of intensities and can be compared one against the other.

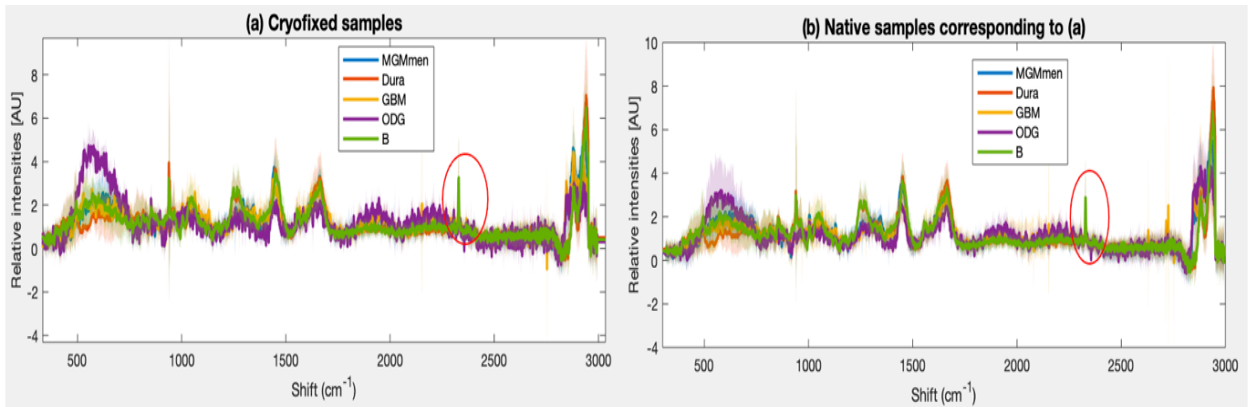


Figure 18: Summary of different spectral analyses: **(a)** shows different (meningothelial meningioma, dura mater, glioblastoma, oligodendrogloma and bone) cryofixed samples **(b)** shows different (meningothelial meningioma, dura mater, glioblastoma, oligodendrogloma and bone) native samples. The red circle shows every time the prominent peak of nitrogen at 2330cm^{-1} . The X-axis represents the Raman shift (cm^{-1}) and the Y-axis the relative intensities. Figure source: own production. Figure produced with Solais™.

4.4.3 Different wavenumber regions

A Raman spectrum has to be divided in different regions, depending on the wavenumber, (low wavenumber region, fingerprint region, silent region and high wavenumber region) for correct interpretation as well as right handling of the data (*figure 19*). In general, one can say that low Raman shifts are formed by weak bonds and large atoms and that high Raman shifts are formed by strong bonds and small atoms.^{89,90}

The low wavenumber region, between 10cm^{-1} and 400cm^{-1} , is often omitted because of its susceptibility to have great interference with background noise and low informative content when working with human tissues.⁸⁹ It represents mostly very heavy atoms, like in crystallin arrangements. It is more used in the pharmaceutical field.⁸⁹

The fingerprint region, ranging from 400cm^{-1} to 2000cm^{-1} includes the wavenumbers, where most of the organic substances have their Raman peaks. It is a region rich in information that is usually, or better has usually been, used for RS studies. However, this region is susceptible for interfering signal background generated, for example, from the fibre optic itself. This urges the need to use strong filters and retrospective spectrum corrections. Furthermore, the spectrum intensities in this wavenumber region have low intensities involving the need for long measuring times to get a clear and usable spectrum. This is complicated in the daily clinical use because of potential sample dehydration and complicated use for the real-time scanning utilization.⁹¹

The so-called silent region is between 2000cm^{-1} and 2800cm^{-1} , no essential information, no peaks from biological material, can be found here.⁹² Some studies found that alkyne has a major peak in the silent region which can be used in specific analyses with Raman microscopy as a tagging substance to target special molecules.⁹²

The high wavenumber region (HWNR) is often used in literature for its prominent differences between molecular groups. The region between 2800cm^{-1} and 3000cm^{-1} is known for its identification of aromatic and aliphatic hydrogens in carbohydrates (differences in fatty acids and sugar) which is important for better knowledge of cell density as well as the relation between cell membrane towards cytoplasm. Some literatures describe this region already from 2400cm^{-1} on and going to 3800cm^{-1} .^{91,93} The HWNR includes enough information for correct tissue recognition and is, because of its stability,

easier usable in the practical clinical routine. This can be observed in the frequent use of the HWNR in divers recent studies.^{94,95,96}

Since we are here testing the use of RS in a new, experimental clinical setting we are considering the fingerprint region, the silent region as well as the high wavenumber region. Furthermore, we omit the region below 400cm⁻¹ in our analysis, not only because of its low information input but also because of the interference with the aluminium spectrum. Metallic aluminium has a negligent spectrum but the oxide form has a small spectrum in the wavenumber region below 900cm⁻¹ (figure7).^{61,97}

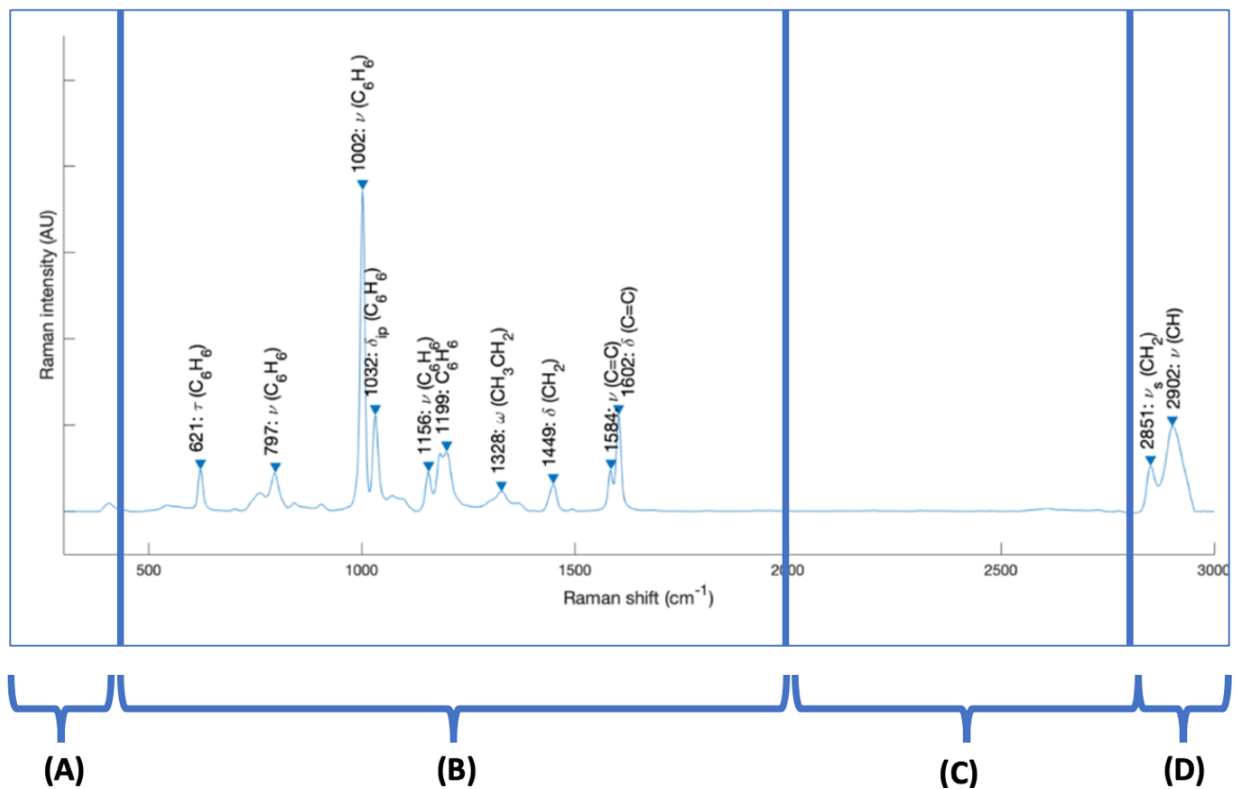


Figure19: Raman spectrum of polystyrene divided into the different spectral regions. **(A)** Low wavenumber region (10cm⁻¹- 400cm⁻¹), **(B)** Fingerprint region (400cm⁻¹- 2000cm⁻¹), **(C)** Silent region (2000cm⁻¹- 2800cm⁻¹), **(D)** High wavenumber region (2800cm⁻¹- 3000cm⁻¹). The X-axis represents the Raman shift (cm⁻¹) and the Y-axis the Raman intensity. Figure source: own production. Figure produced with Solais™.

4.4.4 Statistical tests

The here enclosed *figure20*, extracted from analyses regarding the meningioma and dura mater differentiation by RS (see results) shows a graphical interpretation of the used significance calculation by a Wilcoxon-Mann-Whitney-U test and a Bonferroni-corrected p-value.



Figure20: (a) Average spectra with the individual standard deviations of meningioma and dura mater measurements. A spectral difference can be observed; (b) Subtraction of the mean dura mater spectrum from the mean meningioma spectrum; (c) Significance at each single Raman shift (0=null hypothesis, 1=alternative hypothesis) calculated using Wilcoxon-Mann-Whitney-U test, p-value is Bonferroni-corrected, resulting in $p \leq 6 \times 10^{-6}$. Multiple significant differences can be observed. Figure source: Jelke, Mirizzi et al. 2021; Scientific-reports 2021, "Reproduced with permission from Springer Nature" ⁷⁵

To better illustrate the possible distinction between the two samples, in this case meningioma and dura mater, the mean spectra with their corresponding standard deviation are used. A difference spectrum is then created by subtracting one sample from the other, in this case again subtracting the dura mater spectrum from the meningioma spectrum. Significance is calculated for each Raman shift to determine if one spectrum (for example the spectrum of dura mater) is significantly different from the other spectrum (for example the spectrum of meningioma). It is calculated using a Wilcoxon-Mann-Whitney-U test. This test is similar to the independent t-test but is performed for ordinal, ranked data.⁹⁸ It is used to find differences between two independent groups. We map the H-values oscillating between 0 and 1. In this case 0 stands for no significant difference between the tumor and the dura mater peaks and 1 represents the alternative hypothesis, dura mater and meningioma peaks are significantly different.

The p-value is Bonferroni-corrected with an underlying number of 1603 compared pairs (corresponding to the device-inherent measurement number per spectrum). The standardly used p-value of 0,01 is divided by 1603 resulting in a new p-value of 6×10^{-6} , which allows better statistical analysis. The Bonferroni correction is applied when multiple statistical analyses are performed on the same data set to avoid type I errors (wrong rejection of a correct 0 hypothesis) to occur.⁹⁹

For a more accurate statistical evaluation, as well as machine learning stability, the data are split throughout the study into a training and a validation set. The splitting is performed on patient level meaning that all Raman scans from one patient are present in only one of the two groups. The division is performed using a random split. The training set is used to form the TSNE. The accuracy is validated by a five-fold-cross validation and an external validation data set. A five-fold-cross validation and an external validation data set are used to validate the accuracy of the statistical tests as well as the machine learning results. A 5-fold cross validation can be described as followed (Jelke, Mirizzi et al. 2021): *“For the 5-fold cross validation, a test set containing 1/5th of the randomized spectra was split from the data, and the classifier was trained on the remaining 4/5th of the data. The classifier performance was then evaluated on the held-out unseen test set. This procedure was repeated 5 times until all data was used once for testing.”*⁷⁵ An external validation data set is a collection of data which are not used for training of the classifier.

4.4.5 Sample evaluation

At the beginning of the study, a close look was put on the diverse wavenumbers trying to find prominent differentiations in the Raman spectrum, appearance or disappearance of peaks. Since we know what we are scanning (retrospective analysis with the detailed pathological diagnosis), we try to find unique peaks for each sample. We look into the already existing literature, regarding the biochemical attribution to specific wavelengths.¹⁰⁰ We make our own Raman library by including the references of the already existing literature as well as our own findings. This allows to manually retrace the biochemical background of a specific sample and as a conclusion to show which wavenumber regions, which peaks are characteristic for a certain tissue. In the course of the study this knowledge is essential for knowing on what kind of peaks, peak differences or changings in signal, the classifier should be trained on. Having an exact idea of the biochemical composition of the, in this case, analysed CNS tissue samples, opens the door for a precise use of RS.

A specific example is the differentiation between dura mater and meningioma by their dissimilar amount of collagen content and lipids. Literature describes a higher collagen content for dura mater than for meningioma.^{101,102} Collagen is made of protein chains which are constituted out of different amino acids like glycine, proline and hydroxyproline, represented by the specific peaks at 815cm^{-1} , 855cm^{-1} , 876cm^{-1} , 938cm^{-1} , 1003cm^{-1} , 1033cm^{-1} , 1250cm^{-1} , 1319cm^{-1} , 1450cm^{-1} , 1663cm^{-1} .^{103,104}

The peaks at 815cm^{-1} , 885cm^{-1} , 876cm^{-1} and 938cm^{-1} can be assigned to collagen type I and IV and represent (hydroxy-) proline which is an important composition of collagen.¹⁰⁰ 1003cm^{-1} and 1033cm^{-1} are assigned to phenylalanine and 1250cm^{-1} represents amide III, both amino acids of collagen. The CH_2CH_3 deformation described in literature as a collagen assignment, is visible at the peaks of 1319cm^{-1} and 1450cm^{-1} . At last, 1663cm^{-1} stands for proteins, including collagen type I.

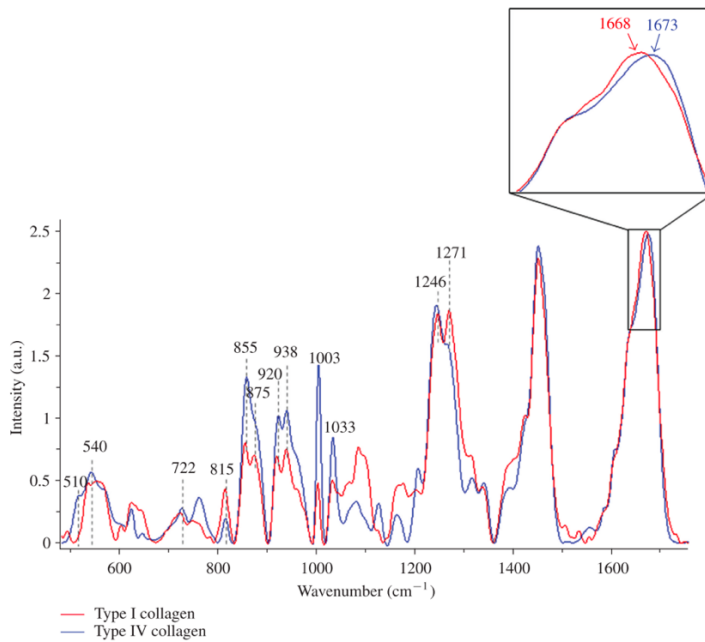


Figure21: Comparative spectrum of collagen type I and IV. X-axis corresponds to the wavenumbers (cm^{-1}) and the Y-axis corresponds to the Raman intensity. Figure source: Nguyen et al. 2013, “Characterization of type I and IV collagens by Raman microspectroscopy: Identification of spectral markers of the dermo-epidermal junction”.¹⁰⁴

In order to verify this hypothesis (collagen is a differentiating factor for dura mater and meningioma), a collagenase experiment is performed. See section 5.2.. We try to remove the before found collagen peaks from the dura mater spectrum by putting a piece of dura mater in a solution containing a collagenase (*figure34*). We measure the sample natively, after 15h of collagenase exposure and after 19h of collagenase exposure.

A similar experiment as for collagen is repeated for the lipid contribution. We base our specific peaks on multiple literature researches (*figure35*). For the general lipid peaks 1260cm^{-1} , 1300cm^{-1} , 1440cm^{-1} , 1656cm^{-1} , 1734cm^{-1} are used.¹⁰³ For sphingomyelin we use 1437cm^{-1} , 1654cm^{-1} , 1670cm^{-1} , 2847cm^{-1} , 2880cm^{-1} , 2959cm^{-1} and 760cm^{-1} ; 1442cm^{-1} , 1657cm^{-1} , 1737cm^{-1} , 2847cm^{-1} , 2882cm^{-1} , 2920cm^{-1} , 2959cm^{-1} , 3007cm^{-1} for phosphatidylethanolamine.¹⁰⁵ For cholesterol we take 418cm^{-1} , 421cm^{-1} , 457cm^{-1} , 549cm^{-1} , 608cm^{-1} , 700cm^{-1} , 702cm^{-1} , 703cm^{-1} , 746cm^{-1} , 759cm^{-1} , 853cm^{-1} , 881cm^{-1} , 957cm^{-1} , 962cm^{-1} , 1132cm^{-1} , 1179cm^{-1} , 1300cm^{-1} , 1440cm^{-1} , 1441cm^{-1} , 1444cm^{-1} , 1659cm^{-1} , 1661cm^{-1} , 1670cm^{-1} , 1674cm^{-1} , 2970cm^{-1} and for cholesterol ester 428cm^{-1} , 538cm^{-1} , 614cm^{-1} , 702cm^{-1} , 1065cm^{-1} , 1131cm^{-1} , 1296cm^{-1} , 1441cm^{-1} , 1669cm^{-1} , 1670cm^{-1} , 1739cm^{-1} , 2970cm^{-1} .^{106,107}

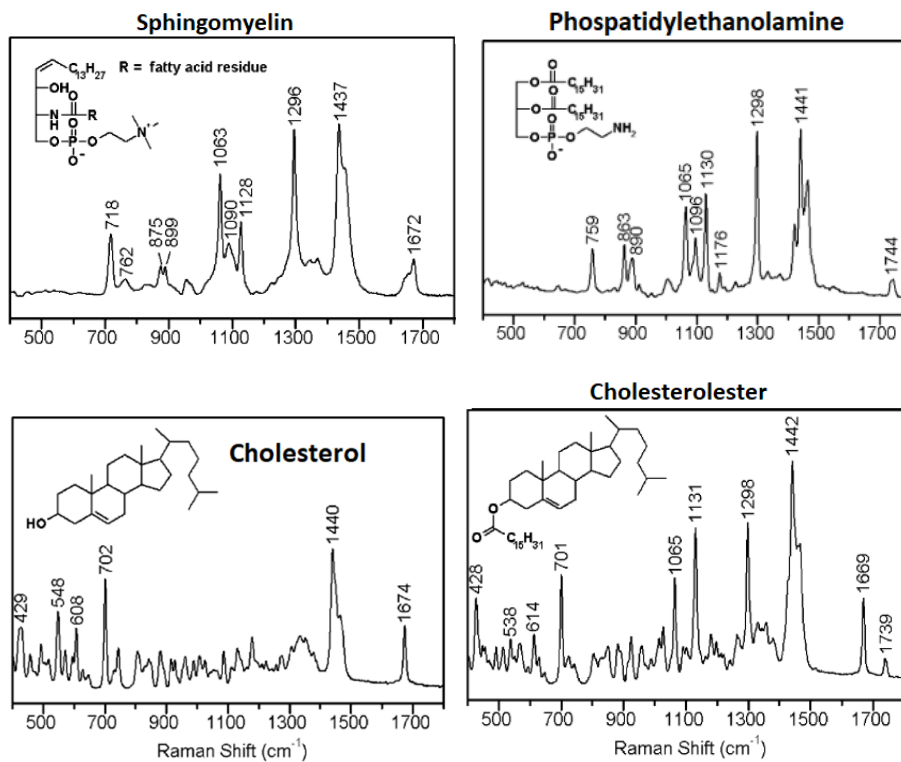


Figure22: Spectra of different lipids: Spingomyelin, phosphatidylethanolamine, cholesterol and cholesterol ester. Figure source: by Krafft et al.2005, "Near infrared Raman spectra of human brain lipids" .¹⁰⁷

Furthermore, the working group started to produce an own Raman peak library of basic components like glucose (*figure23*). These spectra were also used for spectral comparison.

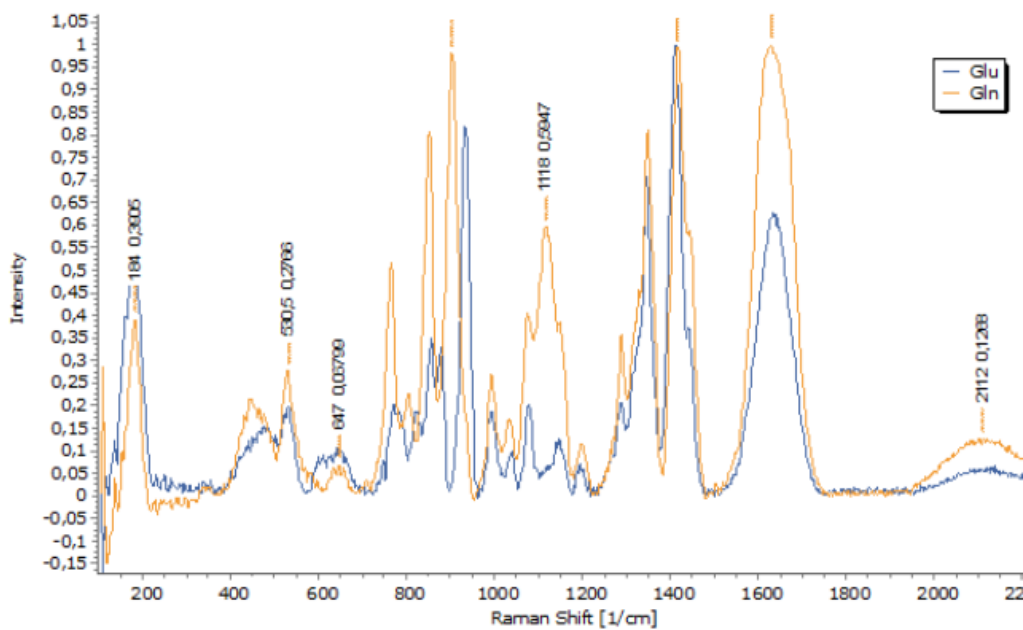


Figure23: Raman spectrum of glucose (Glu, blue line) and glutamine (Gln, orange line). Figure source: Project of B.M. and F.K. X-axis represents the Raman shift (cm^{-1}) and the Y-axis represents the Raman intensity.

5 Results

5.1 Fixation Study

For quickly improving RS based machine learning and to build an eventual omni-class classifier in the future, more and more tissue/tumor samples as well as rare tumor entities should be included. In order to incorporate all these samples, it is mandatory to have a closer look on the induced changes, the influences of common fixation techniques. In this study we choose to analyse formalin fixation as well as cryofixation by dry ice.

5.1.1 Statistics

Table1 gives an overview of all included samples, a total of 40 patients and 1165 measuring points. Not all samples are integrated in the here following analyses. We principally use metastasis of ovarian cancer, CNS metastasis of unknown primary, dura mater, glioblastoma, ganglioma, meningothelial meningioma, necrosis, modified CNS tissue and oligodendroglioma. The patients were between 18 and 87 years old.

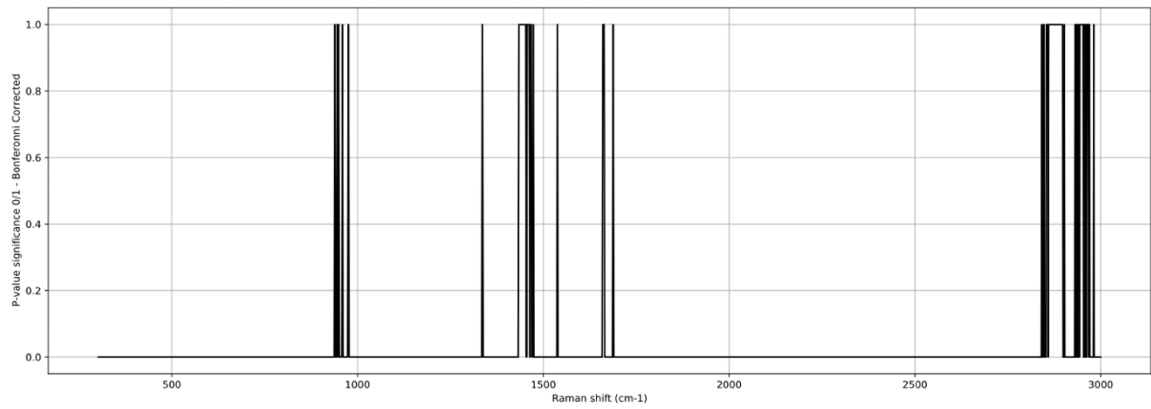
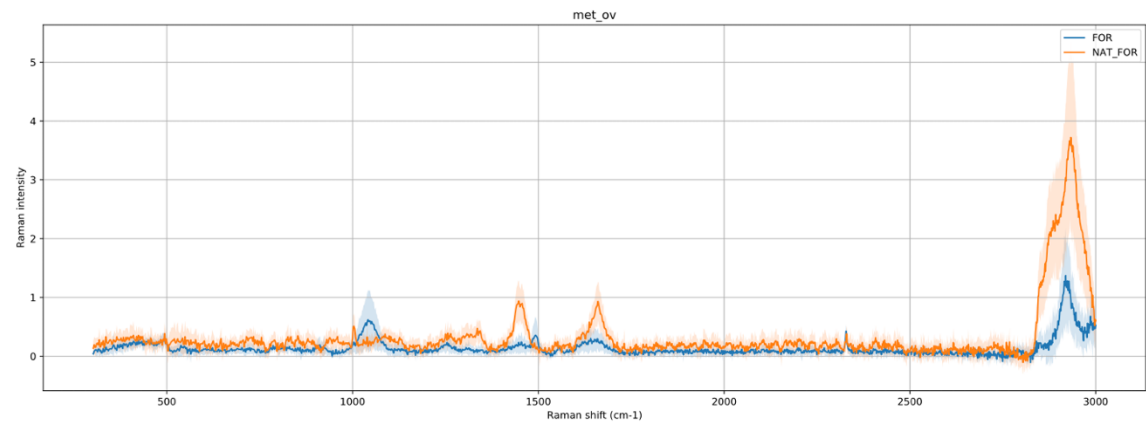
Diagnosis	Fixation-State			
	NAT_FOR	FOR	NAT_FRO	FRO
Glioblastoma	108MP	55MP	27MP	34MP
Muscle	6MP	9MP	0MP	0MP
Necrosis	7MP	5MP	0MP	0MP
Modified CNS	63MP	96MP	9MP	21MP
Oligodendroglioma	51MP	63MP	23MP	24MP
Diffuse astrocytoma	11MP	16MP	0MP	0MP
Pilocytic astrocytoma	9MP	14MP	0MP	0MP
Ganglioma	13MP	13MP	0MP	0MP
Metastasis-Total	29MP	12MP	18MP	19MP
Metastasis of pulmonary cancer	14MP	3MP	0MP	0MP
Metastasis of ovarian cancer	15MP	9MP	0MP	0MP
CNS Metastasis of unknown primary	0MP	0MP	18MP	19MP
Meningioma-Total	114MP	131MP	21MP	43MP
Meningothelial meningioma	29MP	33MP	21MP	43MP
Transitional meningioma	70MP	80MP	0MP	0MP
Atypical meningioma	6MP	4MP	0MP	0MP
Fibrous meningioma	9MP	14MP	0MP	0MP
Dura mater	25MP	48MP	15MP	13MP
TOTAL	436MP	462MP	113MP	154MP

Table1: Data overview of the included patients and measuring points split by sample entity and fixation state. NAT_FOR corresponds to the native data which are afterwards formalin-fixed; FOR corresponds to the formalin-fixed data; NAT_FRO corresponds to the native data which are afterwards cryofixed; FRO corresponds to the cryofixed data. MP corresponds to 'measuring point'.

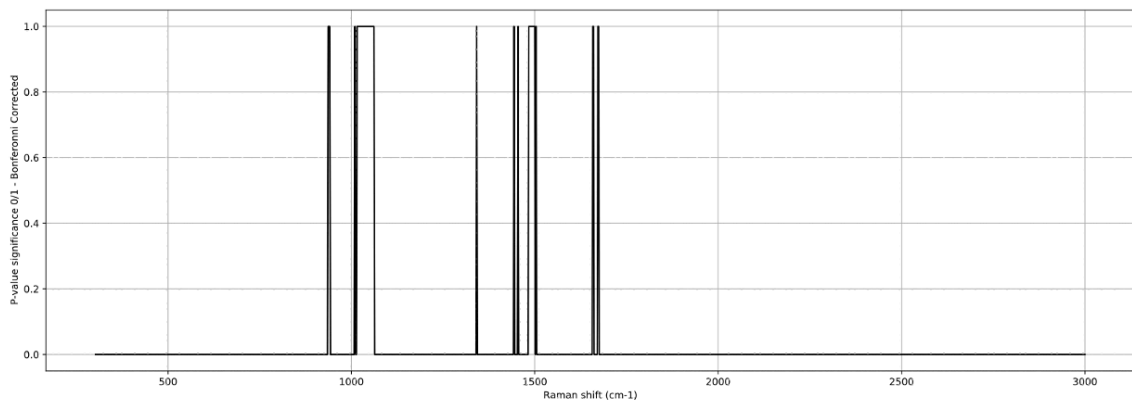
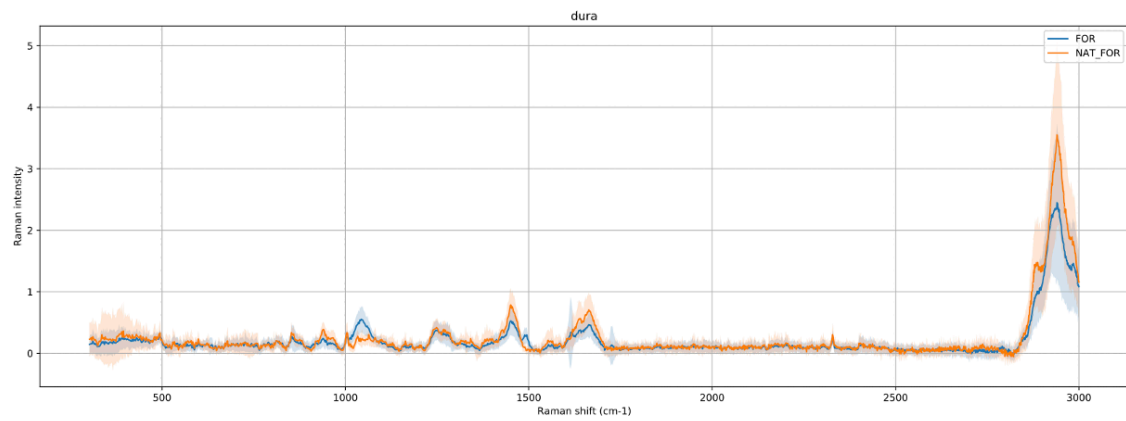
5.1.2 Fixation-study results

We compare the mean spectra of specific samples in different fixation states.

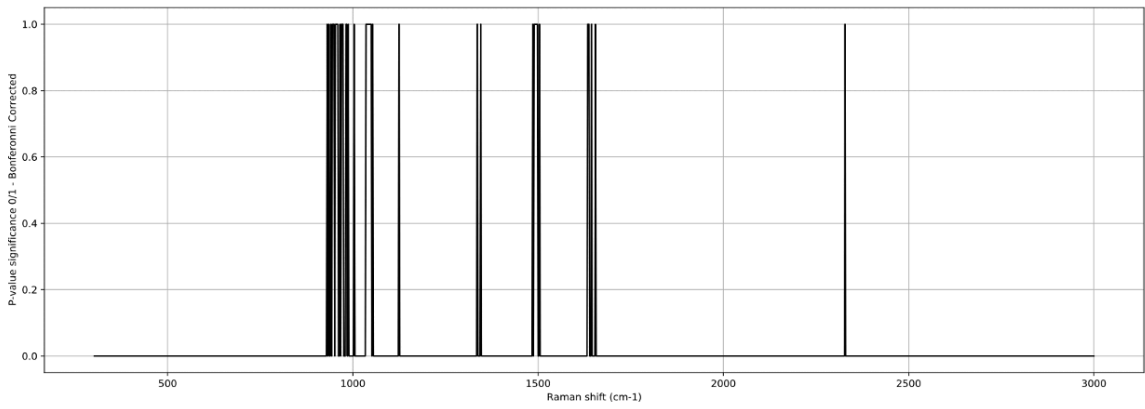
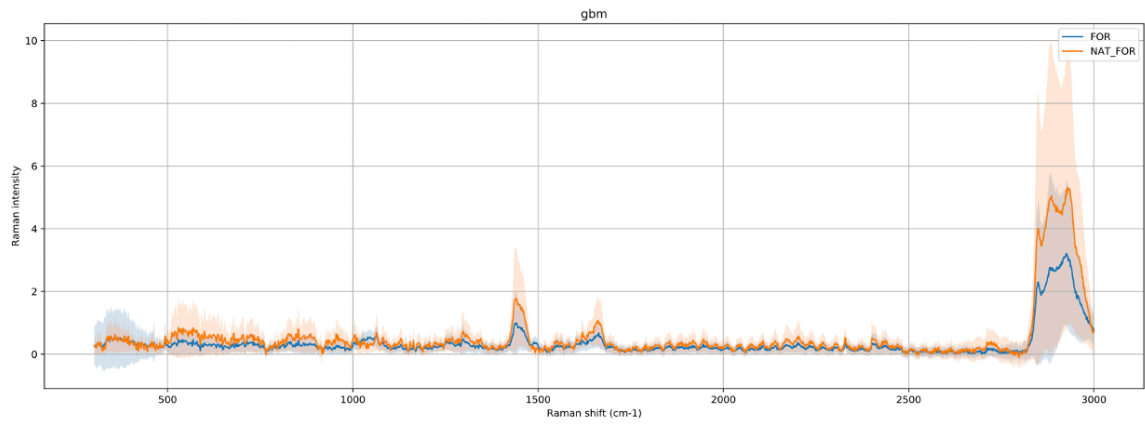
First, native versus formalin-fixed samples (metastasis of ovarian cancer, dura mater, glioblastoma, ganglioma, meningothelial meningioma and necrosis) are analysed. *Figure24 A-F*.



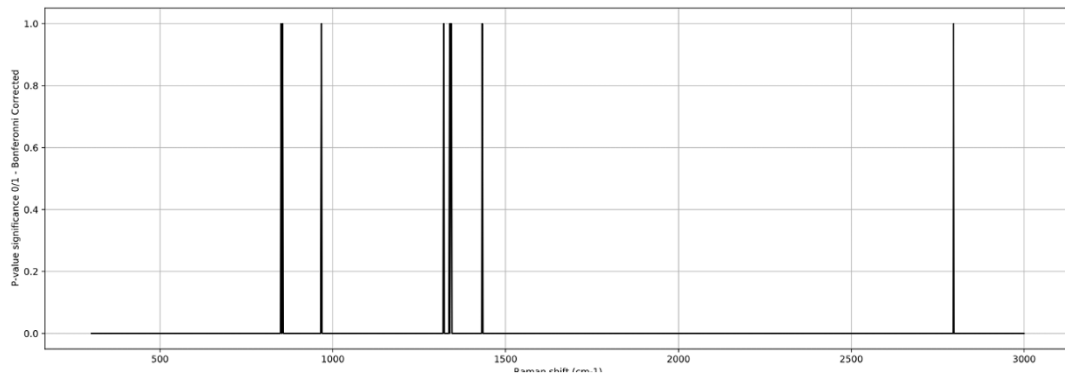
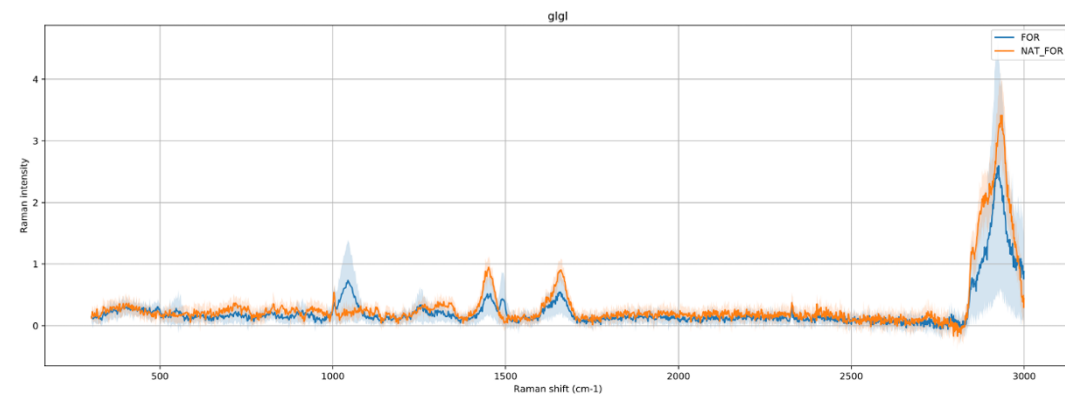
(A) Metastasis of ovarian cancer



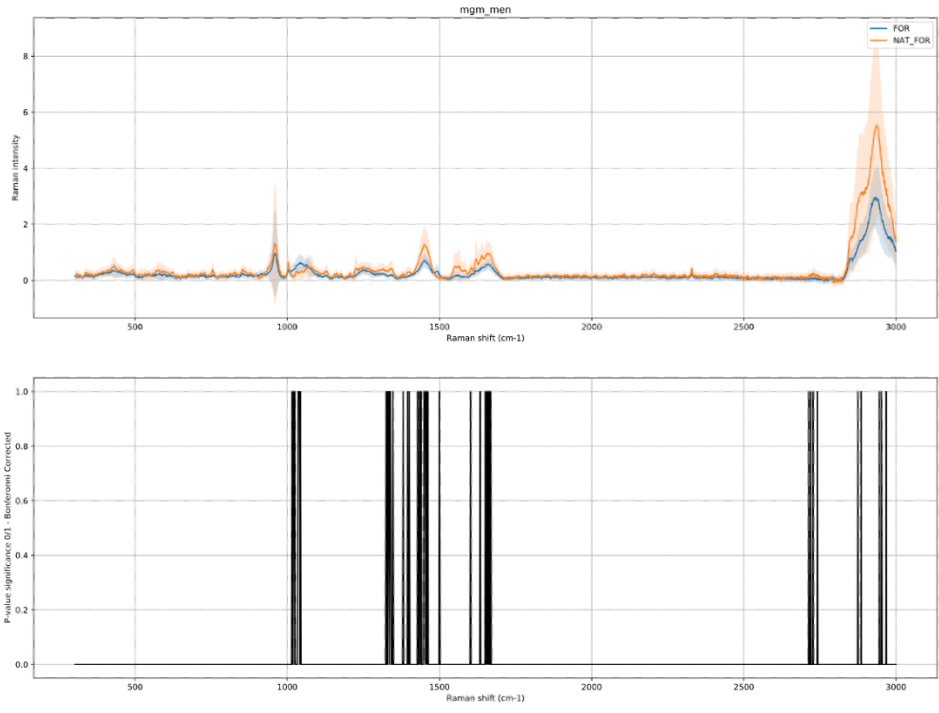
(B) Dura mater



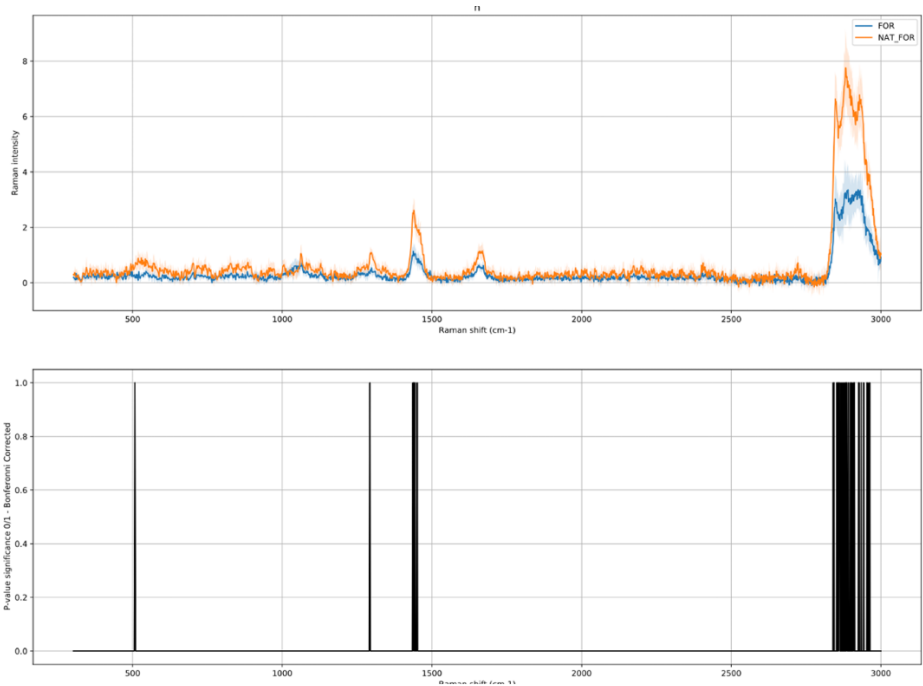
(C) Glioblastoma



(D) Glioma



(E) Meningothelial meningioma

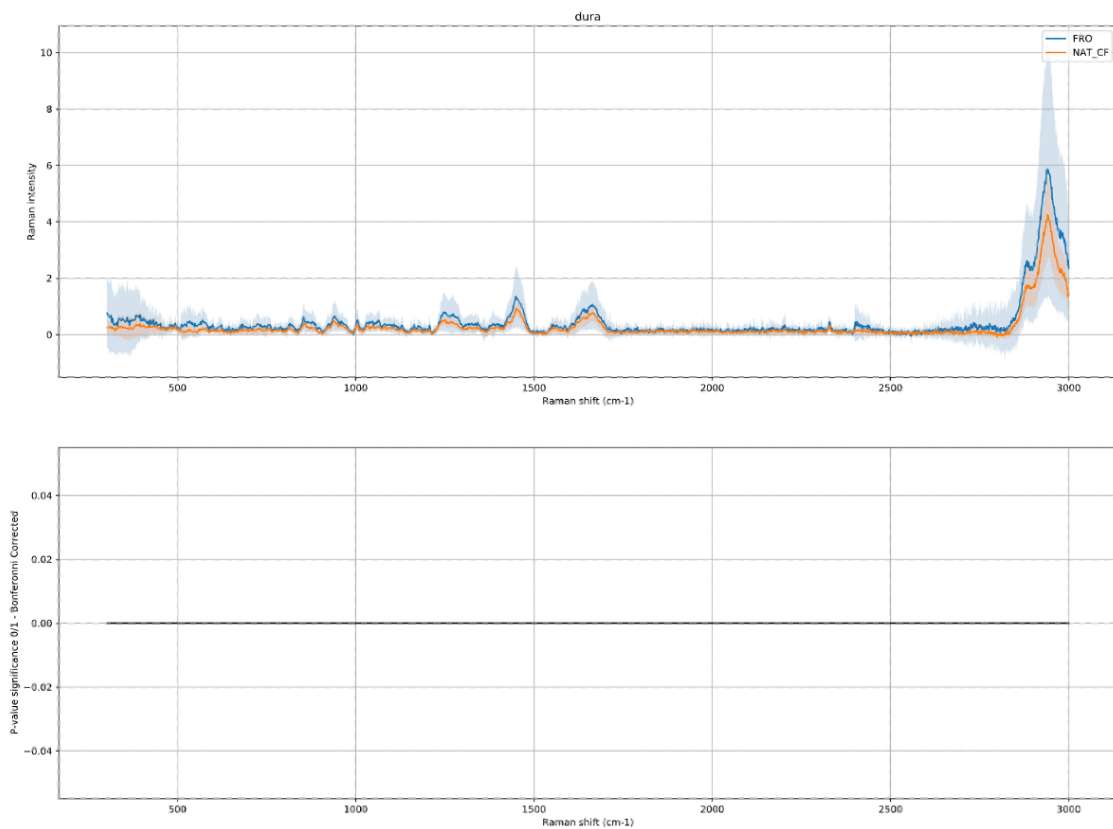


(F) Necrosis

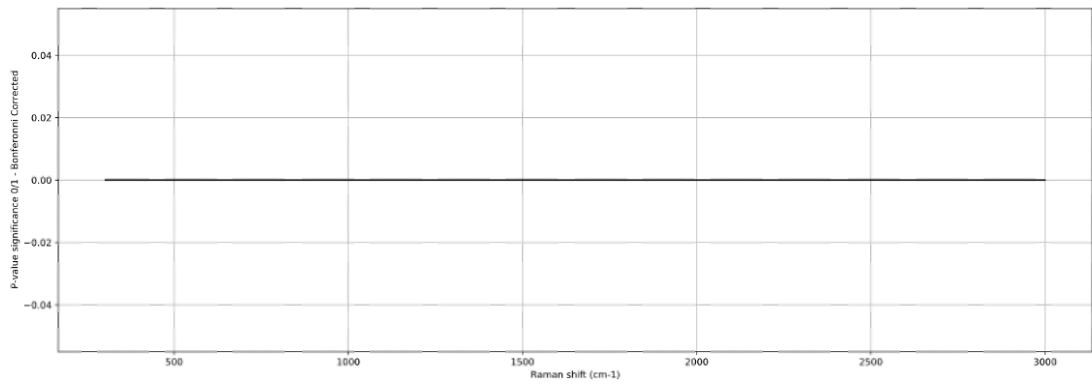
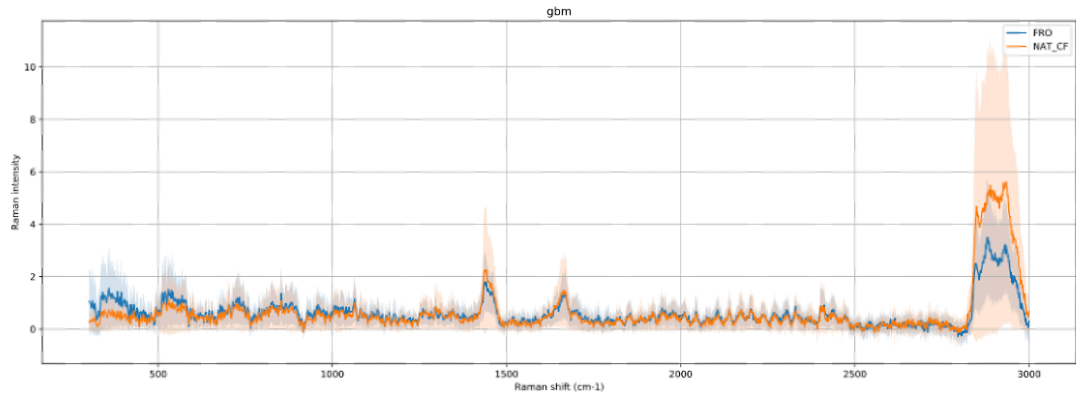
Figure24: Top of each subfigure: Mean spectra of native versus formalin-fixed metastasis of ovarian cancer (A), dura mater (B), glioblastoma (C), ganglioma (D), meningothelial meningioma (E) and necrosis (F). X-axis represents the Raman shift (cm⁻¹) and the Y-axis represents the Raman intensity. Bottom of each subfigure: Significance calculation of differences between the native and the formalin-fixed mean spectra. The black lines indicate the significant difference. X-axis represents the Raman shift (cm⁻¹) and the Y-axis represents the p-value (significance 0/1, Bonferroni-corrected). Multiple alternating spectral differences can be observed. Figure source: own production. Figure produced with Solais™ and Matlab®.

Formalin-fixation induces different changes depending on the sample's entity and its molecular composition. This means that the spectra of the different tissue entities are altered in an individual manner. In (A), the significant differences (represented by the black lines) are at around 950cm^{-1} , 1350cm^{-1} , 1400cm^{-1} , 1550cm^{-1} , 1600cm^{-1} , 2800cm^{-1} - 3000cm^{-1} . In (B) they are at mostly located between 900cm^{-1} and 1700cm^{-1} . 900cm^{-1} – 1600cm^{-1} with one supplement peak at 2300cm^{-1} represent the spectral differences in (C) and 800cm^{-1} , 1000cm^{-1} , 1300cm^{-1} - 1450cm^{-1} with one supplement peak at 2750cm^{-1} in (D). In (E) the peaks are prominently located from 1000cm^{-1} to 1700cm^{-1} and from 2700cm^{-1} to 3000cm^{-1} . At last, some few peaks at 500cm^{-1} , 1300cm^{-1} , 1450cm^{-1} with a higher intensity of peaks from ca. 2800cm^{-1} to 3000cm^{-1} in (F) are again different wavenumbers where the significant difference lines are represented. Formalin-fixation is introducing changes in each sample and individual for each entity.

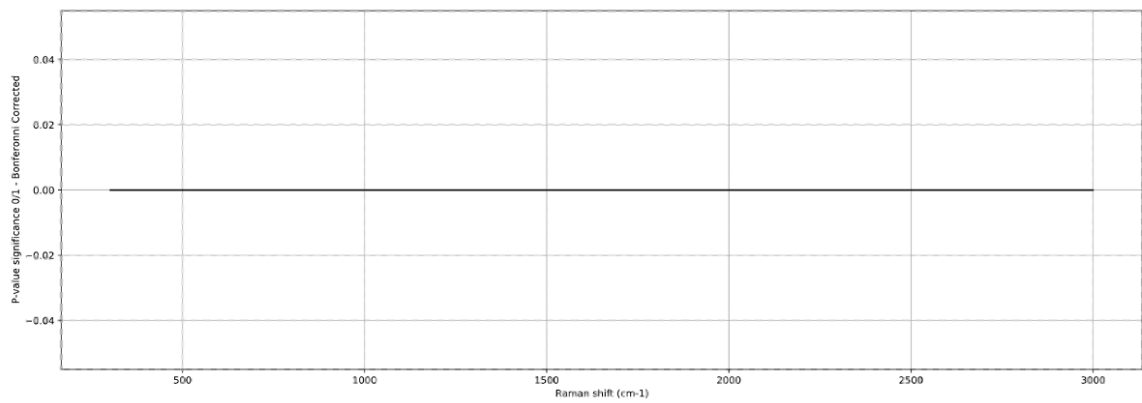
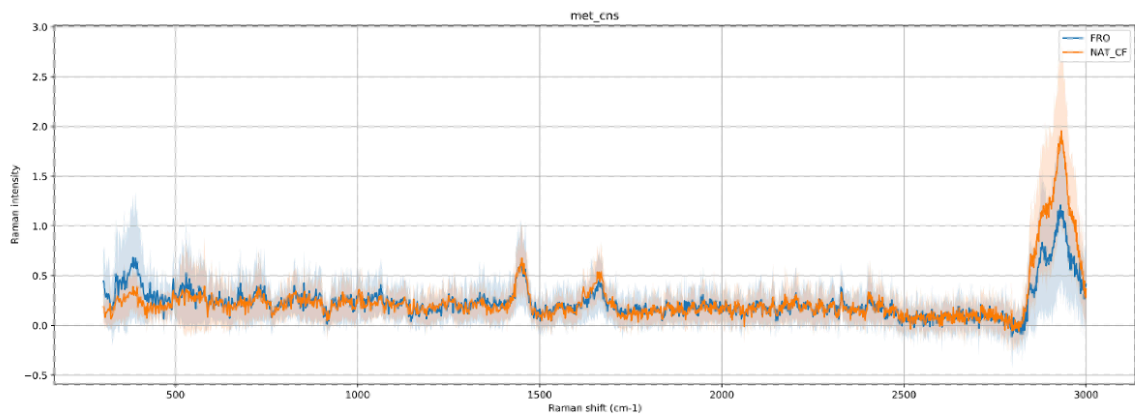
Second, we compare native and cryopreserved samples (*figure25*). Here we use the differentiation of dura mater, glioblastoma, CNS metastasis of unknown primary, meningothelial meningioma, modified CNS tissue and oligodendroglioma.



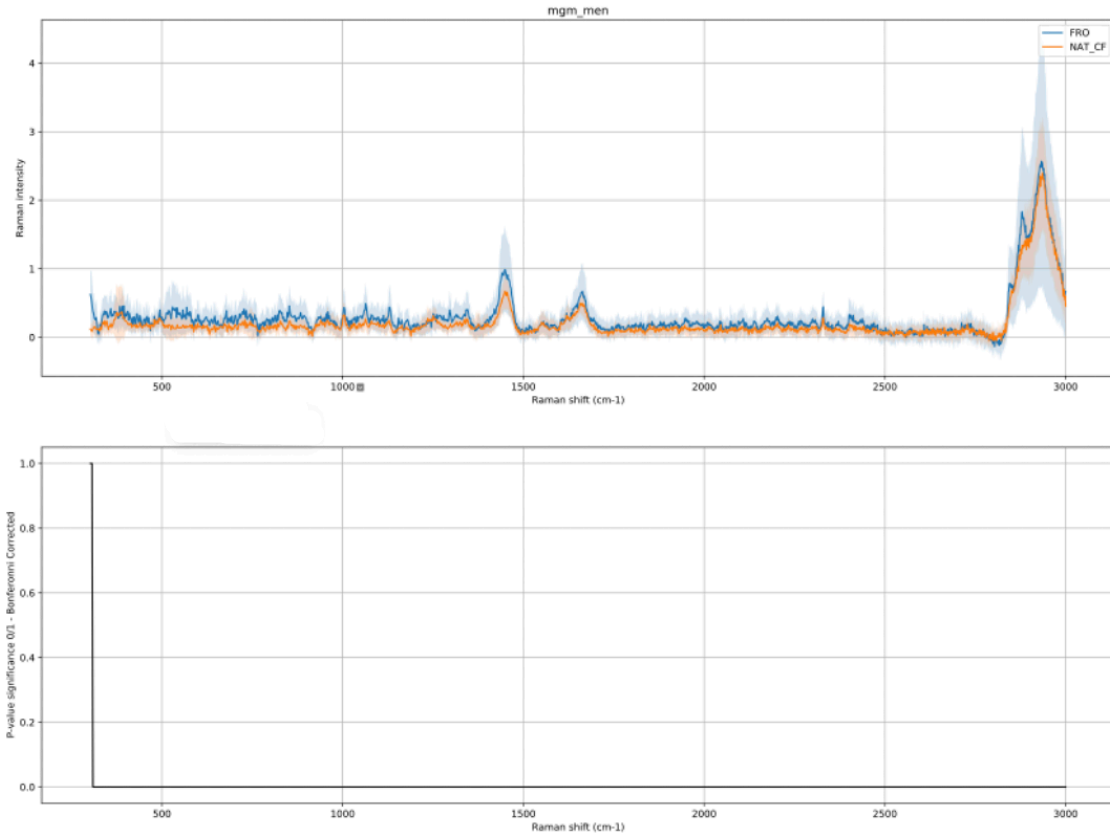
(A) Dura mater



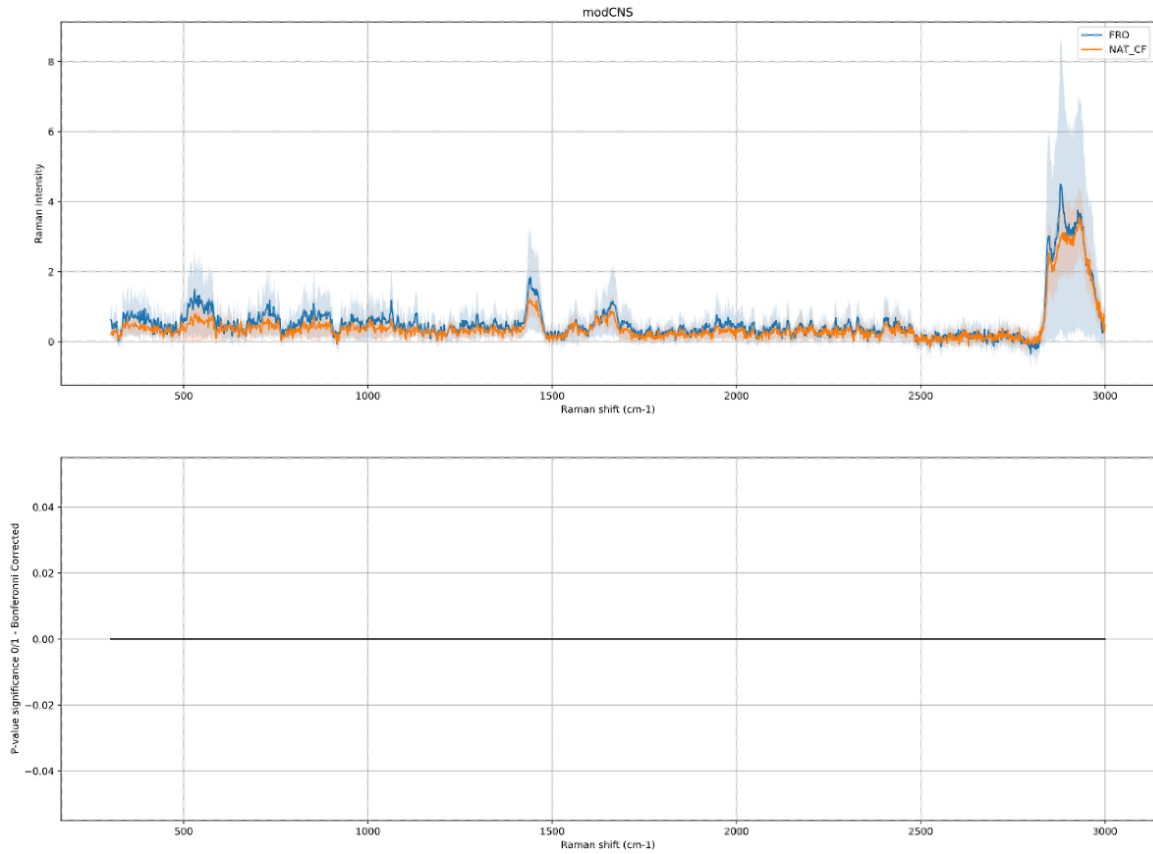
(B) Glioblastoma



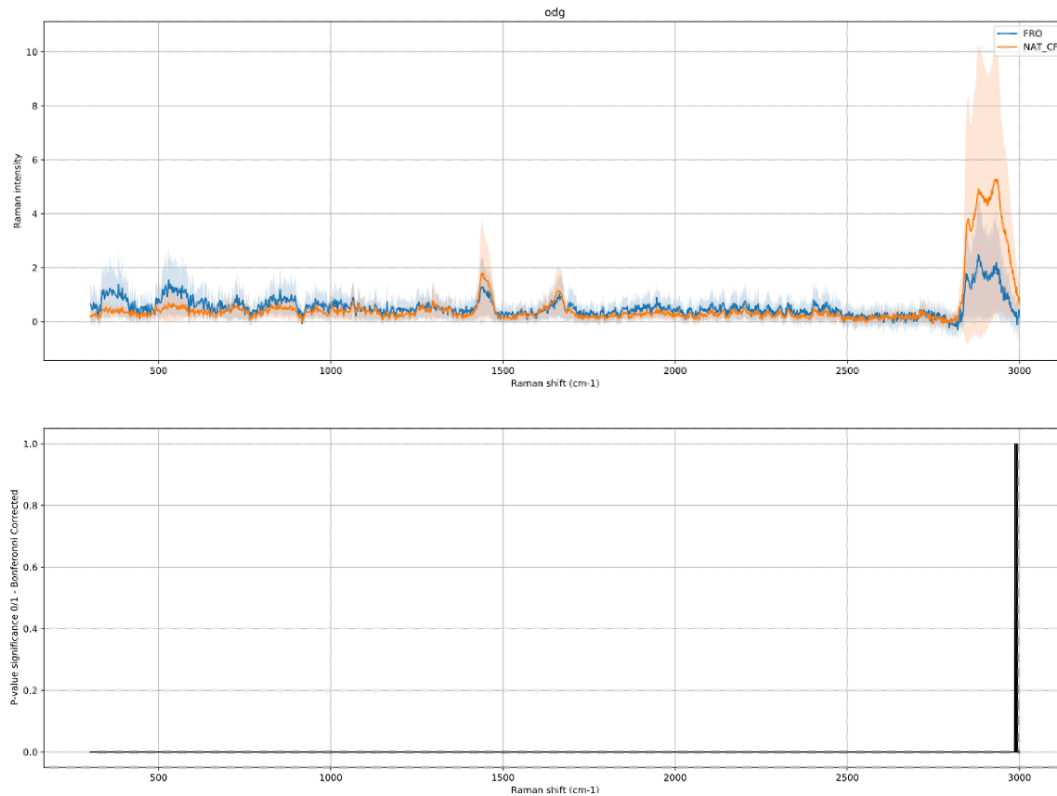
(C) Metastasis



(D) Meningothelial meningioma



(E) Modified CNS tissue



(F) Oligodendroglioma

Figure25: Top of each subfigure: Mean spectra of native versus cryofixed dura mater (A), glioblastoma (B), CNS metastasis of unknown primary (C), meningothelial meningioma (D), modified CNS tissue (E) and oligodendroglioma (F). X-axis represents the Raman shift (cm^{-1}) and the Y-axis represents the Raman intensity. Bottom of each subfigure: Significance calculation of differences between the native and the cryofixed mean spectra. The black lines indicate a significant difference. X-axis represents the Raman shift (cm^{-1}) and the Y-axis represents the p-value (significance 0/1, Bonferroni-corrected). No spectral differences can be overserved. Figure source: own production. Figure produced with Solais™ and Matlab®.

No significant changes between the compared mean spectra can be observed.

For verification of the before mentioned results, an already trained dualclass (meningioma and dura mater)-classifier (see section 5.2.) will be applied on fixed meningioma and dura mater samples (*figure26*).

Application of externally trained Meningioma-Dura SVM Model (InfZo-filtered)

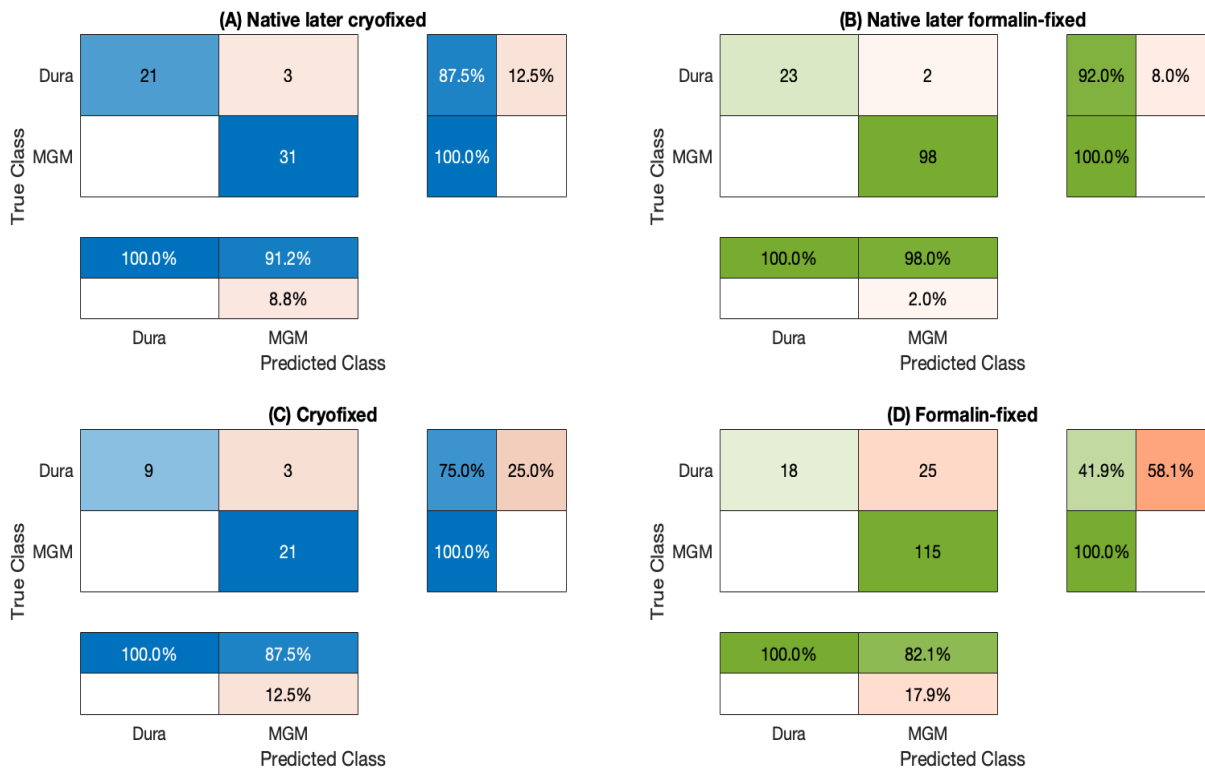


Figure26: SVM-classifier results. **(A)** Trained MGM-dura mater classifier applied on native MGM and dura mater samples corresponding to (C). Sensitivity of 100% and a specificity of 87,5% **(B)** Trained MGM-dura mater classifier applied on native MGM and dura mater samples corresponding to (D). Sensitivity of 100% and a specificity of 92,0% **(C)** Trained MGM-dura mater classifier applied on cryofixed MGM and dura mater samples. Sensitivity of 100% and a specificity of 75%. **(D)** Trained MGM-dura mater classifier applied on formalin-fixed MGM and dura mater samples. Sensitivity of 100% and a specificity of 41,9%. Figure source: own production. Figure produced with Matlab®.

In *figure26* a classifier performance with a sensitivity of 100% and a specificity of 75% on the cryofixed samples can be observed. The classifier performance diminishes when applied on formalin data (sensitivity of 100% and a specificity of 41,9%). *Figure27* represents a subtraction spectrum. The pure formalin spectrum is subtracted from the analysed formalin-fixed tissue spectrum. A significant improvement of the classifier performance (specificity of 62,8% and of sensitivity 100%) can be observed. Nevertheless, the classifier results are underneath the ones from the native data. A new classifier based on the 'difference spectrum data', meaning the formalin-fixed meningioma and dura mater data which are subtracted by the pure formalin spectrum is trained. A slight classifier improvement can be observed (specificity of 66,7% and sensitivity of 100%).

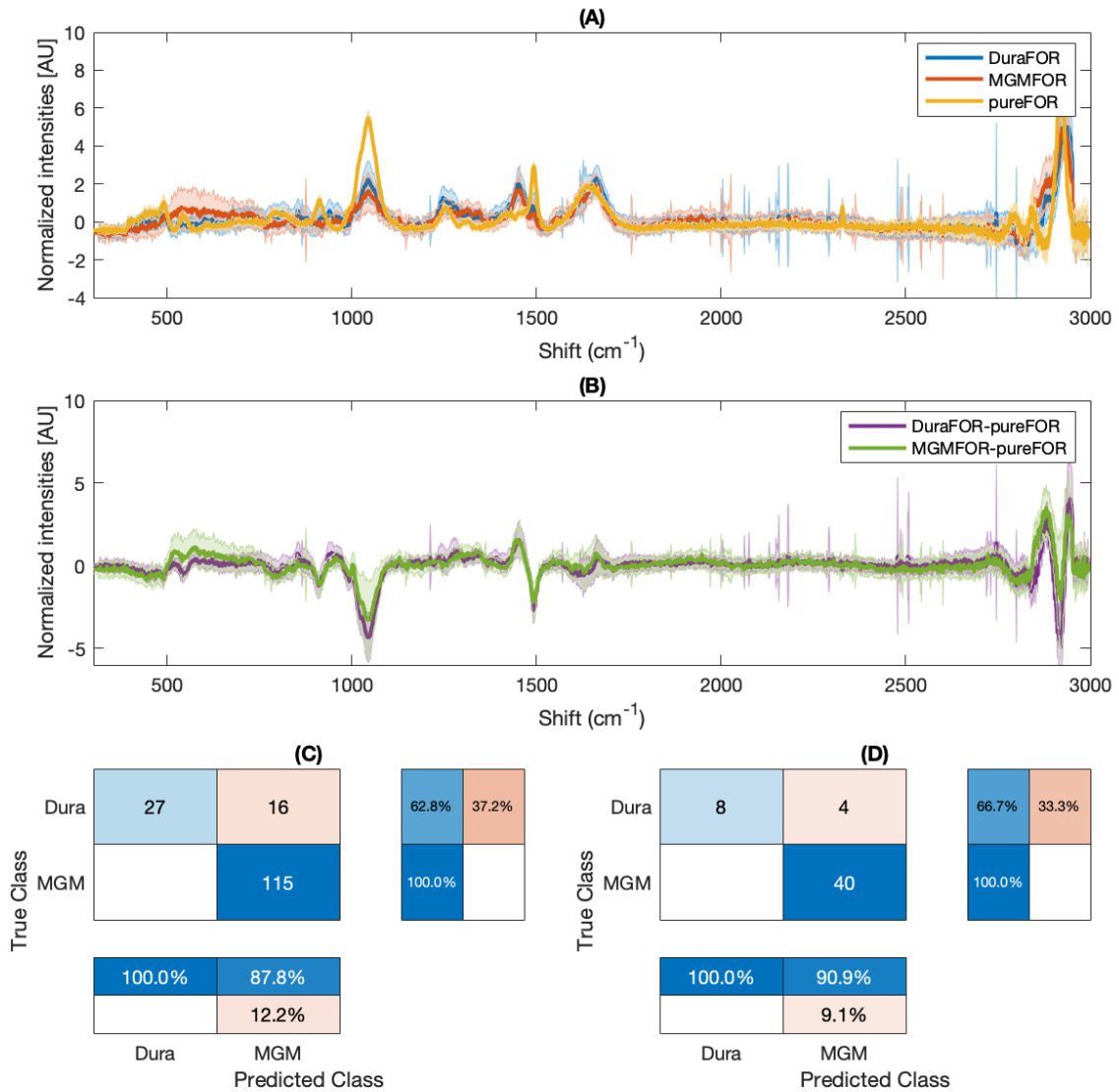


Figure 27: Classifier results when a natively trained classifier is applied on formalin-fixed data with the use of a correction-factor. **(A)** Mean spectra of formalin-fixed dura mater (blue), formalin-fixed meningioma (red) and pure formalin (orange). **(B)** Difference spectra once between formalin-fixed dura mater and pure formalin (purple) and once between formalin-fixed meningioma and pure formalin (green). **(C)** Results of the natively trained classifier used on spectra where the pure formalin spectrum was subtracted. Specificity of 62,8% and of sensitivity 100%. **(D)** Results of a newly trained classifier based on the spectra where the pure formalin spectrum was subtracted. Specificity of 66,7% and sensitivity of 100%. Figure source: own production. Figure produced with Matlab®.

5.1.3 Paper submission

We will submit these results to an adequate journal under the potential title of “Detection and analysis of cryopreserved and formalin-fixed neurosurgical samples by Raman spectroscopy”. The figures and diagrams as well as the here described results will be partly identical to the ones in the paper.

5.2 Meningioma-Study

The behaviour of RS in distinguishing meningioma and dura mater tissue is analysed in order to verify the possibility of successful identification of different tissue types by RS. Could RS be a good tool to detect the infiltration zone between healthy and malignant tissue cells? Distinguishing factors are represented at the biochemical level (different content of collagen and lipids) as well as by the training of a SVM classifier.

5.2.1 Statistics

In total 59 patients and 1268 measuring points are included in the meningioma study. In the enclosed table (*table2*) a precise enumeration of the here used number of patients as well as measuring points split by diagnosis is shown.

It is important to notice in *table2*, that no one-by-one addition of the patient number is possible since some of the dura mater patients are already included in the numbers of the meningioma subtypes. The dura mater samples have been extracted mostly during these tumor-operations.

Sample entity	Patients (n)	Measuring points (n)
Transitional meningioma	13	229
Meningothelial meningioma	19	251
Atypical meningioma	4	62
Fibrous meningioma	6	69
Meningioma, not otherwise specified	2	20
Secretory meningioma	1	14
Healthy dura mater	22	162
Tumor infiltration zone	Included in numbers above	460
Verification sample	1	108

Table2: Data overview of the included patients and measuring points split by sample entity. Since the samples of the 'infiltration zone' class are partly already introduced in the other subclasses, a simple adding on of each subclass to for the 'total' is not possible. Furthermore, some of the dura mater patients are already included in the numbers of the meningioma subtypes since the dura mater samples have been extracted mostly during these tumor-operations. All samples are measured natively.

5.2.2 Meningioma-study results

To analyse if a differentiation between dura mater and meningioma would be possible, the differences between the mean spectra of both entities are analysed. The meningiomas are furthermore divided into their subgroups. In *figure28* the differences of the entire spectrum can be observed. Below, certain zoomed-in intervals, which we consider as particularly important, are shown. The mean spectrum of dura mater is represented in red; the meningioma subtypes are multi-coloured. Furthermore, it is difficult to see a differentiation between the meningioma subtypes, which can and will be considered as one entity (meningioma) in the future.

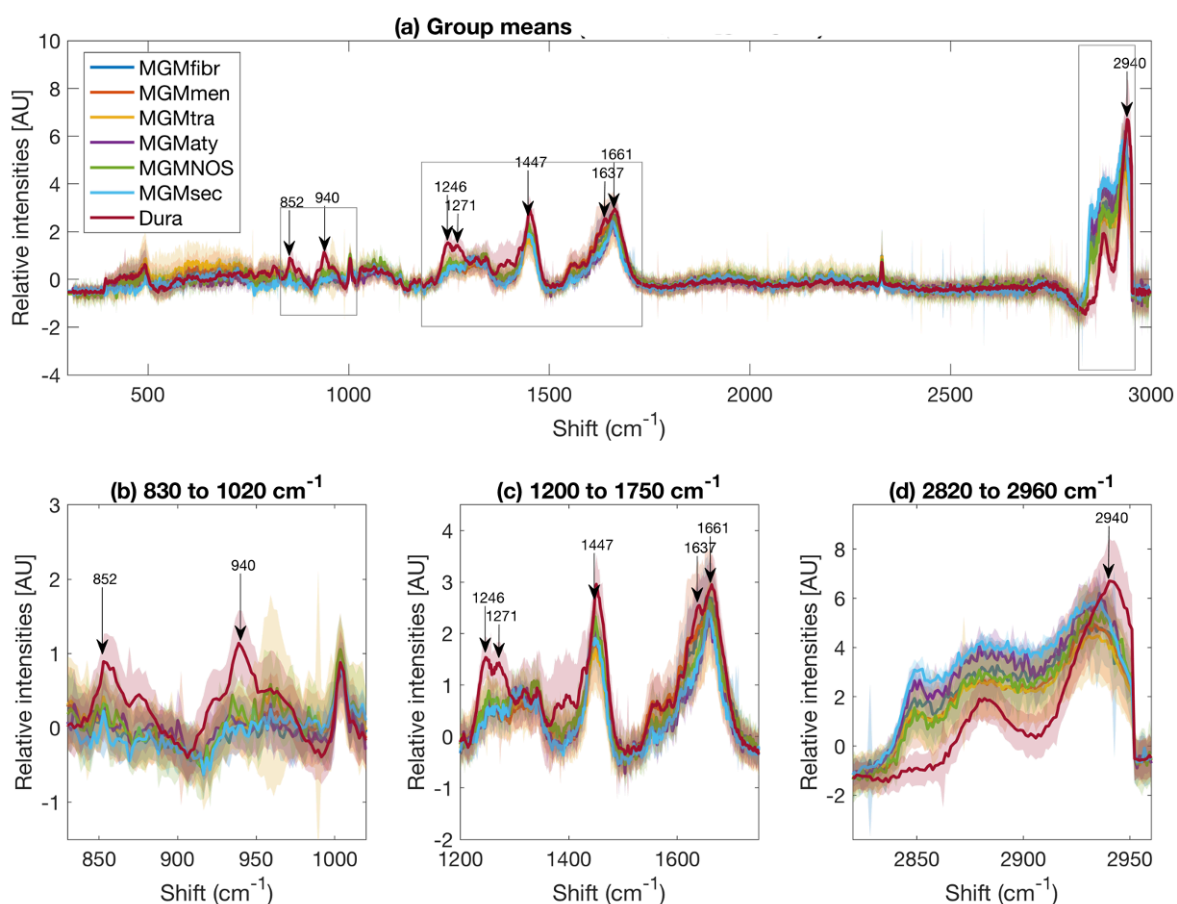


Figure28: (a) Mean spectrum underlaid by the standard deviation of dura mater and the different meningioma subtypes. (b) to (d): Zoomed-in intervals on the spectral differences between dura mater and meningioma subtypes. (b) Subintervals from 830 cm^{-1} to 1020 cm^{-1} , (c) Subintervals from 1200 cm^{-1} to 1750 cm^{-1} , (d) Subintervals from 2820 cm^{-1} to 2960 cm^{-1} . The arrows in (a) to (d) represent the distinctive peaks which rely on common collagen peaks. X-axis corresponds to the Raman shift (cm^{-1}) and the Y-axis corresponds to the Raman intensities. Figure source: Jelke, Mirizzi et al. 2021; Scientific-reports 2021, “Reproduced with permission from Springer Nature”⁷⁵

Afterwards a TSNE (*figure29*) is performed on these data. In *figure29*, two well separable clusters can be discerned (red dots correspond to dura mater, the coloured ones to meningioma samples). For a more precise analysis we considered the entire spectrum as well as a clustering over the HWNR. In *figure30*, we perform the same analysis as in *figure29* but this time patient-based to avoid any intra-patient confounders. Every dot-colour represents a different patient.

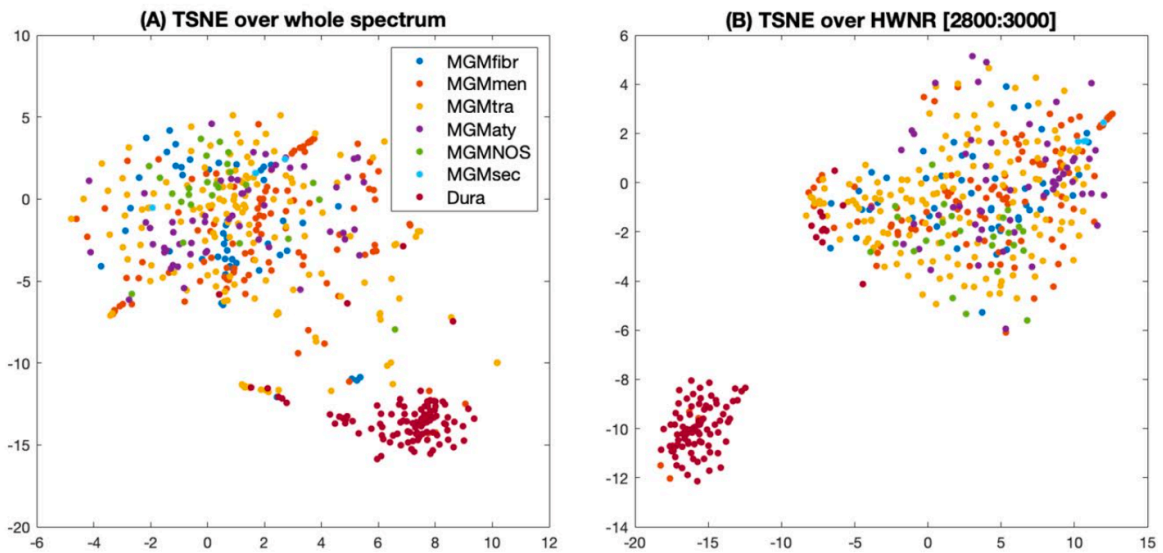


Figure29: (A) TSNE over the entire spectrum. **(B)** TSNE over the HWNR spectrum between dura mater (red dots) and meningioma subtypes (multi-coloured dots). A clear cluster-formation can be observed in (A) and (B). Figure source: Jelke, Mirizzi et al. 2021; Scientific-reports 2021, “Reproduced with permission from Springer Nature”⁷⁵

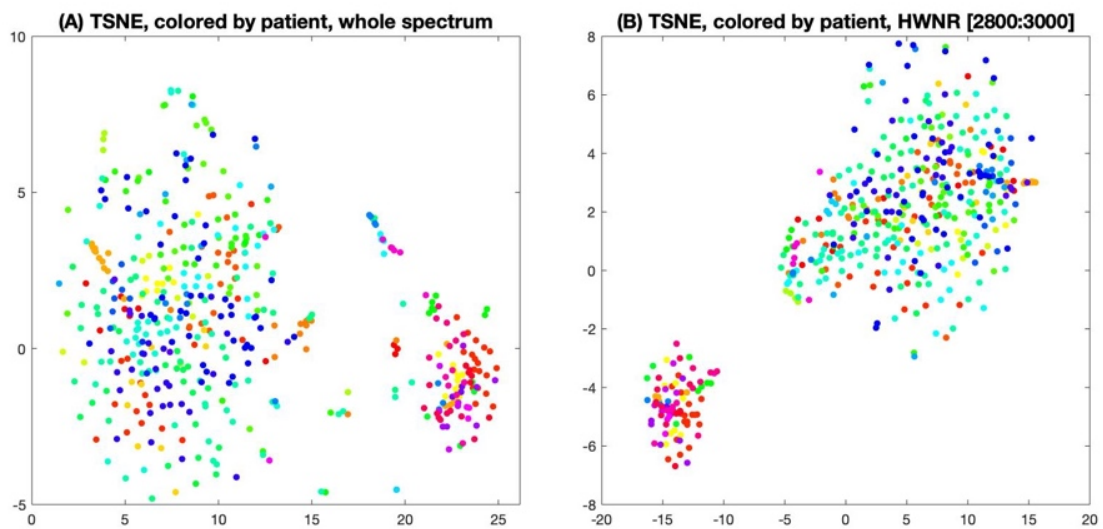


Figure30: (A) TSNE over the entire spectrum. **(B)** TSNE over the HWNR spectrum, patient-based. Every dot-colour represents a different patient. A clear cluster-formation can be observed in (A) and (B). The mixture of coloured dots excludes a cluster formation by patient. Figure source: Jelke, Mirizzi et al. 2021; Scientific-reports 2021, “Reproduced with permission from Springer Nature” ⁷⁵

Figure31 represents by arrows the before mentioned collagen peaks, higher in dura mater than in meningioma tissue.

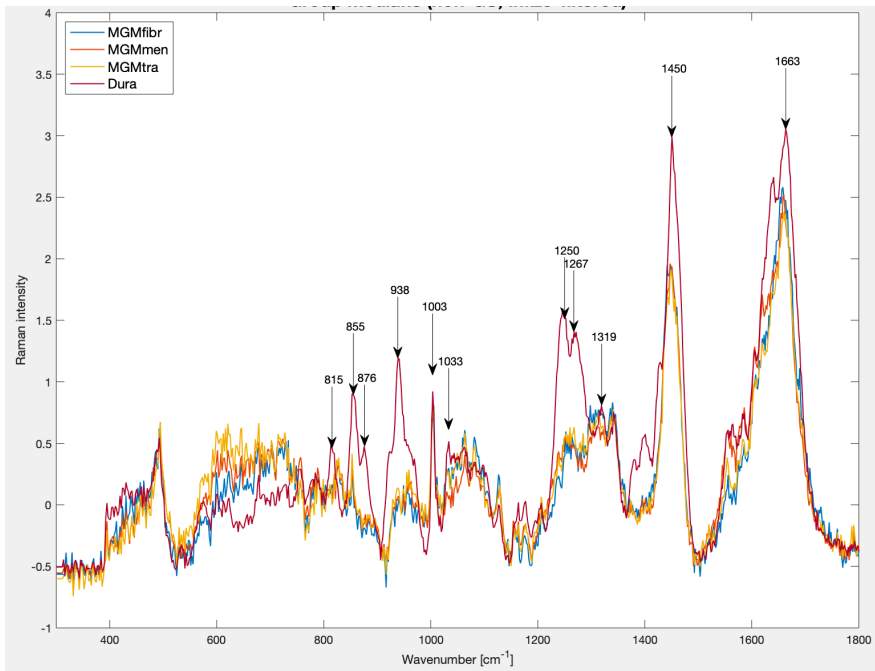


Figure31: Mean spectra of dura mater (red spectrum) and different meningioma subtypes (fibrous, meningotheelial and transitional) with annotation of the before mentioned collagen peaks. A differentiation based on the annotated collagen-peaks can be observed between the spectrum of dura mater and meningioma subtypes. X-axis corresponds to the wavenumbers (cm^{-1}) and the Y-axis corresponds to the Raman intensity. Figure source: own production. Figure produced with Solais™ and Matlab®.

We apply a TSNE (*figure32* and *figure33*) on the used meningioma and dura mater samples to see if collagen alone would still make a difference. A clear clustering between the two classes can be identified.

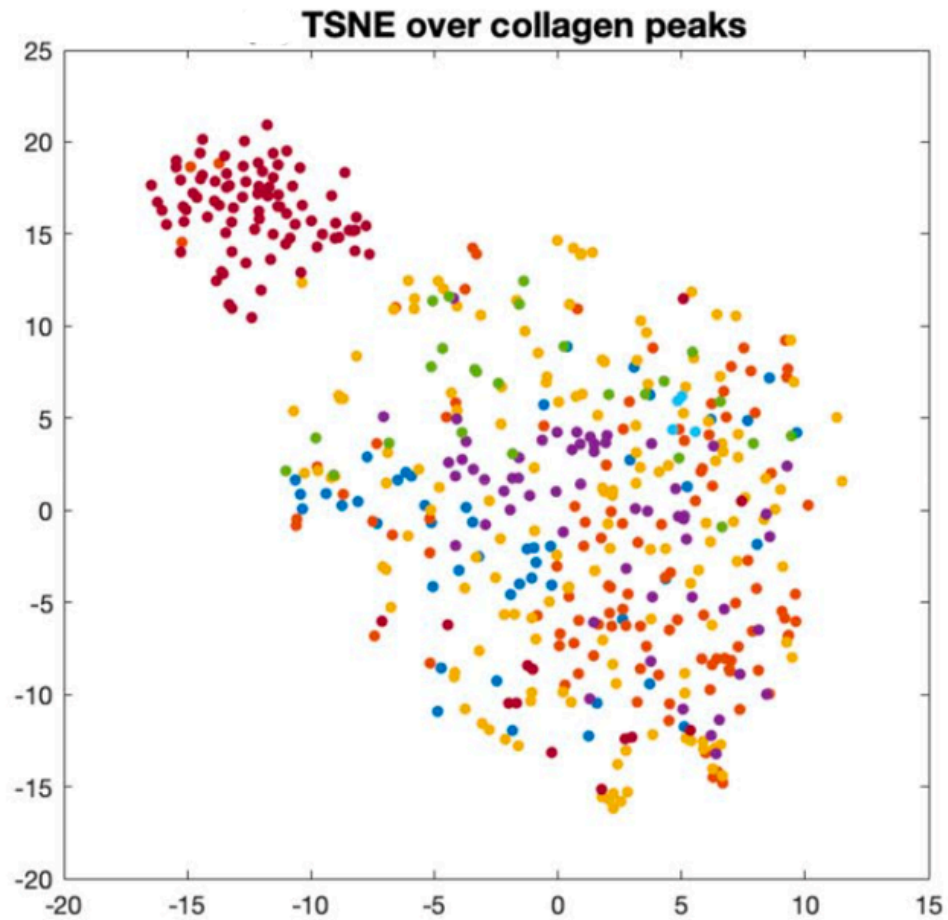


Figure32: TSNE over the collagen peak spectrum between dura mater (red dots) and meningeoma subtypes (coloured dots). Collagen peaks at 815cm^{-1} , 855cm^{-1} , 876cm^{-1} , 938cm^{-1} , 1003cm^{-1} , 1033cm^{-1} , 1250cm^{-1} , 1267cm^{-1} , 1319cm^{-1} , 1450cm^{-1} , 1663cm^{-1} . A clear cluster formation can be observed. Figure source: Jelke, Mirizzi et al. 2021; Scientific-reports 2021, "Reproduced with permission from Springer Nature" ⁷⁵

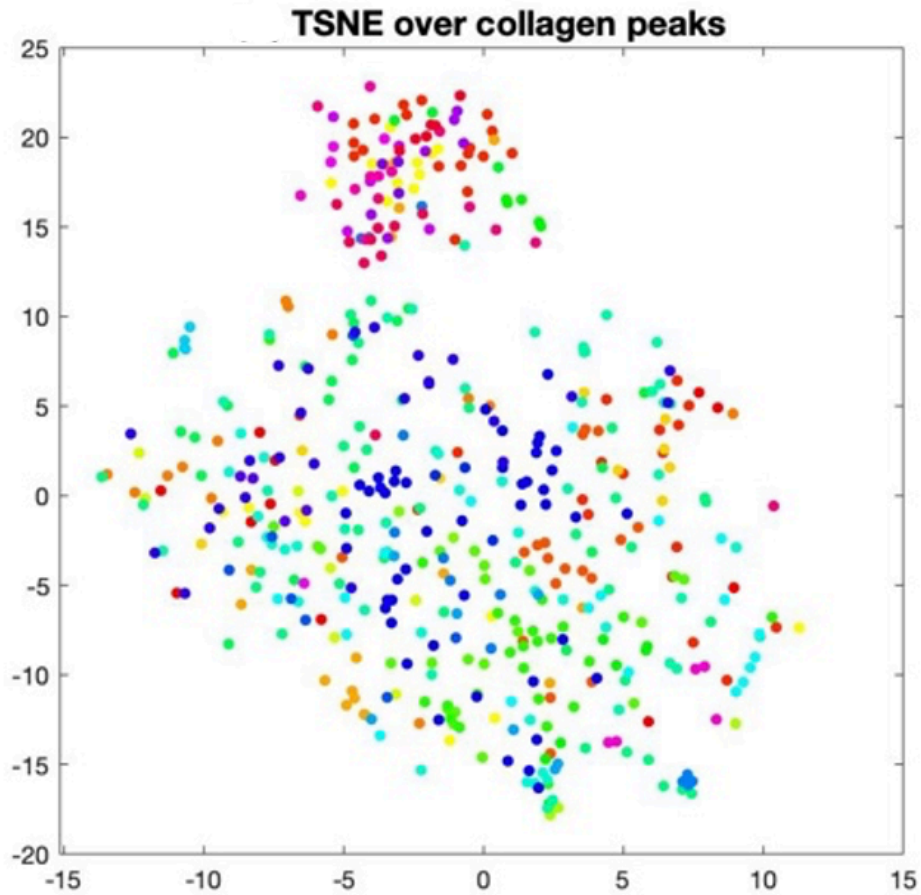


Figure33: Same TSNE as in *figure32* but patient-based to avoid any intra-patient biases. Every dot-colour represents a different patient. A clear cluster-formation can be observed. The mixture of coloured dots excludes a cluster formation by patient. Figure source: Jelke, Mirizzi et al. 2021; Scientific-reports 2021, “Reproduced with permission from Springer Nature”⁷⁵

As a last control we perform here the before mentioned collagenase-experiment (*figure34*). Again, the characteristic peaks for collagen are indicated by arrows.

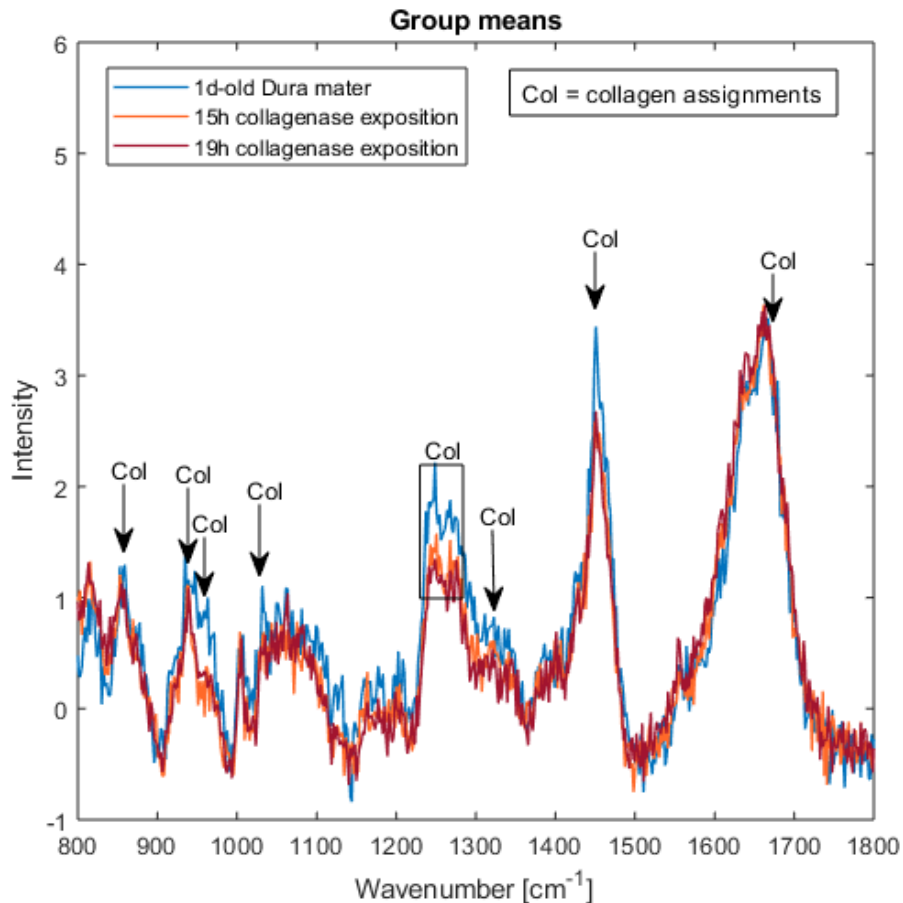


Figure34: Collagenase experiment. In blue, native spectrum of dura mater. In orange, spectrum of the dura mater after 15h of collagenase exposure. In red, spectrum of the dura mater after 19h of collagenase exposure. A diminishing of the collagen peaks can be observed with a longer exposure time towards the collagenase. X-axis corresponds to the wavenumbers (cm^{-1}) and the Y-axis corresponds to the Raman intensity. Figure source: own production. Figure produced with Solais™ and Matlab®.

We can see that the collagen peaks diminish over extending collagenase-exposure time. No total disappearance of the collagen peaks can be observed.

In a next step we perform the same analyses as for the collagen experiment but this time focusing on different lipids. Is a differentiation between meningioma and dura mater possible by different lipid contributions? In *figure35* no clear cluster formation in the TSNEs, based on different lipids, can be observed. The TSNE is at first run over the mean spectra of the included meningioma and dura mater samples and afterwards only over the general lipid peaks (over peaks of sphingomyelin, of phosphatidylethanolamine, of cholesterol and of cholesterol ester). The TSNE is based on specific peaks, characteristic for each analysed lipid subgroup. No clear cluster formation between dura mater (red dots) and meningioma (blue dots) can be observed.

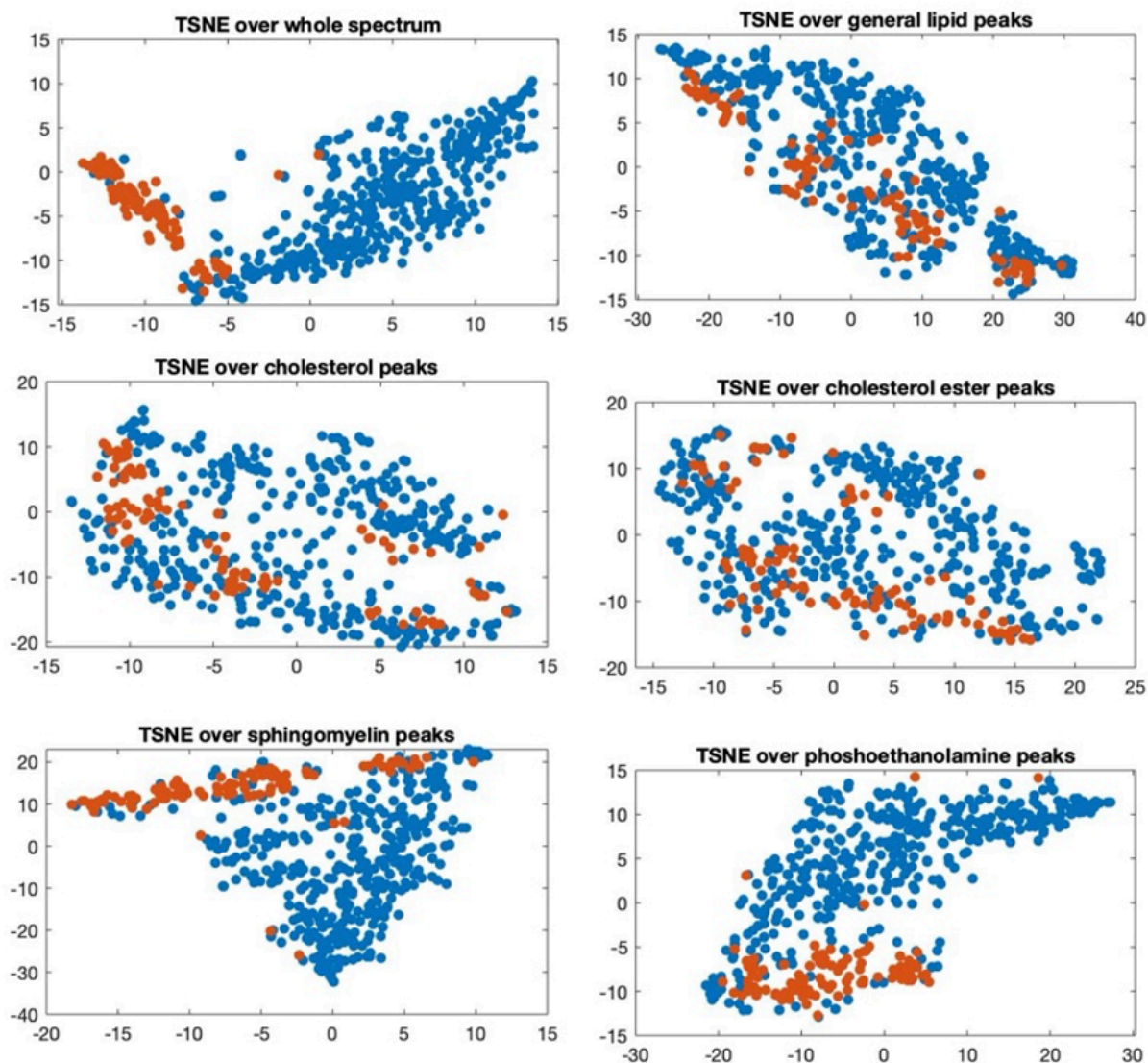


Figure35: TSNE cluster visualization with focus on the lipid peaks for differentiation of dura mater (red dots) and meningioma (blue dots). No clear cluster formation can be observed in these plots. Figure source: Jelke, Mirizzi et al. 2021; Scientific-reports 2021, "Reproduced with permission from Springer Nature" ⁷⁵

In a next step a SVM classifier is trained. A special regard is put on its verification.

As already mentioned in the material and methods section, a SVM classifier is trained and a colour map, usable as an overlay on the VLI, is designed.

We validate the classification once by using a fivefold-cross-validation and then with an external test set. With the fivefold-cross-validation we achieve a sensitivity of $96.06 \pm 0.03\%$ and a specificity of $95.44 \pm 0.02\%$. Furthermore, a good performance with the external test set can be demonstrated, 100% sensitivity and 93.97% specificity.

For classifier verification, we chose one specific sample, containing dura mater and meningioma and it is overlaid by a multitude of measuring points (*figure36*). A point-by-point verification of the classifier with a pathological verification can be achieved this way. A sensitivity of 93,0% and a specificity of 89,7% can be accomplished by the classifier, resulting in a correct identification of tumor and dura mater tissue. The overlaid heat map in (B) of *figure36* shows in yellow the 'meningioma' tissue and in blue the 'non-meningioma tissue'.

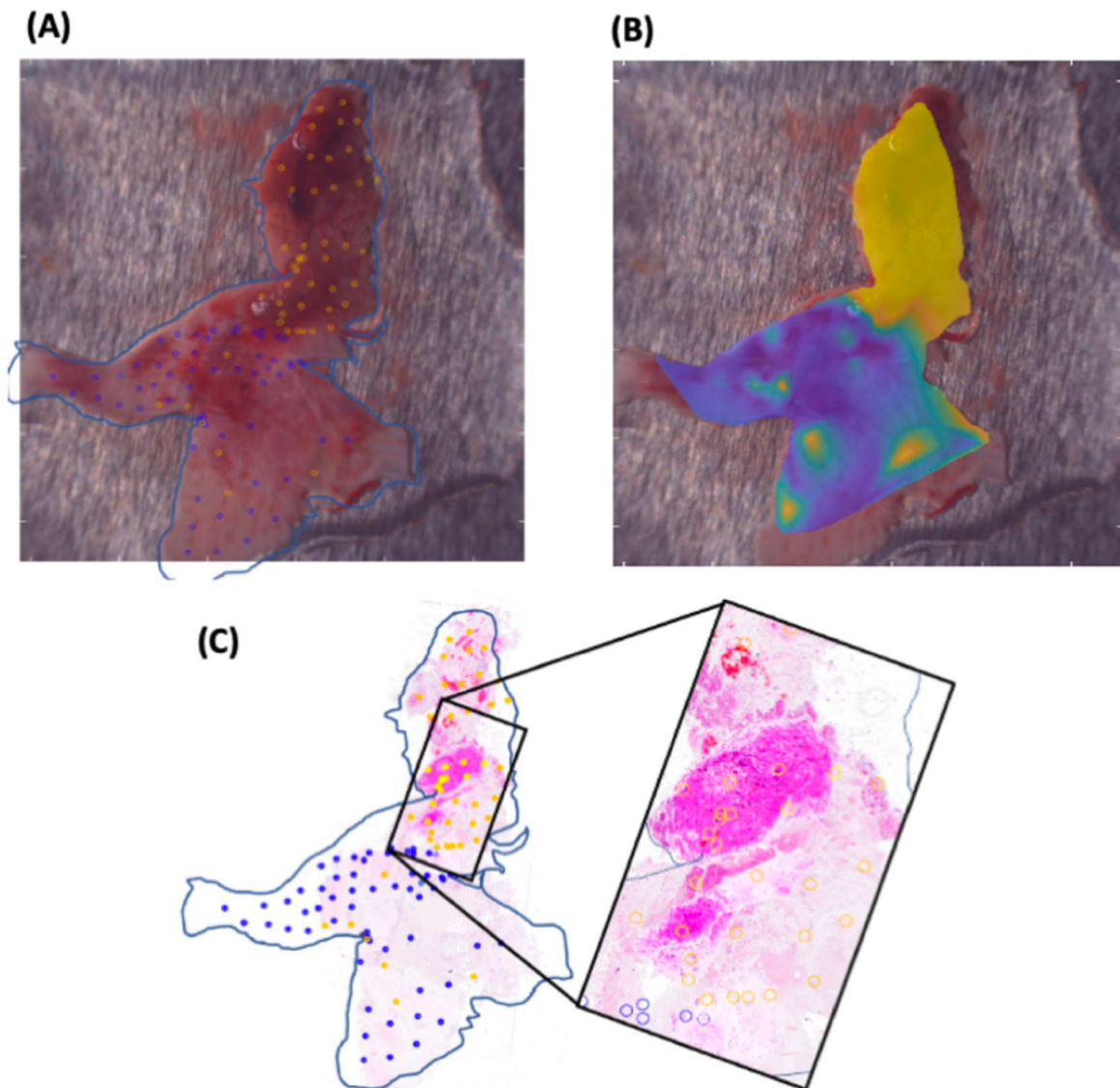


Figure36: Verification of the trained classifier. Dura mater-meningioma-classifier, verified on histological level. **(A)** VLI with the imprinted measuring points and the newly traced frame. **(B)** Classifier heat map superimposing the VLI. Blue corresponds to 'non-meningioma tissue' and yellow to 'meningioma' tissue. **(C)** Superposition of 21 H&E stained slices. The zoomed-in interval corresponds to a tumor infiltration zone. Here blue and yellow dots are mixed and on the histological verification an infiltration of malign cells was described. Figure source: Jelke, Mirizzi et al. 2021; Scientific-reports 2021, "Reproduced with permission from Springer Nature"⁷⁵

5.2.3 Publication

These results have been published on the 8th of December 2021 in “*Scientific Reports*”. The published paper is attached in the supplements (*supplement4*). Some of the here represented figures are extracted from the paper. They are indicated by : ‘Figure source: Jelke, Mirizzi et al. 2021; Scientific-reports 2021, “Reproduced with permission from Springer Nature” ⁷⁵’.

6 Outlooks

As we already demonstrated in this study, RS is a multifunctional and easy usable diagnostic tool whose potential can and should be extended to other applications than those already mentioned.

In this study the potential of RS to correctly differentiate between fixation states as well as between different tissue entities is demonstrated. This could be extended to more and more tissue groups, such as the heterogenous group of metastases originating from different origins, or to rare brain tumors like ependymomas. It would be conceivable to develop a small RS device that could be introduced directly into the microscope of the neurosurgeon, linked to neuronavigation to provide direct feedback on the underlying tissue unit during surgery. 5-aminolevulinic acid (5-ALA) is commonly used in neurosurgery for better visualization of glioblastomas by accumulating in the tumorous tissue. The augmented fluorescence can help the neurosurgeon to correctly remove the malignant tissue.¹⁰⁸ This whole costly and time consuming procedure could be minimized by the use of RS. Furthermore, 5-ALA is only accumulating in the infiltration zone of high-grade malignant gliomas. RS could be used in any grade of glioma and in the entire sample. However, the use of RS should not be limited to brain tumors, but should also be used to diagnose tumors of various origin as already started in dermatology and gynaecology. Not only the diagnosis of 'compact' tumors might be possible in the future with the use of RS, one could also think of the analysis of blood samples for a potential early tumor diagnostic.¹⁰⁹

The augmented research interest in RS opens the door for the construction of an omniclass classifier. If we would be able to analyse all different kinds of tissue samples and find specific spectral changes, it would be possible to build a complete spectral library. This library could be complete enough to easily identify all different types of tumor tissue, which would revolutionize the diagnostic field of medicine.

7 Discussion

7.1 General discussion and limitations of the study

The incidence of tumors in human beings is increasing over time.^{110,111} Whether this increase is due to better diagnostic tools, an aging population, an unhealthy lifestyle or a noxious environment is not really known. Unquestionably, there is an urge need for a quick, easy and omnipresent diagnostic tool to identify malignant cells, enabling a precise identification of the tumor and proposing the best possible therapy to the patient.

RS, which is known for being a non-destructive, rapid and easy-usable tool would be a good method to fulfilling these needs. First, this involves being able to correctly use RS, to understand the biochemistry of different tissues and their impact on the Raman spectrum. Second, we have to include a multitude of different samples, both native and fixed, and use machine learning algorithms to develop classifiers that can automatically identify the entity as well as the margins of a potentially malignant tissue collection.

By knowing the tumor entity as well as the tumor borders, a more radical tumor excision can be achieved, which would significantly reduce the risk of recurrences and consequently be associated with a better patient outcome.¹¹²

Raman spectroscopy is already widely used and described in literature. Section 2.2.4 lists different utilizations, especially non-clinical utilizations of RS. Furthermore, the review study of DePaoli et al. has to be mentioned, representing a compact overview once of RS itself and once of the already existing findings.⁶⁸ Here we focus on the use of RS in different subcategories of the medical field, more precisely in neurosurgery and neuropathology. Zhou et al. describe the possibility to distinguish ex-vivo between metastases originating from five different organs (lung, breast, kidney, rectum and orbita) with a specificity of 75% and a sensitivity of 100% using resonant Raman spectroscopy.¹¹³ Bergner et al. have developed a Raman microscopy-based method to identify metastases, necrosis and normal brain tissue on snap-frozen and then sliced tissue preparations with an accuracy of ca. 99%.¹¹⁴ A similar analysis, as well as similarly good results, are obtained by Koljenovic et al.¹¹⁵ They distinguish vital glioblastoma tissue from necrosis by building coloured maps of the cryofixed sample slices. Lakomkin et al. have analysed the possibility of using RS for a more precise 5-ALA detection in glioblastoma surgery with great results.¹¹⁶

The majority of the studies are performed ex-vivo and even on pre-processed, pathologically fixed samples by the use of Raman microscopy. Raman microscopy is more

precise than the macroscopic method because it is easy to retrace exactly the measuring point back to a precise pathological diagnose. Furthermore, the sample, fixed and prepared specially for microscopic analysis, is less susceptible to environmental influences. Since we are handling native samples directly after surgical extraction, it is important to have a closer look on these macroscopic samples and ensure that the trained classifier is robust to all external influencing factors. This technique will reduce the need for costly and time-consuming intra- and/or peri-operative imaging, like CT or MRI.¹¹⁷ Furthermore, the need for a time-delayed neuropathological sample interpretation could be minimized by using RS. It could be used whenever time or personnel are not available for rapid tissue analysis.

It is important to take a closer look at possible influencing factors. They could deform the actual spectrum and thus lead to incorrect results. The limitations of the study need to be discussed in detail to allow a better understanding of RS as well as a precise handling of the data in future studies.

First, the native samples are placed on an aluminium cup and embedded with some physiological water. Afterwards, this sample preparation is placed on a movable stage. Since the VLI is taken before the stage moves, we must expect minimal sample movement. This is due to the fact that it is not possible to fix the sample completely on the aluminium cup without destroying it, and some drops of water must be sprayed on the sample to avoid dehydration. This could provoke some measuring points to lay outside the sample. This should be considered if some spectra, mostly spectra from measuring points located near the edges of the sample, are significantly different from the other spectra of this sample. In addition, the samples extracted directly during the neurosurgical operation, are not of the same size and, more importantly, are not completely plane. The inhomogeneity of the sample surface, ups and downs, could influence the spectrum to some extent. Water drops, especially ice crystals formed during the cryofixation process could derive the spectrum onto another part of the sample or even to a measuring point outside the sample. While this is likely to be true for only a minimal portion of the spectra, it should still be considered as a possible explanation if a spectrum drops off completely. Since we want to establish an in vivo usable diagnostic tool, it is important that we learn how to deal with these inevitable incidents. As mentioned before, different parameters (6-30 averages and an acquisition time between 800ms to 2000ms for each measuring point) are used to scan the samples. The rang of parameters is due to the experimental setup of this study as well as the heterogenous sample dataset.

The longer the acquisition time is, the higher the intensity will be. In *figure37*, this phenomenon can be observed, the intensities (Y-axis) are increasing with higher acquisition time. An explanation could be that the higher number of photons scanned by the longer

acquisition time, will have a higher impact on the spectral intensity. Pelletier et al. describe that if more averages are used, the signal-to-noise ratio will be higher.¹¹⁸ In *figure38*, we were interested in reproducing these findings.

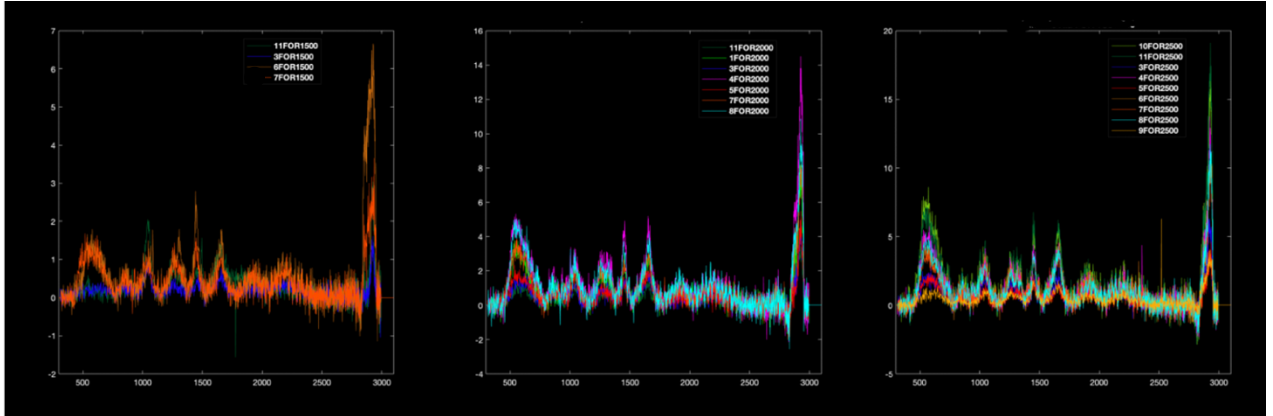


Figure37: A piece of muscle scanned firstly with an acquisition time of 1500ms (first picture), then with 2000ms (middle picture) and afterwards with 2500ms (last picture). An increase in intensities on the y-axis can be observed with longer acquisition times. Figure source: own production. Figure produced with Solais™.

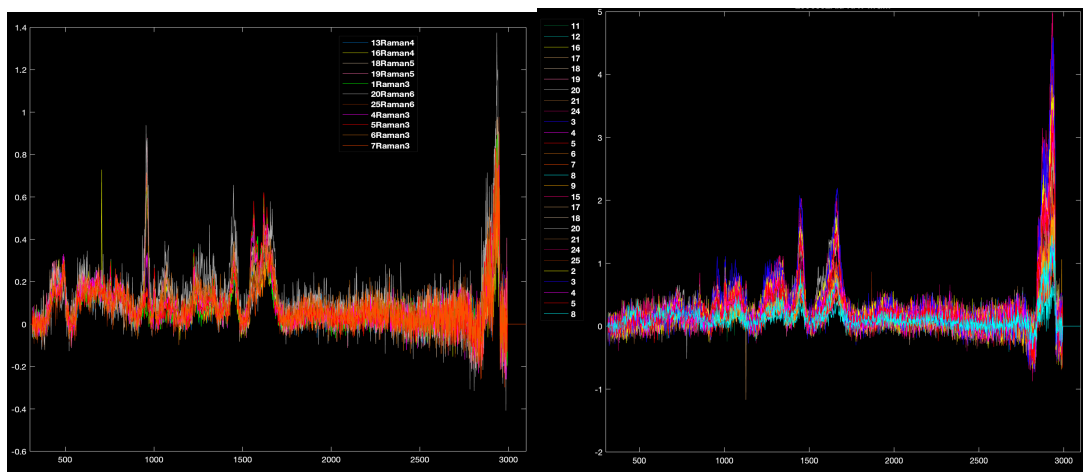


Figure38: A piece of meningioma scanned firstly with 1.0 averages (left picture), then with 1.5 (right picture). No clear or significant changes can be observed regarding the signal-to-noise-ratio when increasing the averages. Figure source: own production. Figure produced with Solais™.

In all the analyses, special attention was paid to have an equilibrated data set regarding the parameters to minimize its potential effect on the results. Furthermore, the scanning itself is, inevitably, taking some amount of time which could already induce sample decomposition. All the samples are scanned within 20 minutes after excision.

All these influencing factors could interfere with the classifier performance, but since we want to train an in-vivo classifier it is mandatory that the classifier can handle 'natural' variances. As seen in the different presented results, which all have a high sensitivity and specificity, our classifier is able to successfully deal with these variances.

As already mentioned in the text, the choice of container-material (plastic or aluminium cup) is of great importance. When performing the RS scan, it is mandatory to use an easily accessible material, such as aluminium. It has been proven that some materials, like plastic, have a great Raman spectrum that would interfere with the spectrum of the actual tissue being scanned. Not only would the tissue spectrum become nearly useless, but also if the classifier would have been trained on these plastic-interfered spectra, the performance of the classifier would be affected if used on samples which are not measured on plastic. It is important for further studies to use a correct and fitting sample background. As already mentioned, metallic aluminium with its negligent Raman spectrum would be a good choice. It has to be noticed that the oxidized form of aluminium shows a spectrum in the wavenumber region below 900cm^{-1} . This region has to be handled with care since this could have an influence in smaller samples.⁶¹ Calcium fluoride (CaF_2) has one single Raman peak at 322cm^{-1} which would make it an even better choice for the background material. Since aluminium is better available, especially in the operating room, we opted for aluminium. Calcium fluoride would, because of its translucent property, be a perfect choice for Raman microscopy.¹¹⁹

All the used methods for data pre-processing (background removal, Savitzky Golay filter, outlier sorting, removal of cosmic ray artefacts etc.) are widely used in the spectral- and Raman spectroscopic field. Without them, Raman spectra are difficult or impossible to use for comparative studies. For the future, and especially for the introduction of RS in the clinical routine, it would be essential to have a standardized pre-processing procedure usable without any deeper ML knowledge. Our data pre-processing is simple and similar to methods used in literature. It could be easily integrated into any ML-code.

We chose a SVM classifier because it is widely used in the ML field and has performed well in our analyses. But we could also have used other classifiers. We believe that the choice of classifier algorithm should not be critical for the classifier outcome. *Table3* shows that other methods would work equally well. Different classifiers produced with the Matlab® Classification Learner app are used on the meningioma and dura mater data for comparison with our own SVM classifier. The results do not change significantly, demonstrating the robustness of the trained classifier.

<i>Classifier</i>	<i>Accuracy</i>
<i>Fine Tree</i>	92.4%
<i>Medium Tree</i>	92.4%
<i>Coarse Tree</i>	93.0%
<i>Fine KNN</i>	83.6%
<i>Medium KNN</i>	83.2%
<i>Coarse KNN</i>	88.6%
<i>Cosine KNN</i>	92.6%
<i>Cubic KNN</i>	77.6%
<i>Weighted KNN</i>	80.6%
<i>Linear Discriminant</i>	95.2%
<i>Linear SVM</i>	96.4%
<i>Gaussian Naïve Bayes</i>	75.6%
<i>Kernel Naïve Bayes</i>	89.4%
<i>Narrow Neural Network</i>	97.0%
<i>Medium Neural Network</i>	97.8%
<i>Wide Neural Network</i>	97.6%
<i>Bilayered Neural Network</i>	96.6%
<i>Trilayered Neural Network</i>	95.2%

Table3: Results of different classifiers produced with the Matlab® Classification Learner app.

Nevertheless, SVM classifiers have their limitations, which should be kept in mind. SVM is known for good separation when the analysed groups (here analysed sample entities) have clear margins and good performance in high dimensional spaces. But SVM is less performant when the different classes overlap (for example in the infiltration zone). It is sometimes difficult to retrace the exact classification because SVM attributes points above

or below the hyperplane.^{76,77} In summary, SVM is a good choice distinguishing meningioma and dura mater but should be handled with caution when analysing the infiltration zone.

A TSNE can be used for non-linear data separation and is known to preserve the global data structure well. This means that data points which are close to each other in a multidimensional setting will also be plotted side by side when dimensionality reduction is performed by TSNE. However, TSNE will not reproduce exactly the same figure (the same cluster-arrangement) every time, even when performed on the same data set, a slight rotation is possible.⁷³ This has no influence on the actual result, only on the visual representation. To minimize the effect of overfitting the machine learning tool, meaning that the classifier is only usable on the specific data it was trained on, a five-fold-cross validation is performed. The trained classifier, in this case the dual-class-classifier for meningioma and dura mater, could be used as it is to analyse different meningioma and dura mater samples.

One important limiting factor of this study is the limited number of patients and the difficulty in obtaining access to healthy brain samples. We are working with native tissue samples collected during neurosurgical procedures and are therefore limited to these samples. Furthermore, because the patient should not be exposed to any additional risk at any point of the study, small samples or biopsies often cannot be introduced into the RS study. The potential risk of sample destruction or dehydration, which would urge an additional biopsy for the patient, must be considered. This would not be tolerable and will therefore be avoided. Small samples are fixed directly in a formalin solution and sent to neuropathology without Raman spectroscopic examination. This precaution also limits our access to more rare tumor entities. The same is true for healthy brain tissue: it is intolerable to remove healthy tissue without a medical reason. The only 'healthy' samples we are analysing are tissue pieces that must be removed to get to the actual tumor. This technique is also used in most previously published studies to distinguish healthy from malignant human tissue samples.^{120,121,122} One could also think of using samples from body-donors, but here the need for direct Raman scanning to avoid any post-mortem biochemical sample alterations is a limiting factor.

When analysing the Raman spectrum, the different wavenumber regions must be considered, as described before. In literature, the used wavenumber regions vary widely. Kalkanis et al. and Wills et al. use a spectral range that tends to be in the lower variety (600cm^{-1} - 1800cm^{-1}).^{122,123} The high-wavenumber region is also often used because it is less influenced by background noise and contains sufficient information for successful sample

differentiation.^{124,91} Ultimately, it is important to understand and consider the advantages respectively the disadvantages of each region, and depending on the main goal of the study, the spectral range has to be adjusted. To minimize any 'deformation', the whole or at least a major part of the spectrum should be considered.

Jermyn et al. already describe the design of a "*handheld contact Raman spectroscopy probe technique for live, local detection of cancer cells in the human brain*".¹²⁵ They claim a differentiation of healthy brain tissue and cancer tissue with a sensitivity of 93% and a specificity of 91% by using their RS device. They focus on the identification of glioblastoma cells. The device provides immediate intraoperative feedback about the underlying tissue by projecting the Raman spectrum onto a nearby computer. Furthermore, they describe the differentiation between healthy brain and tumor tissue by different lipid bands for cancer cells (700cm^{-1} and 1142cm^{-1}), higher bands from 1540cm^{-1} to 1645cm^{-1} , a higher number of nucleic acids for malignant tissue. Machine learning is performed with a boosted trees method. They found a very good way to include RS into the neurosurgical workflow. Desroches et al. found similar results by also using a hand-held probe to differentiate normal brain tissue and glioblastoma (specificity of 89%; sensitivity of 84%).¹²⁶ In another study, Jermyn et al. are interested in the possibility to detect malignant cells that penetrated deeper into the healthy brain tissue than imaging (MRI) would suggest by using their designed handheld RS probe.¹²⁷ They perform multiple in-vivo RS measurements in the resection cavity, track the location of the measurement using infrared signals from the probe back to pre-operative imaging, and take biopsies from the measurement locations. Afterwards, the biopsies are analysed by a neuropathologist. According to all these results, a retracement of the fugitive malignant cells can be achieved with an accuracy between 3,7cm and 2,4cm beyond the imaging margins.

In the future, we would want to incorporate a Raman spectroscope directly into the surgical microscope, which would allow an even more precise tissue analysis without switching between the microscope and the handheld probe. Furthermore, it would be of great benefit to create a coloured heat map that could also be integrated into the surgical microscope, giving the neurosurgeon easy feedback on the underlying tissue composition. We would also like to extend the tumor classification beyond glioblastomas towards an omniclass-classifier. An omniclass-classifier could omit the need to take biopsies and provide direct and precise diagnosis of the sample directly intraoperatively. Please note here that these are still experimental setups and further studies on this topic have to be done.

7.2 Fixation study

In order to increase the number of samples, the amount of possible data, and to improve machine learning as well as the understanding of RS, it is important to recur to already existing tumor-banks. Since these samples are fixed chemically by formalin or physically by cryopreservation (often dry-ice), the specific changes in the Raman spectrum of certain samples are investigated in this study. Yu et al. describe the importance of tumor-banks preserving and the need for correct sample storage, especially the maintenance of constant, very low temperatures.⁴⁶ The quality of this procedure needs to be verified by a pathologist, analysing for example the amount of tumor cells in the stored sample and comparing it to the amount of the beginning. Estrada et al. have done a similar work on long-term-storage of monkey brain samples stored at -80 degree Celsius in a 15% glycerol solution.¹²⁸ After defreezing the samples for analysis, they demonstrate a strong stability of sample quality over time. RS would be an easier, quicker and most importantly, non-destructive way to resolve this task. It might be possible to analyse samples without thawing them. Biochemical changes induced by cryofixation and/or formalin-fixation have already widely been discussed in literature. Thavarajah et al. and Jones et al. describe detailed reactions induced by formalin-fixation on the biochemical composition of a sample.^{42,129} Several authors and study groups already have had precise insight not only into the quality of long-stored samples and the biochemical changes induced by dry-ice and formalin-fixation, but also into the potential of RS as a helpful tool in these domains. Here we combine these two ideas, first the identification of biochemical changes induced by dry-ice and formalin-fixation and second the potential of recurring to tumor-banks to improve the samples available for RS analysis.

No significant difference is observed in the spectral analyses between the native and frozen samples. Cryopreservation does not lead to major biochemical changes within the tissue composition, which is in line with the before described literatures claiming good sample quality even after long-term cryopreservation. When our previously trained dualclass-classifier (trained on native meningioma and dura mater samples) is applied on cryofixed data, a sensitivity of 100% and a specificity of 75% can be observed.

To summarize these results, cryofixation does not cause major changes in the biochemistry of the sample, which allows to analyse cryofixed samples with a natively trained classifier. This opens the door for the non-destructive use of RS to analyse tumor-banks. Furthermore, an already trained classifier could easily be used to retrospectively explore the tissue entity of stored samples. No need for a special training of a cryofixed classifier. Similar results have been found by Wills et al. who investigated whether inclusion of thawed samples,

more precisely neuropediatric tumors, would be possible to increase RS data.¹²³ They found that Raman microscopy can recognize the correct tissue entity in a cryopreserved section. These results suggest that RS is able to correctly identify a sample entity even when the sample has been cryopreserved and that the biochemical changes induced by dry-ice are not so pronounced that they would change the overall spectral appearance of the sample. The potential formation of ice-crystals mentioned previously was discussed by Kalkanis et al.⁵¹ They found a diminished accuracy of 77,5% in frozen H&E stained sections by Raman microscopy when the samples contain these freezing artefacts, as opposed to an accuracy of 97,8% when there are no ice-crystals in the sample. Nevertheless, both accuracies are still good and satisfying. These results can be relocated in our findings. First, at a spectral level, where no significant differences can be found between native and cryofixed samples, meaning that cryofixation does not have a strong effect on the biochemistry of the sample. And second, through our natively trained classifier, which can still recognize the tissue origin even in a cryofixed sample. The ice-peaks described in literature are mostly located in the wavenumber region above 3000cm^{-1} while our wavenumber-scale only ranges from 314cm^{-1} to 2994cm^{-1} . Some important data induced by cryofixation may thus be overlooked. But since these Raman bands are mainly OH-stretching, this should not influence to great extend our results since we are focusing on the intra-tissue induced modifications. Furthermore, the low wavenumber region, between 10cm^{-1} and 400cm^{-1} , representing mostly very heavy atoms, could be of great interest for the analysis of ice crystals. But as mentioned above, this region was omitted from the analyses because of the interference of aluminium.

However, formalin-fixation induces new or altered peaks specific for the different entities. Formalin-fixation infiltrates the sample. When the previously trained dualclass-classifier is applied on formalin-fixed data, a deterioration of the results can be observed (specificity of 41,9% and sensitivity of 100%). In a next step, we are interested whether a simple subtraction of the pure-formalin spectrum would improve the classifier results of the formalin-fixed data. We were able to obtain a slight improvement (specificity of 62,8% and sensitivity of 100%). Special training of a new classifier based only on these difference-spectra improved the results even further (specificity of 66,7% and sensitivity of 100%). Formalin-fixation induces further changes and has to be handled with caution. As mentioned before, literature already suggests that formalin-fixation in itself is introducing major alterations in the biochemical structure of a sample, which is consistent with our results. It is not possible to use a natively trained classifier on formalin-fixed data. In future studies, a special classifier for formalin-fixation should be developed. We performed first steps in this direction by improving our results by subtracting the pure formalin spectrum

from the spectrum of formalin-fixed data. The formalin data are stored for different time laps in the formalin solution, which could have an influence on peak differentiation.

Due to the limited number of samples and/or measuring points in this part of the study, further experiments should be done by including more samples and more tumor entities. This could lower the discrepancy and strengthen our results. Nevertheless, this study gives a first and important insight into the potential of RS in handling fixed data. In summary, we demonstrated here the possibility to include tumor-banks (cryofixed samples) into the RS analyses, which would allow a quick increase in the number of samples. This would be a perfect source to improve ML and include rare tumors. In addition, RS could complement the work of the neuropathologist, particularly when working with cryofixed samples.

7.3 Meningioma study

Tumor recurrences after surgical tissue removal are common and are associated with bad survival outcome. The recurrence rate is directly related to the left-over malignant cells at primary surgical tumor removal (Simpson grading). Therefore, there is an urgent need for a powerful and easy-usable diagnostic tool directly inside of the operating room to differentiate between tumor and non-tumor tissue, which would allow a more complete tumor resection and thus reduce the risk of tumor recurrence. RS could compete commonly used intraoperative resection control tools like intraoperative ultrasound, MRI or intraoperative smear preparations because of its quick and precise use.^{130,131,132,133} All these techniques are expensive, time consuming, and must be performed by trained staff. We start this study by analysing meningioma and dura mater because they are relatively common (important for adequate data collection) and good accessibility during surgery. This topic has been previously addressed in literature by several study groups. Krafft et al. analysed glioma, meningioma and schwannoma samples using Raman microscopy.¹³⁴ They do the analysis once with RS and once with infrared spectroscopy. They create so-called Raman-maps on which they can successfully identify, beyond others, the meningioma tissue based on different shades of grey. Furthermore, they identify and use the differences in lipid and collagen composition to distinguish meningioma and dura mater as a comparative tool. A sensitivity of 90,9% and a specificity of 100% for discrimination between malignant and healthy meningeal tissue is claimed by Zhou et al. by looking at the different Raman bands as well as by using a SVM classifier.¹³⁵ Similar results are also provided by Aguiar et al. who have looked more closely at the biochemistry of meningeal tumor composition.¹³⁶ One particular study has to be mentioned here, the study of Koljenovic et al.¹⁰³ They address the problem of tumor recurrence by residual malignant meningioma cells with the aim of introducing RS into the neurosurgical routine. They find a main difference between meningioma and dura mater by the content of collagen. With the design of coloured Raman maps on cryofixed sections, they are able to differentiate meningioma and dura mater with an accuracy of 100%. All these studies already demonstrate the great potential of RS for successful differentiation of meningioma and dura mater. It should be noted that in all these examples, the samples were cryopreserved and/or fixed by a different method, no native tissue pieces were used. We are interested in the native samples that are collected directly during neurosurgical resection and are not treated with any other substances. This makes them more heterogeneous, but better reflects the reality one would have if RS would directly be installed in the microscope of the neurosurgeon.

In a first step, we focused on the spectral differences. Meningioma and dura mater are well separable, but the differentiation between the meningioma subtypes seems to be more difficult. The same results are reproduced by applying a TSNE to these data. A special patient-based TSNE excludes any intra-patient biases. Once successful differentiation is observed, we move on to the next step. The different biochemical composition of the two sample entities and the possibility to differentiate them based on biochemical Raman peaks is analysed. According to the before mentioned literature and the here included *table4*, we start with collagen. At a spectral level, the collagen specific peaks are more prominent in dura mater than in meningioma. A TSNE based only on collagen peaks confirms these results.

	Peaks (cm ⁻¹)	Assignments	Literature
Collagen	855	(Hydroxy-) Proline	Huang et al. 2003 ¹³⁷
Collagen	876	(Hydroxy-) proline P	Huang et al. 2003 ¹³⁷ Frank et al. 1995 ¹²¹
Collagen	938	(Hydroxy-) Proline	Cheng et al. 2005 ¹³⁸
Collagen	1003	Phenylalanine	Chan et al. 2006 ¹³⁹
Collagen	1033	Phenylalanine	Chan et al. 2006 ¹³⁹
Collagen	1245	Amide III	Shetty et al. 2006 ¹⁴⁰
Collagen	1250	Amide III	Cheng et al. 2005 ¹³⁸
Collagen	1267	Amide III	Malini et al. 2006 ¹⁴¹
Collagen	1271	Amide III band in proteins	Sigurdsson et al. 2004 ¹⁴²
Collagen	1319	CH ₂ CH ₃ deformation	Frank et al. 1995 ¹²¹
Collagen	1447	CH ₂ bending mode of proteins & lipids	Faolain et al. 2005 ⁴⁴
Collagen	1450	CH ₂ CH ₃ deformation	Shafer-Peltier et al. 2002 ¹⁴³
Collagen	1637	Amid I	Faolain et al. 2005 ⁴⁴
Collagen	1661	Amide I band	Naumann et al. 1998 ¹⁴⁴
Collagen	1663	Proteins, collagen type I	Binoy et al. 2004 ¹⁴⁵
Collagen	2940	C-H vibrations in lipids & proteins	Sigurdsson et al. 2004 ¹⁴²

Table4: Main collagen peaks with the biochemical background as well as the literature source where the information is extracted from. Table source: Jelke, Mirizzi et al. 2021; Scientific-reports 2021, “Reproduced with permission from Springer Nature” ⁷⁵

At a last verification of the results, we apply a collagenase solution to a piece of dura mater. A diminishing of the specific collagen peaks can be observed. The collagenase experiment is only a supplementary verification of our collagen-hypotheses using a single sample. Votteler et al. also performed a collagenase experiment by exposing leaflets of porcine aortic valves, which are mostly composed of collagen, to a collagenase.¹⁴⁶ They found similar results, an overall decrease but no complete disappearance of the collagen peaks

over the exposure time. A longer exposure time to the collagenase could eventually lead to total disappearance of these peaks.

Afterwards, the differentiation of meningioma and dura mater based on lipid content is considered in more detail. A differentiation between meningioma and dura mater can be achieved, but again no clear clustering in the TSNE for the meningioma subtypes. Aguiar et al. claim that the lipid content is higher in tumours tissue than in healthy dura mater.¹⁴⁷ These results can be reproduced to some extent by our findings, but the discrimination is of poorer nature than when based on collagen. When it comes to the meningioma subtypes, further studies have to be done. In clinical practice, the knowledge of the exact subtype is not crucial since it would not affect the surgical removal procedure. The potential differentiation of dura mater and meningioma by their different collagen and lipid contribution is of great importance.

The applied SVM classifier shows successful results in differentiating the two sample entities: a sensitivity of $96.06 \pm 0.03\%$ and a specificity of $95.44 \pm 0.02\%$ for an internal fivefold cross validation and a sensitivity of 100% and a specificity of 93.97% if validated with an external test set. This demonstrates that the trained classifier is able to handle heterogeneous native tissue samples, which is essential for direct use in the surgical field. It provides direct feedback without the need for pathological sample preparation and a specialist in neuropathology. The classifier results are consistent with the before mentioned literature results.

A last verification of our results is performed by taking one sample containing dura mater and meningioma and scanning it in detail using multiple measuring points. This sample is afterwards precisely analysed by a specialist in neuropathology so that we can review each measuring point for its histological description. The trained classifier and a heat map are overlaid on the sample, differentiating dura mater and meningioma with a sensitivity of 93,0% and a specificity of 89,7%. These results show that our classifier is robust even at a precise histological verification level. The here designed heat map would be a great visualization tool, a simple product design, for later introduction of RS within the surgical microscope. The main question for the neurosurgeon is the exact identification of the infiltration zone. In our 'special sample' we are already able to successfully distinguish the tumorous cell clusters that are spreading in the healthy meningeal tissue. For a more precise insight, the number of measuring points as well as their proximity has to be increased. Since the neurosurgeon is equipped with neuronavigation, a microscope and, of course, his/her own experience and optical interpretation, he or she can decide where the potential infiltration zone is proximately and lay more measuring points on this precise area. In summary, RS would be a helpful non-destructive diagnostic tool to correctly identify

meningioma tissue intraoperatively, even in the infiltration zone. These findings could significantly reduce the risk of tumor recurrences.

8 Conclusion

We have demonstrated that RS is a strong, quick and easy usable new diagnostic tool that has the potential to revolutionize the diagnostic field of medicine.

We present here a successful identification of fixed samples by a constant Raman spectrum for cryofixation and the appearance of new, sample-specific peaks for formalin-fixation. As seen in the result section, no significant statistical difference can be observed between native and cryofixed data. Furthermore, we demonstrate that it is possible to use a natively trained classifier on cryofixed data. As a conclusion, on the one hand, it is not necessary to train a special classifier on cryofixed data since we can use the natively trained one. On the other hand, formalin-fixation is inducing specific peaks that are different for each analysed sample entity. This underlines the hypothesis that formalin induces specific biochemical changes in each specific sample/molecule. By subtracting the pure formalin spectrum from the mean spectrum of formalin-fixed data, we can ameliorate the classifier performance. Since the results are not as good as the cryofixed data, it is important to notice that this provides a quick overview of the underlying sample entity, but it is still mandatory to finalize the sample differentiation with further analyses.

A profound knowledge of the biochemical changes introduced by different fixation methods, in this case, cryofixation and formalin-fixation, will allow the use of already existing tumor-banks. This would rapidly increase the number of scannable tissue samples, and also augment the number of rare tumor probes, allowing for a strong improvement in machine learning. This could open the door for an omniclass-classifier. This classifier could be applied not only to native but also to fixed data. This would be a helpful tool to complement the work of the neuropathologist, which requires a high level of expertise as well as specialised tools. This could make RS a ubiquitously usable diagnostic tool that complements the work of the neuropathologist and can be used in an omnipresent environment where time-consuming and costly analyses are not wished or technically not feasible.

Furthermore, the successful differentiation between dura mater and meningioma is shown. These are fundamental results for a better understanding of the functioning of RS, the required background analyses and the handling of the specific spectra.

Tumor recurrences are often caused by residual malignant cells left over from the initial surgery, as it is nearly impossible to remove all tumour cells without the risk of removing healthy brain tissue as well. RS would provide the opportunity to obtain immediate, instantaneous feedback on the tissue entity of the underlying cell formation. Consequently,

RS could help the neurosurgeon with the fundamental question of whether or not to remove this tissue. RS, as a new and sophisticated tool, that does not require preanalytical sample processing, could easily fulfil these needs. It has the potential to be introduced into the daily neurosurgical routine, minimizing the risk of recurrences, the need for biopsies and time-consuming neuropathological sample preparations. Of course, we are still in the beginning of understanding and exploring the vast potential of RS. To assure optimal patient care, RS should still be reviewed and accompanied by the trained eye of a neuropathologist and postoperative imaging (CT or MRI) to verify Simpson grade I resection at the beginning of its introduction into routine clinical practice. Afterwards, these precautions could be easily omitted. The colour overlay heat map designed based on the SVM classifier results could be integrated into the neurosurgeon's microscope in the near future.

In summary, we present here a rapid, easy usable and accurate spectroscopic device for insitu sample diagnostic. Furthermore, the newly obtained results on the fundamental biochemical differences between tissues types as well as between fixation methods are explored. The potential of RS remains to be analysed in further studies, but already shows its enriching contribution to simpler and non-destructive tissue handling. This study shows the great potential of RS to be introduced into the clinical routine of the operating room in the coming years.

9 Conflict of interest

The authors declare that they have no conflicts of interest.

10 References

1. Scheithauer BW. Development of the WHO classification of tumors of the central nervous system: A historical perspective. *Brain Pathol.* 2009;19(4):551-564. doi:10.1111/j.1750-3639.2008.00192.x
2. Louis DN, Ohgaki H, Wiestler OD, Cavenee WK, eds. *WHO Classification of Tumours of the Central Nervous System*. Revised 4th. Lyon: International Agency for Research on Cancer; 2016.
3. Louis DN, Perry A, Wesseling P, et al. The 2021 WHO classification of tumors of the central nervous system: A summary. *Neuro Oncol.* 2021;23(8):1231-1251. doi:10.1093/neuonc/noab106
4. Claus EB, Calvocoressi L, Bondy ML, Wrensch M, Wiemels JL, Schildkraut JM. Exogenous hormone use, reproductive factors, and risk of intracranial meningioma in females. *J Neurosurg.* 2013;118(3):649-656. doi:10.3171/2012.9.JNS12811
5. Menger R, Connor Jr. DE, Chan AY, Jain G, Nanda A. Degree of Resection and Ki-67 Labeling Index for Recurring Meningiomas. *Cureus.* 2017;9(11):9-14. doi:10.7759/cureus.1820
6. Bruna J, Brell M, Ferrer I, Gimenez-Bonafe P, Tortosa A. Ki-67 proliferative index predicts clinical outcome in patients with atypical or anaplastic meningioma. *Neuropathology.* 2007;27(2):114-120. doi:10.1111/j.1440-1789.2007.00750.x
7. Whittle IR, Smith C, Navoo P, Collie D. Meningiomas. *Lancet.* 2004;363(9420):1535-1543.
8. Marosi C, Hassler M, Roessler K, et al. Meningioma. *Crit Rev Hematol.* 2008;67:153-171. doi:10.1016/j.critrevonc.2008.01.010
9. Komotar RJ, Otten ML, Moise G, Connolly ES. Radiotherapy plus concomitant and adjuvant temozolomide for glioblastoma—A critical review. *Clin Med Oncol.* 2008;2:421-422. doi:10.4137/cmo.s390
10. Kostaras X, Cusano F, Kline GA, Roa W, Easaw J. Use of dexamethasone

- in patients with high-grade glioma: A clinical practice guideline. *Curr Oncol.* 2014;21(3):493-503. doi:10.3747/co.21.1769
11. Adegboyega G, Kanmounye US, Petrinic T, et al. Global Landscape of Glioblastoma Multiforme Management in the Stupp Protocol Era: Systematic Review Protocol. *Int J Surg Protoc.* 2021;25(1):108. doi:10.29337/ijsp.148
 12. Warren KT, Liu L, Liu Y, Milano MT, Walter KA. The impact of timing of concurrent chemoradiation in patients with high-grade glioma in the era of the stupp protocol. *Front Oncol.* 2019;9(MAR):1-9. doi:10.3389/fonc.2019.00186
 13. Stathis A. Treatment overview. *Handb Lymphoma.* 2016;20(5):33-44. doi:10.1007/978-3-319-08467-1_5
 14. Stummer W, Pichlmeier U, Meinel T, Wiestler OD, Zanella F, Reulen HJ. Fluorescence-guided surgery with 5-aminolevulinic acid for resection of malignant glioma: a randomised controlled multicentre phase III trial. *Lancet Oncol.* 2006;7(5):392-401. doi:10.1016/S1470-2045(06)70665-9
 15. Wong ET, Lok E, Swanson KD. An Evidence-Based Review of Alternating Electric Fields Therapy for Malignant Gliomas. *Curr Treat Options Oncol.* 2015;16(8). doi:10.1007/s11864-015-0353-5
 16. Kinzel A, Ambrogi M, Varshaver M, Kirson ED. Tumor Treating Fields for Glioblastoma Treatment: Patient Satisfaction and Compliance With the Second-Generation Optune® System. *Clin Med Insights Oncol.* 2019;13:0-6. doi:10.1177/1179554918825449
 17. Kerbauy MN, Moraes FY, Lok BH, et al. Challenges and opportunities in primary CNS lymphoma: A systematic review. *Radiother Oncol.* 2017;122(3):352-361. doi:10.1016/j.radonc.2016.12.033
 18. Han CH, Batchelor TT. Diagnosis and management of primary central nervous system lymphoma. *Cancer.* 2017;123(22):4314-4324. doi:10.1002/cncr.30965
 19. Coleman RE, Eccles SA. General Mechanisms of Metastasis. *Textb Bone Metastases.* 2006:1-25. doi:10.1002/0470011610.ch1
 20. Alizadeh AM, Shiri S, Farsinejad S. *Metastasis Review: From Bench to Bedside.* Vol 35.; 2014. doi:10.1007/s13277-014-2421-z
 21. Aragon-Ching JB, Zujewski JA. CNS metastasis: An old problem in a new guise. *Clin Cancer Res.* 2007;13(6):1644-1647. doi:10.1158/1078-

0432.CCR-07-0096

22. Fink K, Fink J. Imaging of brain metastases. *Surg Neurol Int.* 2013;4(SUPPL4):209-219. doi:10.4103/2152-7806.111298
23. Hicks DG, Short SM, Prescott NL, et al. Breast cancers with brain metastases are more likely to be estrogen receptor negative, express the basal cytokeratin CK5/6, and overexpress HER2 or EGFR. *Am J Surg Pathol.* 2006;30(9):1097-1104. doi:10.1097/01.pas.0000213306.05811.b9
24. Evans AJ, James JJ, Cornford EJ, et al. Brain metastases from breast cancer: Identification of a high-risk group. *Clin Oncol.* 2004;16(5):345-349. doi:10.1016/j.clon.2004.03.012
25. Gril B, Evans L, Palmieri D, Steeg PS. Translational research in brain metastasis is identifying molecular pathways that may lead to the development of new therapeutic strategies. *Eur J Cancer.* 2010;46(7):1204-1210. doi:10.1016/j.ejca.2010.02.033
26. Raman C V. A new radiation. *Proc Indian Acad Sci - Sect A.* 1953;37(3):333-341. doi:10.1007/BF03052651
27. Krishnan RS, Shankar RK. Raman effect: History of the discovery. *J Raman Spectrosc.* 1981;10(1):1-8. doi:10.1002/jrs.1250100103
28. Bumbrah GS, Sharma RM. Raman spectroscopy – Basic principle, instrumentation and selected applications for the characterization of drugs of abuse. *Egypt J Forensic Sci.* 2016;6(3):209-215. doi:10.1016/j.ejfs.2015.06.001
29. Zhang Y, Hong H, Weibo C. Imaging with Raman spectroscopy. *Curr Pharm Biotechnol.* 2010;11(6):654-661.
30. Ferraro JR, Nakamoto K, Brown CW. *Introductory Raman Spectroscopy: Second Edition.*; 2003. doi:10.1016/B978-0-12-254105-6.X5000-8
31. Jones RR, Hooper DC, Zhang L, Wolverson D, Valev VK. Raman Techniques: Fundamentals and Frontiers. *Nanoscale Res Lett.* 2019;14(1). doi:10.1186/s11671-019-3039-2
32. Banaei N, Foley A, Houghton JM, Sun Y, Kim B. Multiplex detection of pancreatic cancer biomarkers using a SERS-based immunoassay. *Nanotechnology.* 2017;28(45). doi:10.1088/1361-6528/aa8e8c
33. Ταραντίλης ΠΑ. Φασματοσκοπία Raman (Raman Spectroscopy) Φασματοσκοπία Raman (Raman Spectroscopy). 1988;14:3-4.

34. Krafft C, Schie IW, Meyer T, Schmitt M, Popp J. Developments in spontaneous and coherent Raman scattering microscopic imaging for biomedical applications. *Chem Soc Rev.* 2016;45(7):1819-1849. doi:10.1039/c5cs00564g
35. Zhao J, Lui H, Mclean D, et al. Real-Time Raman Spectroscopy for Noninvasive Skin Cancer Detection -- Preliminary Results. 2008:3107-3109.
36. Lyng FM, Traynor D, Ramos IRM, Bonnier F, Byrne HJ. Raman spectroscopy for screening and diagnosis of cervical cancer. *Anal Bioanal Chem.* 2015;407(27):8279-8289. doi:10.1007/s00216-015-8946-1
37. Huang Z, Teh SK, Zheng W, et al. Integrated Raman spectroscopy and trimodal wide-field imaging techniques for real-time in vivo tissue Raman measurements at endoscopy. *Opt Lett.* 2009;34(6):758. doi:10.1364/ol.34.000758
38. Doty KC, Lednev IK. Raman spectroscopy for forensic purposes: Recent applications for serology and gunshot residue analysis. *TrAC - Trends Anal Chem.* 2018;103:215-222. doi:10.1016/j.trac.2017.12.003
39. André S, Cristau L Saint, Gaillard S, Devos O, Calvosa É, Duponchel L. In-line and real-time prediction of recombinant antibody titer by in situ Raman spectroscopy. *Anal Chim Acta.* 2015;892:148-152. doi:10.1016/j.aca.2015.08.050
40. Cho Y, Song SW, Sung J, Jeong YS, Park CR, Kim HM. Hyperspectral depth-profiling with deep Raman spectroscopy for detecting chemicals in building materials. *Analyst.* 2017;142(19):3613-3619. doi:10.1039/c7an00894e
41. Kilmer PD. Review Article: Review Article. *Journalism.* 2010;11(3):369-373. doi:10.1177/1461444810365020
42. Thavarajah R, Mudimbaimannar VK, Elizabeth J, Rao UK, Ranganathan K. Chemical and physical basics of routine formaldehyde fixation. *J Oral Maxillofac Pathol.* 2012;16(3):400-405. doi:10.4103/0973-029X.102496 PM - 23248474 M4 - Citavi
43. Metz B, Kersten GFA, Hoogerhout P, et al. Identification of formaldehyde-induced modifications in proteins. *J Biol Chem.* 2004;279(8):6235-6243. doi:10.1074/jbc.M310752200 T4 - Reactions with model peptides PM - 14638685 M4 - Citavi

44. Ó Faoláin E, Hunter MB, Byrne JM, et al. A study examining the effects of tissue processing on human tissue sections using vibrational spectroscopy. *Vib Spectrosc.* 2005;38(1-2):121-127. doi:10.1016/j.vibspec.2005.02.013
45. Lyng F, Gazi E, Gardner P. Preparation of tissues and cells for infrared and Raman spectroscopy and imaging. *RSC Anal Spectrosc Ser.* 2011;01(11):147-191.
46. Yu Y-Y. Significance of biological resource collection and tumor tissue bank creation. *World J Gastrointest Oncol.* 2010;2(1):5. doi:10.4251/wjgo.v2.i1.5
47. Ahmed I, Agarwal S, Ilchyshyn A. Liquid nitrogen cryotherapy of common warts : cryo-spray vs . cotton wool bud.
48. Careche M, Li-Chan ECY. Structural changes in cod myosin after modification with formaldehyde or frozen storage. *J Food Sci.* 1997;62(4):717-723. doi:10.1111/j.1365-2621.1997.tb15443.x
49. Agarwal A. Semen banking in patients with cancer: 20-year experience. *Int J Andrology, Suppl.* 2000;23(2):16-19. doi:10.1046/j.1365-2605.2000.00005.x
50. Bauchet L, Rigau V, Mathieu-Daudé H, et al. French brain tumor data bank: Methodology and first results on 10,000 cases. *J Neurooncol.* 2007;84(2):189-199. doi:10.1007/s11060-007-9356-9
51. Kalkanis SN, Kast RE, Rosenblum ML, et al. Raman spectroscopy to distinguish grey matter, necrosis, and glioblastoma multiforme in frozen tissue sections. *J Neurooncol.* 2014;116(3):477-485. doi:10.1007/s11060-013-1326-9 PM - 24390405 M4 - Citavi
52. Dörr D, Stracke F, Zimmermann H. Noninvasive quality control of cryopreserved samples. *Biopreserv Biobank.* 2012;10(6):529-531. doi:10.1089/bio.2012.0011
53. Hibben JH. The Raman spectra of water, aqueous solutions and ice. *J Chem Phys.* 1937;5(3):166-172. doi:10.1063/1.1750001
54. Baumgartner M, Bakker RJ. Raman spectra of ice and salt hydrates in synthetic fluid inclusions. *Chem Geol.* 2010;275(1-2):58-66. doi:10.1016/j.chemgeo.2010.04.014
55. Engineering B. Thermodynamic Modeling of Activity Coefficient and Prediction of Solubility: Part 2. Semipredictive or Semiempirical Models. *Online.* 2006;95(4):798-809. doi:10.1002/jps
56. V. HD. Properties of paraffin waxesComposition by mass spectrometer

- analysis. *Ind Eng Chem*. 1955;47:1219.
57. Palou A, Cruz J, Blanco M, et al. Characterization of the composition of paraffin waxes on industrial applications. *Energy and Fuels*. 2014;28(2):956-963. doi:10.1021/ef4021813
 58. Kong H, West S. WMA DECLARATION OF HELSINKI – ETHICAL PRINCIPLES FOR Scientific Requirements and Research Protocols. 2013;(June 1964):29-32.
 59. Council OFTHE. (Text with EEA relevance). 2016;2014(October 1995).
 60. Cui L, Butler HJ, Martin-Hirsch PL, Martin FL. Aluminium foil as a potential substrate for ATR-FTIR, transfection FTIR or Raman spectrochemical analysis of biological specimens. *Anal Methods*. 2016;8(3):481-487. doi:10.1039/c5ay02638e
 61. Thomas P V., Ramakrishnan V, Vaidyan VK. Oxidation studies of aluminum thin films by Raman spectroscopy. *Thin Solid Films*. 1989;170(1):35-40. doi:10.1016/0040-6090(89)90619-6
 62. Hung PS, Kuo YC, Chen HG, Chiang HHK, Lee OKS. Detection of Osteogenic Differentiation by Differential Mineralized Matrix Production in Mesenchymal Stromal Cells by Raman Spectroscopy. *PLoS One*. 2013;8(5):1-7. doi:10.1371/journal.pone.0065438
 63. Downes A, Elfick A. Raman spectroscopy and related techniques in biomedicine. *Sensors*. 2010;10(3):1871-1889. doi:10.3390/s100301871
 64. Bowden M, Gardiner DJ, Rice G, Gerrard DL. Line-scanned micro Raman spectroscopy using a cooled CCD imaging detector. *J Raman Spectrosc*. 1990;21(1):37-41. doi:10.1002/jrs.1250210108
 65. Jermyn M, Ghadyani H, Mastanduno MA, et al. Fast segmentation and high-quality three-dimensional volume mesh creation from medical images for diffuse optical tomography. *J Biomed Opt*. 2013;18(8):86007.
 66. Podoleanu AG, Rogers JA, Jackson DA, Dunne S. Three dimensional OCT images from retina and skin. *Opt Express*. 2000;7(9):292. doi:10.1364/oe.7.000292
 67. *Machine Learning in Radiation Oncology.*; 2015. doi:10.1007/978-3-319-18305-3
 68. DePaoli D, Lemoine É, Ember K, et al. Rise of Raman spectroscopy in neurosurgery: a review. *J Biomed Opt*. 2020;25(05):1.

- doi:10.1117/1.jbo.25.5.050901
69. Likas A, Vlassis N, J. Verbeek J. The global k-means clustering algorithm. *Pattern Recognit.* 2003;36(2):451-461. doi:10.1016/S0031-3203(02)00060-2
 70. Shi N, Liu X, Guan Y. Research on k-means clustering algorithm: An improved k-means clustering algorithm. *3rd Int Symp Intell Inf Technol Secur Informatics, IITSI 2010.* 2010:63-67. doi:10.1109/IITSI.2010.74
 71. Pleil JD, Stiegel MA, Madden MC, Sobus JR. Heat map visualization of complex environmental and biomarker measurements. *Chemosphere.* 2011;84(5):716-723. doi:10.1016/j.chemosphere.2011.03.017
 72. Van der Maaten L, Hinton G. Visualizing Data using t-SNE. *J Mach Learn.* 2008:10.
 73. Hinton G, Roweis S. Stochastic neighbor embedding. *Adv Neural Inf Process Syst.* 2003.
 74. Yang Z, Fang KT, Kotz S. On the Student's t-distribution and the t-statistic. *J Multivar Anal.* 2007;98(6):1293-1304. doi:10.1016/j.jmva.2006.11.003
 75. Jelke F, Mirizzi G, Borgmann FK, et al. Intraoperative discrimination of native meningioma and dura mater by Raman spectroscopy. *Sci Rep.* 2021;11(1):1-10. doi:10.1038/s41598-021-02977-7
 76. Ben-hur A, Weston J. A User ' s Guide to Support Vector Machines. In: Carugo O, Eisenhaber F, eds. *Methods in Molecular Biology.* New York: Humana Press, c/o Springer Science + Business Media; 2009:223-239. doi:10.1007/978-1-60327-241-4
 77. Noble WS, Street P. What is a support vector machine ? *Nat Biotechnol.* 2006;24(12):1565-1567. doi:https://doi.org/10.1038/nbt1206-1565
 78. Rinnan Å, Berg F van den, Engelsen SB. Review of the most common pre-processing techniques for near-infrared spectra. *TrAC - Trends Anal Chem.* 2009;28(10):1201-1222. doi:10.1016/j.trac.2009.07.007
 79. Savitzky, A.; Golay MJE. Smoothing and Differentiation. *Anal Chem.* 1964;36(8):1627-1639.
 80. Li B, Calvet A, Casamayou-Boucau Y, Ryder AG. Kernel principal component analysis residual diagnosis (KPCARD): An automated method for cosmic ray artifact removal in Raman spectra. *Anal Chim Acta.* 2016;913:111-120. doi:10.1016/j.aca.2016.01.042
 81. Ying W. Department of Neurology, University of California at San Francisco

- and San Francisco Veterans Affairs Medical Center. *In Vivo (Brooklyn)*. 2006;3129-3148.
82. Maines MD. Heme oxygenase: function, multiplicity, regulatory mechanisms, and clinical applications. *FASEB J*. 1988;2(10):2557-2568. doi:10.1096/fasebj.2.10.3290025
 83. Lieber CA, Mahadevan-Jansen A. Automated Method for Subtraction of Fluorescence from Biological Raman Spectra. *Appl Spectrosc*. 2003;57(11):1363-1367. doi:10.1366/000370203322554518
 84. Gebrekidan MT, Knipfer C, Stelzle F, Popp J, Will S, Braeuer A. A shifted-excitation Raman difference spectroscopy (SERDS) evaluation strategy for the efficient isolation of Raman spectra from extreme fluorescence interference. *J Raman Spectrosc*. 2016;47(2):198-209. doi:10.1002/jrs.4775
 85. Mazilu M, De Luca AC, Riches A, Herrington CS, Dholakia K. Optimal algorithm for fluorescence suppression of modulated Raman spectroscopy. *Opt Express*. 2010;18(11):11382. doi:10.1364/oe.18.011382
 86. Samarkhanov K, Abuduwaili J, Samat A, Issanova G. The spatial and temporal land cover patterns of the Qazaly irrigation zone in 2003-2018: The case of Syrdarya river's lower reaches, Kazakhstan. *Sustain*. 2019;11(15). doi:10.3390/su11154035
 87. Chen S, Lin X, Yuen C, Padmanabhan S, Beuerman RW, Liu Q. Recovery of Raman spectra with low signal-to-noise ratio using Wiener estimation. *Opt Express*. 2014;22(10):12102. doi:10.1364/oe.22.012102
 88. Sandfort V, Goldschmidt J, Wöllenstein J, Palzer S. Cavity-enhanced raman spectroscopy for food chain management. *Sensors (Switzerland)*. 2018;18(3). doi:10.3390/s18030709
 89. Roy S, Chamberlin B, Matzger AJ. Polymorph discrimination using low wavenumber Raman spectroscopy. *Org Process Res Dev*. 2013;17(7):976-980. doi:10.1021/op400102e
 90. Koljenović S, Bakker Schut TC, Wolthuis R, et al. Tissue characterization using high wave number Raman spectroscopy. *J Biomed Opt*. 2005;10(3):031116. doi:10.1117/1.1922307
 91. Koljenović S, Schut TCB, Wolthuis R, Jong B De. Tissue characterization using high wave number Raman spectroscopy. 2005;10(June 2005):1-11. doi:10.1117/1.1922307

92. Yamakoshi H, Dodo K, Palonpon A, et al. Alkyne-tag Raman imaging for visualization of mobile small molecules in live cells. *J Am Chem Soc.* 2012;134(51):20681-20689. doi:10.1021/ja308529n
93. Masson LE, O'Brien CM, Pence IJ, et al. Dual excitation wavelength system for combined fingerprint and high wavenumber Raman spectroscopy. *Analyst.* 2018;143(24):6049-6060. doi:10.1039/c8an01989d
94. Mo J, Zheng W, Low JJH, Ng J, Ilancheran A, Huang Z. High wavenumber raman spectroscopy for in vivo detection of cervical dysplasia. *Anal Chem.* 2009;81(21):8908-8915. doi:10.1021/ac9015159
95. Chau AH, Motz JT, Gardecki JA, Waxman S, Bouma BE, Tearney GJ. Fingerprint and high-wavenumber Raman spectroscopy in a human-swine coronary xenograft in vivo. *J Biomed Opt.* 2008;13(4):040501. doi:10.1117/1.2960015
96. Santos LF, Wolthuis R, Koljenović S, Almeida RM, Puppels GJ. Fiber-optic probes for in vivo Raman spectroscopy in the high-wavenumber region. *Anal Chem.* 2005;77(20):6747-6752. doi:10.1021/ac0505730
97. Kerr LT, Byrne HJ, Hennelly BM. Optimal choice of sample substrate and laser wavelength for Raman spectroscopic analysis of biological specimen. *Anal Methods.* 2015;7(12):5041-5052. doi:10.1039/c5ay00327j
98. Fay MP, Proschan MA. Wilcoxon-Mann-Whitney or T-test? on assumptions for hypothesis tests and multiple interpretations of decision rules. *Stat Surv.* 2010;4:1-39. doi:10.1214/09-SS051
99. Armstrong RA. When to use the Bonferroni correction. *Ophthalmic Physiol Opt.* 2014;34(5):502-508. doi:10.1111/opo.12131
100. Movasaghi Z, Rehman S, Rehman IU. Raman Spectroscopy of Biological Tissues. *Appl Spectrosc Rev.* 2007;42(5):493-541. doi:10.1080/05704920701551530
101. Protasoni M, Sangiorgi S, Cividini A, et al. The collagenic architecture of human dura mater: Laboratory investigation. *J Neurosurg.* 2011;114(6):1723-1730. doi:10.3171/2010.12.JNS101732
102. Caffo M, Caruso G, Galatioto S, et al. Immunohistochemical study of the extracellular matrix proteins laminin, fibronectin and type IV collagen in secretory meningiomas. *J Clin Neurosci.* 2008;15(7):806-811. doi:10.1016/j.jocn.2007.05.029

103. Koljenović S, Schut TB, Vincent A, Kros JM, Puppels GJ. Detection of meningioma in dura mater by Raman spectroscopy. *Anal Chem.* 2005;77(24):7958-7965. doi:10.1021/ac0512599
104. Nguyen TT, Gobinet C, Feru J, Brassart-Pasco S, Manfait M, Piot O. Characterization of type I and IV collagens by Raman microspectroscopy: Identification of spectral markers of the dermo-epidermal junction. *Adv Biomed Spectrosc.* 2013;7(5):105-110. doi:10.3233/978-1-61499-184-7-105
105. Czamara K, Majzner K, Pacia MZ, Kochan K, Kaczor A, Baranska M. Raman spectroscopy of lipids: A review. *J Raman Spectrosc.* 2015;46(1):4-20. doi:10.1002/jrs.4607
106. Hsu JF, Hsieh PY, Hsu HY, Shigeto S. When cells divide: Label-free multimodal spectral imaging for exploratory molecular investigation of living cells during cytokinesis. *Sci Rep.* 2015;5(November):1-8. doi:10.1038/srep17541
107. Krafft C, Neudert L, Simat T, Salzer R. Near infrared Raman spectra of human brain lipids. *Spectrochim Acta A Mol Biomol Spectrosc.* 2005;61(7):1529-1535. doi:10.1016/j.saa.2004.11.017 PM - 15820887 M4 - Citavi
108. Kaneko S, Suero Molina E, Ewelt C, Warneke N, Stummer W. Fluorescence-Based Measurement of Real-Time Kinetics of Protoporphyrin IX After 5-Aminolevulinic Acid Administration in Human In Situ Malignant Gliomas. *Neurosurgery.* 2019;85(4):739-746. doi:10.1093/neuros/nyz129
109. Pichardo-Molina JL, Frausto-Reyes C, Barbosa-García O, et al. Raman spectroscopy and multivariate analysis of serum samples from breast cancer patients. *Lasers Med Sci.* 2007;22(4):229-236. doi:10.1007/s10103-006-0432-8
110. McKinney PA. Brain tumours: Incidence, survival, and aetiology. *Neurol Pract.* 2004;75(2):12-17. doi:10.1136/jnnp.2004.040741
111. Kasuga M, Ueki K, Tajima N, et al. Report of the Japan diabetes society/Japanese cancer association joint committee on diabetes and cancer. *Cancer Sci.* 2013;104(7):965-976. doi:10.1111/cas.12203
112. Nanda A, Bir SC, Maiti TK, Konar SK, Missios S, Guthikonda B. Relevance of Simpson grading system and recurrence-free survival after surgery for World Health Organization Grade I meningioma. *J Neurosurg.*

- 2017;126(1):201-211. doi:10.3171/2016.1.JNS151842
113. Zhou Y, Liu C, Cheng G, et al. Brain metastasis detection by resonant Raman optical biopsy method. *Opt Biopsy XII*. 2014;8940(212):89400C. doi:10.1117/12.2038731
114. Bergner N, Bocklitz T, Romeike BFM, et al. Identification of primary tumors of brain metastases by Raman imaging and support vector machines. *Chemom Intell Lab Syst*. 2012;117:224-232. doi:10.1016/j.chemolab.2012.02.008
115. Koljenović S, Choo-Smith LP in., Schut TCB, Kros JM, Van den Berge HJ, Puppels GJ. Discriminating vital tumor from necrotic tissue in human glioblastoma tissue samples by Raman spectroscopy. *Lab Investig*. 2002;82(10):1265-1277. doi:10.1097/01.LAB.0000032545.96931.B8
116. Lakomkin N, Hadjipanayis CG. The use of spectroscopy handheld tools in brain tumor surgery: Current evidence and techniques. *Front Surg*. 2019;6(May):1-7. doi:10.3389/fsurg.2019.00030
117. Ramina R, Coelho Neto M, Giacomelli A, et al. Optimizing costs of intraoperative magnetic resonance imaging. A series of 29 glioma cases. *Acta Neurochir (Wien)*. 2010;152(1):27-32. doi:10.1007/s00701-009-0430-2
118. Pelletier MJ. Quantitative Analysis Using Raman Spectroscopy. *Focal point, Appl Spectrosc*. 2003;57.
119. Kerr LT, Byrne HJ, Hennelly BM. Optimal choice of sample substrate and laser wavelength for Raman spectroscopic analysis of biological specimen. *Anal Methods*. 2015;7(12):5041-5052. doi:10.1039/c5ay00327j
120. Barroso EM, Smits RWH, Schut TCB, et al. Discrimination between Oral Cancer and Healthy Tissue Based on Water Content Determined by Raman Spectroscopy. *Anal Chem*. 2015;87(4):2419-2426. doi:10.1021/ac504362y
121. Frank CJ, McCreary RL, Redd DCB. Raman Spectroscopy of Normal and Diseased Human Breast Tissues. *Anal Chem*. 1995;67(5):777-783. doi:10.1021/ac00101a001
122. Kalkanis SN, Kast RE, Rosenblum ML, et al. Raman spectroscopy to distinguish grey matter, necrosis, and glioblastoma multiforme in frozen tissue sections. *J Neurooncol*. 2014;116(3):477-485. doi:10.1007/s11060-013-1326-9 PM - 24390405 M4 - Citavi
123. Wills H, Kast R, Stewart C, et al. Raman spectroscopy detects and

- distinguishes neuroblastoma and related tissues in fresh and (banked) frozen specimens. *J Pediatr Surg*. 2009;44(2):386-391.
doi:10.1016/j.jpedsurg.2008.10.095
124. Caspers PJ, Lucassen GW, Carter EA, Bruining HA, Puppels GJ. In vivo confocal raman microspectroscopy of the skin: Noninvasive determination of molecular concentration profiles. *J Invest Dermatol*. 2001;116(3):434-442.
doi:10.1046/j.1523-1747.2001.01258.x
 125. Jermyn M, Mok K, Mercier J, et al. Intraoperative brain cancer detection with Raman spectroscopy in humans. *Sci Transl Med*. 2015.
doi:10.1126/scitranslmed.aaa2384
 126. Desroches J, Jermyn M, Mok K, et al. Characterization of a Raman spectroscopy probe system for intraoperative brain tissue classification. *Biomed Opt Express*. 2015. doi:10.1364/BOE.6.002380
 127. Jermyn M, Desroches J, Mercier J, et al. Raman spectroscopy detects distant invasive brain cancer cells centimeters beyond MRI capability in humans. *Biomed Opt Express*. 2016;7(12):5129. doi:10.1364/boe.7.005129
 128. Estrada LI, Robinson AA, Amaral AC, et al. Evaluation of Long-Term Cryostorage of Brain Tissue Sections for Quantitative Histochemistry. *J Histochem Cytochem*. 2017;65(3):153-171. doi:10.1369/0022155416686934
 129. Jones D. The reaction of formaldehyde with unsaturated fatty acids during histological fixation. *Histochem J*. 1969;1(5):459-491.
 130. Chandler WF, Knake JE, McGillicuddy JE, Lillehei KO, Silver TM. Intraoperative use of real-time ultrasonography in neurosurgery. *J Neurosurg*. 1982;57(2):157-163. doi:10.3171/jns.1982.57.2.0157
 131. Black PML, Moriarty T, Alexander E, et al. Development and implementation of intraoperative magnetic resonance imaging and its neurosurgical applications. *Neurosurgery*. 1997;41(4):831-845. doi:10.1097/00006123-199710000-00013
 132. Tilgner J, Herr M, Ostertag C, Volk B. Validation of intraoperative diagnoses using smear preparations from stereotactic brain biopsies: Intraoperative versus final diagnosis - Influence of clinical factors. *Neurosurgery*. 2005;56(2):257-263. doi:10.1227/01.NEU.0000148899.39020.87
 133. Comeau RM, Sadikot AF, Fenster A, Peters TM. Intraoperative ultrasound for guidance and tissue shift correction in image-guided neurosurgery. *Med*

- Phys.* 2000;27(4):787-800. doi:10.1118/1.598942
134. Krafft C, Sobottka SB, Schackert G, Salzer R. Raman and infrared spectroscopic mapping of human primary intracranial tumors: A comparative study. *J Raman Spectrosc.* 2006;37(1-3):367-375. doi:10.1002/jrs.1450
 135. Zhou Y, Liu C-H, Sun Y, et al. Human brain cancer studied by resonance Raman spectroscopy. *J Biomed Opt.* 2012;17(11):116021. doi:10.1117/1.jbo.17.11.116021
 136. Aguiar RP, Silveira L, Falca ET, et al. Discriminating Neoplastic and Normal Brain Tissues in Vitro Through Raman Spectroscopy : *Photomed Laser Surg.* 2013;31(12):595-604. doi:10.1089/pho.2012.3460
 137. Huang Z, McWilliams A, Lui H, McLean DI, Lam S, Zeng H. Near-infrared Raman spectroscopy for optical diagnosis of lung cancer. *Int J Cancer.* 2003;107(6):1047-1052. doi:10.1002/ijc.11500
 138. Cheng WT, Liu MT, Liu HN, Lin SY. Micro-Raman spectroscopy used to identify and grade human skin pilomatrixoma. *Microsc Res Tech.* 2005;68(2):75-79. doi:10.1002/jemt.20229
 139. Chan JW, Taylor DS, Zwerdling T, Lane SM, Ihara K, Huser T. Micro-raman spectroscopy detects individual neoplastic and normal hematopoietic cells. *Biophys J.* 2006;90(2):648-656. doi:10.1529/biophysj.105.066761
 140. Shetty G, Kendall C, Shepherd N, Stone N, Barr H. Raman spectroscopy: Elucidation of biochemical changes in carcinogenesis of oesophagus. *Br J Cancer.* 2006;94(10):1460-1464. doi:10.1038/sj.bjc.6603102
 141. Malini R, Venkatakrishna K, Kurien J, et al. Discrimination of Normal, Inflammatory, Premalignant, and Malignant Oral Tissue: A Raman Spectroscopy Study. *Biopolymers.* 2006;81:179-193. doi:10.1002/bip.20398
 142. Sigurdsson S, Philipsen PA, Hansen LK, Larsen J, Gniadecka M, Christian Wulf H. Detection of skin cancer by classification of Raman spectra. *IEEE Trans Biomed Eng.* 2004;51(10):1784-1793. doi:10.1109/TBME.2004.831538
 143. Shafer-Peltier KE, Haka AS, Motz JT, Fitzmaurice M, Dasari RR, Feld MS. Model-based biological Raman spectral imaging. *J Cell Biochem.* 2002;137(SUPPL. 39):125-137. doi:10.1002/jcb.10418
 144. Dieter Naumann. Infrared and NIR Raman spectroscopy in medical microbiology. *Infrared Spectrosc New Tool Med.* 1998;3257(i):245-257.

145. Binoy J, Abraham JP, Joe IH, Jayakumar VS, Pettit GR, Nielsen OF. NIR-FT Raman and FT-IR spectral studies and ab initio calculations of the anti-cancer drug combretastatin-A4. *J Raman Spectrosc.* 2004;35(11):939-946. doi:10.1002/jrs.1236
146. Votteler M, Carvajal Berrio DA, Pudlas M, Walles H, Stock UA, Schenke-Layland K. Raman spectroscopy for the non-contact and non-destructive monitoring of collagen damage within tissues. *J Biophotonics.* 2012;5(1):47-56. doi:10.1002/jbio.201100068
147. Aguiar RP, Silveira L, Falca ET, et al. Discriminating Neoplastic and Normal Brain Tissues in Vitro Through Raman Spectroscopy : *Photomed Laser Surg.* 2013;31(12):595-604. doi:10.1089/pho.2012.3460

11 Acknowledgements

I would like to thank Prof. Dr. med. Frank Hertel, for all the constructive critics and a constant encouragement for further experiments and ideas. I am really grateful for the whole INSITU group, having welcome me with open arms to their amazing team. I appreciate the opportunity given by the department of neurosurgery from the UKS Homburg to write this thesis. At this point, I want to express a special thank to Felix Kleine-Borgmann and Finn Jelke for hours of discussion, whole classifier ideas written on the inside of a chocolate paper during a healthful meeting and their enthusiasm for new ideas. For the endless moral support, motivational coffee breaks and their listening I would like to thank my family and friends, especially N.T. and L.K.

12 Supplements

12.1 Supplement1: WHO-Classification of CNS tumors 2016 and 2021

This table is based on the table of content of the 2016th and the 2021th WHO-Classification for tumors of the human CNS and should give an overview on the different tumor-classifications between 2016 and 2021.

Tumortype 2016th WHO-Classification²	Tumortype 2021th WHO-Classification³
Diffuse astrocytic and oligodendroglial tumours	Gliomas, glioneuronal tumors, and neuronal tumors
Diffuse astrocytoma, IDH-mutant Gemistocytic astrocytoma, IDH-mutant Diffuse astrocytoma, IDH-wildtype Diffuse astrocytoma, NOS Anaplastic astrocytoma, IDH-mutant Anaplastic astrocytoma, IDH-wildtype Anaplastic astrocytoma, NOS Glioblastoma, IDH-wildtype Giant cell glioblastoma Gliosarcoma Epithelioid glioblastoma Glioblastoma, IDH-mutant Glioblastoma, NOS Diffuse midline glioma, H3 K27M-mutant Oligodendroglioma, IDH-mutant and 1p/19q-codeleted Oligodendroglioma, NOS Anaplastic oligodendroglioma, IDH-mutant and 1p/19q-codeleted Anaplastic oligodendroglioma, NOS Oligoastrocytoma, NOS Anaplastic oligoastrocytoma, NOS	Adult-type diffuse gliomas Astrocytoma, IDH-mutant Oligodendroglioma, IDH-mutant, and 1p/19q-codeleted Glioblastoma, IDH-wildtype Pediatric-type diffuse low-grade gliomas Diffuse astrocytoma, MYB- or MYBL1-altered Angiocentric glioma Polymorphous low-grade neuroepithelial tumor of the young Diffuse low-grade glioma, MAPK pathway-altered Pediatric-type diffuse high-grade gliomas Diffuse midline glioma, H3 K27-altered Diffuse hemispheric glioma, H3 G34-mutant Diffuse pediatric-type high-grade glioma, H3-wildtype and IDH-wildtype Infant-type hemispheric glioma Circumscribed astrocytic gliomas Pilocytic astrocytoma High-grade astrocytoma with piloid features Pleomorphic xanthoastrocytoma Subependymal giant cell astrocytoma Chordoid glioma Astroblastoma, MN1-altered Glioneuronal and neuronal tumors Ganglioglioma Desmoplastic infantile ganglioglioma / desmoplastic infantile astrocytoma Dysembryoplastic neuroepithelial tumor Diffuse glioneuronal tumor with oligodendroglioma-like features and nuclear clusters Papillary glioneuronal tumor Rosette-forming glioneuronal tumor Myxoid glioneuronal tumor Diffuse leptomeningeal glioneuronal tumor Gangliocytoma Multinodular and vacuolating neuronal tumor Dysplastic cerebellar gangliocytoma (Lhermitte-Duclos disease) Central neurocytoma Extraventricular neurocytoma Cerebellar liponeurocytoma
Other astrocytic tumours	
Pilocytic astrocytoma Pilomyxoid astrocytoma Subependymal giant cell astrocytoma Pleomorphic xanthoastrocytoma Anaplastic pleomorphic xanthoastrocytoma	
Ependymal tumours	Ependymal tumors
Subependymoma Myxopapillary ependymoma Ependymoma Papillary ependymoma Clear cell ependymoma Tanycytic ependymoma	Supratentorial ependymoma Supratentorial ependymoma, ZFTA fusion-positive Supratentorial ependymoma, YAP1 fusion-positive Posterior fossa ependymoma Posterior fossa ependymoma, group PFA Posterior fossa ependymoma, group PFB

Ependymoma, RELA fusion-positive Anaplastic ependymoma	Spinal ependymoma Spinal ependymoma, MYCN-amplified Myxopapillary ependymoma Subependymoma
Other gliomas	
Chordoid glioma of the third ventricle Angiocentric glioma Astroblastoma	
Choroid plexus tumours	Choroid plexus tumours
Choroid plexus papilloma Atypical choroid plexus papilloma Choroid plexus carcinoma	Choroid plexus papilloma Atypical choroid plexus papilloma Choroid plexus carcinoma
Neuronal and mixed neuronal-glioma tumours	
Dysembryoplastic neuroepithelial tumour Gangliocytoma Ganglioglioma Anaplastic ganglioglioma Dysplastic cerebellar gangliocytoma (Lhermitte-Duclos disease) Desmoplastic infantile astrocytoma and ganglioglioma Papillary glioneuronal tumour Rosette-forming glioneuronal tumour Diffuse leptomeningeal glioneuronal tumour Central neurocytoma Extraventricular neurocytoma Cerebellar liponeurocytoma Paraganglioma	
Tumours of the pineal region	Pineal tumours
Pineocytoma Pineal parenchymal tumour of intermediate differentiation Pineoblastoma Papillary tumour of the pineal region	Pineocytoma Pineal parenchymal tumor of intermediate differentiation Pineoblastoma Papillary tumor of the pineal region Desmoplastic myxoid tumor of the pineal region, SMARCB1-mutant
Embryonal tumours	Embryonal tumours
Medulloblastoma Medulloblastoma, NOS Medulloblastomas, genetically defined Medulloblastoma, WNT-activated Medulloblastoma, SHH-activated and TP53-mutant Medulloblastoma, SHH-activated and TP53-wildtype Medulloblastomas, histologically defined Medulloblastoma, classic Desmoplastic/nodular medulloblastoma Medulloblastoma with extensive nodularity Large cell / anaplastic medulloblastoma Embryonal tumour with multilayered rosettes, C19MC-altered Embryonal tumour with multilayered rosettes, NOS Other CNS embryonal tumours Medulloepithelioma CNS neuroblastoma CNS ganglioneuroblastoma CNS embryonal tumour, NOS Atypical teratoid/rhabdoid tumour CNS embryonal tumour with rhabdoid features	Medulloblastoma Medulloblastomas, molecularly defined Medulloblastoma, WNT-activated Medulloblastoma, SHH-activated and TP53-wildtype Medulloblastoma, SHH-activated and TP53-mutant Medulloblastoma, non-WNT/non-SHH Medulloblastomas, histologically defined Other CNS embryonal tumors Atypical teratoid/rhabdoid tumor Cribriform neuroepithelial tumor Embryonal tumor with multilayered rosettes CNS neuroblastoma, FOXR2-activated CNS tumor with BCOR internal tandem duplication CNS embryonal tumor
Tumours of the cranial and paraspinal nerves	Cranial and paraspinal nerve tumors
Schwannoma Cellular schwannoma Plexiform schwannoma Melanotic schwannoma Neurofibroma Atypical neurofibroma Plexiform neurofibroma Perineurioma Hybrid nerve sheath tumours Malignant peripheral nerve sheath tumour (MPNST) MPNST with divergent differentiation Epithelioid MPNST MPNST with perineurial differentiation	Schwannoma Neurofibroma Perineurioma Hybrid nerve sheath tumor Malignant melanotic nerve sheath tumor Malignant peripheral nerve sheath tumor Paraganglioma
Meningiomas	Meningiomas
Meningioma	Meningioma

<p>Meningioma variants</p> <ul style="list-style-type: none"> Meningothelial meningioma Fibrous meningioma Transitional meningioma Psammomatous meningioma Angiomatous meningioma Microcystic meningioma Secretory meningioma Lymphoplasmacyte-rich meningioma Metaplastic meningioma Chordoid meningioma Clear cell meningioma Atypical meningioma Papillary meningioma Rhabdoid meningioma Anaplastic (malignant) meningioma 	
<p>Mesenchymal, non-meningothelial tumours</p> <ul style="list-style-type: none"> Solitary fibrous tumour / haemangiopericytoma Haemangioblastoma Haemangioma Epithelioid haemangioendothelioma Angiosarcoma Kaposi sarcoma Ewing sarcoma / peripheral primitive neuroectodermal tumour Lipoma Angiolipoma Hibernoma Liposarcoma Desmoid-type fibromatosis Myofibroblastoma Inflammatory myofibroblastic tumour Benign fibrous histiocytoma Fibrosarcoma Undifferentiated pleomorphic sarcoma / malignant fibrous histiocytoma Leiomyoma Leiomyosarcoma Rhabdomyoma Rhabdomyosarcoma Chondroma Chondrosarcoma Osteoma Osteochondroma Osteosarcoma 	<p>Mesenchymal, non-meningothelial tumours</p> <ul style="list-style-type: none"> Soft tissue tumors <ul style="list-style-type: none"> Fibroblastic and myofibroblastic tumors <ul style="list-style-type: none"> Solitary fibrous tumor Vascular tumors <ul style="list-style-type: none"> Hemangiomas and vascular malformations Hemangioblastoma Skeletal muscle tumors <ul style="list-style-type: none"> Rhabdomyosarcoma Uncertain differentiation <ul style="list-style-type: none"> Intracranial mesenchymal tumor, FET-CREB fusion-positive CIC-rearranged sarcoma Primary intracranial sarcoma, DICER1-mutant Ewing sarcoma Chondro-osseous tumors <ul style="list-style-type: none"> Chondrogenic tumors <ul style="list-style-type: none"> Mesenchymal chondrosarcoma Chondrosarcoma Notochordal tumors <ul style="list-style-type: none"> Chordoma (including poorly differentiated chordoma)
<p>Melanocytic tumours</p> <ul style="list-style-type: none"> Meningeal melanocytosis Meningeal melanomatosis Meningeal melanocytoma Meningeal melanoma 	<p>Melanocytic tumours</p> <ul style="list-style-type: none"> Diffuse meningeal melanocytic neoplasms <ul style="list-style-type: none"> Meningeal melanocytosis and meningeal melanomatosis Circumscribed meningeal melanocytic neoplasms <ul style="list-style-type: none"> Meningeal melanocytoma and meningeal melanoma
<p>Lymphomas</p> <ul style="list-style-type: none"> Diffuse large B-cell lymphoma of the CNS <ul style="list-style-type: none"> Corticoid-mitigated lymphoma Sentinel lesions Immunodeficiency-associated CNS lymphomas <ul style="list-style-type: none"> AIDS-related diffuse large B-cell lymphoma EBV+ diffuse large B-cell lymphoma, NOS Lymphomatoid granulomatosis Intravascular large B-cell lymphoma Miscellaneous rare lymphomas in the CNS <ul style="list-style-type: none"> Low-grade B-cell lymphomas T-cell and NK/T-cell lymphomas Anaplastic large cell lymphoma (ALK+/ALK-) MALT lymphoma of the dura 	<p>Hematolymphoid tumours</p> <ul style="list-style-type: none"> Lymphomas <ul style="list-style-type: none"> CNS lymphomas <ul style="list-style-type: none"> Primary diffuse large B-cell lymphoma of the CNS Immunodeficiency-associated CNS lymphoma Lymphomatoid granulomatosis Intravascular large B-cell lymphoma Miscellaneous rare lymphomas in the CNS <ul style="list-style-type: none"> MALT lymphoma of the dura Other low-grade B-cell lymphomas of the CNS Anaplastic large cell lymphoma (ALK+/ALK-) T-cell and NK/T-cell lymphomas
<p>Histiocytic tumours</p> <ul style="list-style-type: none"> Langerhans cell histiocytosis Erdheim-Chester disease Rosai-Dorfman disease Juvenile xanthogranuloma Histiocytic sarcoma 	<p>Histiocytic tumours</p> <ul style="list-style-type: none"> Erdheim-Chester disease Rosai-Dorfman disease Juvenile xanthogranuloma Langerhans cell histiocytosis Histiocytic sarcoma
<p>Germ cell tumours</p> <ul style="list-style-type: none"> Germinoma 	<p>Germ cell tumours</p> <ul style="list-style-type: none"> Mature teratoma

Embryonal carcinoma Yolk sac tumour Choriocarcinoma Teratoma Mature teratoma Immature teratoma Teratoma with malignant transformation Mixed germ cell tumour	Immature teratoma Teratoma with somatic-type malignancy Germinoma Embryonal carcinoma Yolk sac tumor Choriocarcinoma Mixed germ cell tumor
Familial tumour syndromes Neurofibromatosis	
Neurofibromatosis type 1 Neurofibromatosis type 2 Schwannomatosis Von Hippel-Lindau disease Tuberous sclerosis Li-Fraumeni syndrome Cowden syndrome Turcot syndrome Mismatch repair cancer syndrome Familial adenomatous polyposis Naevoid basal cell carcinoma syndrome Rhabdoid tumour predisposition syndrome	
Tumours of the sellar region	Tumors of the sellar region
Craniopharyngioma Adamantinomatous craniopharyngioma Papillary craniopharyngioma Granular cell tumour of the sellar region Pituicytoma Spindle cell oncocytoma	Adamantinomatous craniopharyngioma Papillary craniopharyngioma Pituicytoma, granular cell tumor of the sellar region, and spindle cell oncocytoma Pituitary adenoma/PitNET Pituitary blastoma
Metastatic tumours	Metastases to the CNS
	Metastases to the brain and spinal cord parenchyma Metastases to the meninges

12.2 Supplement2: Informed Consent

11.08.2018 V3

FEUILLE D'INFORMATION AUX PATIENTS / PARTICIPANTS OPERES

NOM DE L'ETUDE

INSITU – Innovative Spectroscopy and Imaging for Tumors

PERSONNE DE CONTACT POUR TOUTE DEMANDE D'INFORMATION

Prof. Frank Hertel

Vous êtes invité(e) à prendre part à une étude de recherche au sein de notre institution. Ce document est destiné à mieux vous informer afin que vous puissiez donner votre consentement ou refuser de participer à cette étude. Votre participation est entièrement volontaire. Si vous décidez de participer à cette étude, vous pourrez vous retirer à tout moment. Cette étude a reçu un avis positif du Comité National d'Ethique de Recherche.

Objectif et description de l'étude

Chère patiente, cher patient,

Vous avez bénéficié d'une prise en charge chirurgicale pour exérèse d'un processus expansif lié au système nerveux (par exemple une tumeur intracrânienne ou une tumeur de la colonne vertébrale). Le tissu prélevé est envoyé pour analyse anatomopathologique pouvant être complétée par une analyse moléculaire.

Dans le cadre d'une collaboration entre le CHL, l'université du Luxembourg (LCSB), le laboratoire national de santé (LNS) et le Luxembourg Institute of Health (LIH), nous sollicitons votre accord pour utiliser un fragment du tissu prélevé afin de réaliser d'autres analyses à des fins scientifiques dans le but d'optimiser la caractérisation des tissus. Aucun tissu complémentaire, notamment du tissu sain, ne sera prélevé durant la prise en charge chirurgicale.

L'étude consiste à analyser ce tissu selon une technique particulière de spectroscopie, en péri-opératoire, avant que ce tissu ne soit envoyé pour analyse anatomopathologique. La détermination de l'origine exacte du tissu analysé est permise par l'utilisation péri-opératoire du système de neuronavigation utilisé de façon standard lors d'une procédure d'exérèse d'un processus expansif intracrânien. Il s'agit d'un matériel de guidage chirurgical sur base des données d'imagerie préopératoires à l'instar d'un système de navigation GPS utilisant des cartes routières.

Avant de réaliser toute analyse scientifique, les échantillons de tissus, les données de localisation du prélèvement et les données personnelles seront pseudonymisées. La pseudonymisation est une technique de protection de données personnelles par laquelle un pseudonyme (souvent un alignement de lettres et de chiffres qui forme un code, p.ex. Mme Schmidt devient Cas1) remplace le nom de l'individu auquel se rattachent les données. Contrairement au processus d'anonymisation, la pseudonymisation est réversible via un tableau clé de données. Dans notre projet d'étude, seul l'investigateur principal a accès à ce tableau. Par conséquent, à l'exception des membres du service national de Neurochirurgie, aucun intervenant de l'étude n'aura accès à vos données médicales y compris les intervenants

de l'université de Luxembourg ou du LIH. Le processus de pseudonymisation est nécessaire afin d'offrir au participant la possibilité de se retirer du projet d'étude.

Dans une deuxième partie du projet d'étude et dans le cadre d'une coopération scientifique internationale, les données relatives aux profils tumoraux seront échangées pour définir un profil type pour le diagnostic de chaque type de tumeur. Cette coopération scientifique nécessite un échange de données qui dans ce cas seront anonymisées.

L'anonymisation consiste à modifier le contenu des données afin de rendre la « ré-identification » impossible. Aucun intervenant de l'étude y compris l'investigateur principal du service national de neurochirurgie n'a la capacité de lier les données tumorales à un patient après l'anonymisation.

Afin de procéder à l'analyse spectroscopique du tissu tumoral, seul le tissu prélevé dans le cadre de l'opération et destiné à être envoyé pour analyse anatomopathologique est utilisé.

Aucun matériel ne sera prélevé en plus du matériel nécessaire pour l'analyse anatomopathologique. La participation à l'étude n'entraîne aucun risque supplémentaire pour le patient dans le décours de la procédure chirurgicale. Par ailleurs, aucun examen clinique ou d'imagerie médicale complémentaire n'est nécessaire dans le cadre de la participation à l'étude hormis les examens de suivi dans un souci de routine clinique standard et de bonne pratique. Pour le participant, aucun avantage ni désavantage n'est à considérer. La participation à cette étude est gratuite.

L'étude poursuit strictement un but scientifique et non commercial. Ce dernier est d'améliorer les différentes stratégies thérapeutiques dans le cadre des processus expansifs intracrâniens notamment tumoraux constituant un intérêt majeur en termes de progrès médical.

Risques ou désagréments possibles

La participation ou le refus de participation à l'étude n'entraîne aucun avantage ou désavantage dans le cadre de la prise en charge.

Protection de la vie privée

Toute collection de données est faite au sein du CHL. Toutes les données récoltées sont pseudonymisées. Dans le processus de la pseudonymisation, le nom ou d'autres données personnelles sont remplacés par un pseudonyme, l'identité du patient n'est plus déterminable. Le processus de pseudonymisation des données est réservé aux membres de l'équipe de Neurochirurgie du CHL. Par conséquent, d'une part, aucun des participants à l'étude hors des membres du CHL n'a accès aux données médicales d'un patient X, et d'autre part, ce même patient peut soumettre son droit de se rétracter vis-à-vis de la participation à cette étude et voir ces données supprimées de l'étude. L'analyse des données pseudonymisées sera réalisée via des serveurs de l'université de Luxembourg /LCSB, du LIH et/ou du LNS.

Hors du Luxembourg, ces données seront uniquement transmises au centre de coordination de l'étude internationale. Ces données, dans le cadre de la coopération scientifique internationale, sont quant à elles strictement anonymes. Il est donc impossible à ce stade pour le patient de se retirer de l'étude. En effet, une anonymisation complète des données a pour conséquence l'impossibilité de procéder au retrait des données dudit patient, les données n'ayant plus aucun lien avec ce dernier.

Rappelons par ailleurs que les données collectées sont sauvegardées selon des normes scientifiques strictes et toujours dans le cadre de la bonne pratique scientifique (GSP - good scientific practice) et clinique (GCP - good clinical practice).

13.08.2018 V 3

FORMULAIRE DE CONSENTEMENT ECLAIRE

NOM DE L'ETUDE

INSITU – Innovative Spectroscopy and Imaging for Tumors

PERSONNE DE CONTACT POUR TOUTE DEMANDE D'INFORMATION

Prof. Frank HERTEL

Je soussigné(e), confirme par la présente que j'ai reçu suffisamment d'informations concernant cette étude de la part de mon médecin, et que j'ai lu la feuille d'information attachée et en ai compris le sens.

Je suis conscient(e) que ma participation à cette étude est entièrement volontaire et que je peux mettre fin à tout moment à ma participation sans que cela me porte préjudice.

Mes données personnelles seront traitées de manière strictement confidentielle, comme prévu dans la Loi du 1er août 2018 portant organisation de la Commission nationale pour la protection des données et du régime général sur la protection des données et le texte « EU General Data Protection Regulation GDPR ». Je comprends les raisons pour lesquelles ces données sont collectées, traitées et utilisées dans le cadre de cette étude.

J'accepte librement de participer à cette étude et de satisfaire aux conditions telles qu'elles sont décrites dans la feuille d'information attachée.

Nom du patient ou de la patiente :

Date :

Signature patient(e) :

Partie réservée au médecin traitant :

Je soussigné(e), _____, confirme avoir informé le patient/la personne ci-dessus, des buts, de la nature, la durée ainsi que les risques et procédures de cette étude, et qu'il (elle) a accepté de participer à cette étude.

Date :

Signature :

12.3 Supplement3: List of used abbreviations

Healthy Tissue

Tag	Long version
Fat	Fat
CNS	CNS tissue
GM	Grey Matter
WM	White Matter
Arach	Arachnoid mater
Dura	Dura mater
CSF	Cerebrospinal fluid (Liquor cerebrospinalis)
B	Bone
Cart	Cartilage
Sk	Skin
SCFT	Subcutaneous fat tissue
Dis	Discus vertebralis
Fibr	Fibrous connective tissue
VesVLI	Vessel, identified in visible light image (VLI)
Blood	Blood
Mus	Skeletal muscle
B_mar	Bone marrow
H	Hair

Modified Tissue

Tag	Long version
modCNS	Modified CNS tissue
modVes	Malignantly altered blood vessel
Coag	Coagulated blood
InfZo	Infiltration zone
N	Necrosis
Inflamm	Inflammation

Diffuse astrocytic and oligodendroglial tumors

Tag	Long Version
GBM	Glioblastoma
DA	Diffuse astrocytoma
AA	Anaplastic astrocytoma
PA	Pilocytic astrocytoma
SEGA	Subependymal giant cell astrocytoma
DMG	Diffuse midline glioma
ODG	Oligodendroglioma
ODG_ana III	Anaplastic oligodendroglioma

Ependymal tumors

Tag	Lon version
EDY	Ependymal tumor

Choroid plexus tumors

Tag	Long Version
CPT	Choroid plexus tumor

Neuronal & mixed neuronal-glia tumors

Tag	Long version
NT	Neuronal tumor
DNET	Dysembryoplastic neuroepithelial tumor
GLGL	Ganglioglioma

Embryonal tumors

Tag	Long Version
MDB	Medulloblastoma

Nerve sheath tumors

Tag	Long version
Sch	Schwannoma
NF	Neurofibroma

Meningiomas

Tag	Long version
MGM_NOS	Meningioma not otherwise specified
MGM_men	Meningothelial meningioma
MGM_fibr	Fibrous meningioma
MGM_tra	Transitional meningioma
MGM_aty	Atypical meningioma
MGM_sec	secretory meningioma

Mesenchymal, non-meningothelial tumors

Tag	Long version
MES	Mesenchymal, non-meningothelial tumor (super group)
Sarc	Sarcoma
HAP	Hemangiopericytoma
HAB	Hemangioblastoma
VMF	Vessel malformation
LMF	Lipid malformation (lipoma, liposarcoma, ...)
OMF	Osseous malformation (osteosarcoma, ...)
CMF	Cartilagenous malformation (chordoma, ...)
FMF	Fibrous malformation
MMF	Muscular malformation

Lymphomas

Tag	Long version
LYM	Lymphoma
DLBCL	Diffuse large B-cell lymphoma

Germ-cell tumors

Tag	Long version
GCL	Germ-cell tumor (super group)
Terat	Teratoma
Derm	Dermoid cyst

Tumors of the pituitary gland

Tag	Long version
PIT	Tumors of the pituitary gland

Metastatic tumors

Tag	Long version
MET	Metastasis

Primary of metastasis

Tag	Long version
MET_Pul	Lung cancer
MET_NSCL	Non-small-cell lung carcinoma
MET_Br	Breast cancer
MET_GIT	Gastro intestinal tumor
MET_Mel	Melanoma
MET_RCC	Renal cell carcinoma
MET_UT	Urologic tumor
MET_CUP	Cancer of unknown primary
MET_CNS	CNS carcinoma
MET_PCa	Prostate carcinoma
MET_LMSar	Leiomyosarcoma

Properties

Tag	Long version
ALA+	Gliolan® (5-ALA) positive
ALA-	Gliolan® (5-ALA) negative
Con+	Contrast enhancement in MRI
Con-	Non-contrastive in MRI
NAT	Native, unfixed
FOR	Fixed in formalin
CRU	Crushed
FRO	Frozen
Coag	Coagulated tissue
CUSA	Cavitron ultrasonic surgical aspirator®
SteBio	Stereotactic biopsy
Rec	Tumor recurrence

Background

Tag	Long version
Alu	Aluminum
Pla	Plastic



OPEN

Intraoperative discrimination of native meningioma and dura mater by Raman spectroscopy

Finn Jelke^{1,2,6}, Giulia Mirizzi^{1,2,6}, Felix Kleine Borgmann^{2,4,5}, Andreas Husch³, Rédouane Slimani⁴, Gilbert Georg Klamminger^{2,5}, Karoline Klein², Laurent Mombaerts³, Jean-Jacques Gérardy⁵, Michel Mittelbronn^{4,5} & Frank Hertel^{1,2,3✉}

Meningiomas are among the most frequent tumors of the central nervous system. For a total resection, shown to decrease recurrences, it is paramount to reliably discriminate tumor tissue from normal dura mater intraoperatively. Raman spectroscopy (RS) is a non-destructive, label-free method for vibrational analysis of biochemical molecules. On the microscopic level, RS was already used to differentiate meningioma from dura mater. In this study we test its suitability for intraoperative macroscopic meningioma diagnostics. RS is applied to surgical specimen of intracranial meningiomas. The main purpose is the differentiation of tumor from normal dura mater, in order to potentially accelerate the diagnostic workflow. The collected meningioma and dura mater samples ($n = 223$ tissue samples from a total of 59 patients) are analyzed under untreated conditions using a new partially robotized RS acquisition system. Spectra ($n = 1273$) are combined with the according histopathological analysis for each sample. Based on this, a classifier is trained via machine learning. Our trained classifier separates meningioma and dura mater with a sensitivity of $96.06 \pm 0.03\%$ and a specificity of $95.44 \pm 0.02\%$ for internal fivefold cross validation and 100% and 93.97% if validated with an external test set. RS is an efficient method to discriminate meningioma from healthy dura mater in fresh tissue samples without additional processing or histopathological imaging. It is a quick and reliable complementary diagnostic tool to the neuropathological workflow and has potential for guided surgery. RS offers a safe way to examine unfixed surgical specimens in a perioperative setting.

Meningiomas (MGM) constitute some of the most frequent tumors of the central nervous system (CNS) with a lifetime-risk of approximately 1%. They are a diverse group of mesenchymal tumor entities, deriving from arachnoid cap cells².

Radiological diagnostics of meningiomas is usually accomplished either by magnetic resonance imaging (MRI) or computed tomography (CT) scan. The gold-standard of treatment is the complete surgical resection. Complementary approaches can be radiosurgery/radiotherapy, or in some cases application of hormonal treatment^{3,4} or immunotherapy⁵. After successful surgical resection, the recurrence rate is between 7 and 25% for benign (WHO I), 29–52% for atypical (WHO II) and 50–94% for anaplastic meningiomas (WHO III)^{1,6}. The recurrence rate negatively correlates with the extent of resection^{2,7}. The main goal of surgical resection should always be a Simpson-grade I resection, concomitant with a symptomatic 10-year recurrence of 9%. It is often difficult to exactly distinguish the tumor border or differentiate infiltrated dura mater from adjacent healthy tissue². Therefore, a technical support could be helpful to complete the tumor removal. Intraoperative neuropathological diagnostics (smear or snap frozen) arrive time-delayed, are invasive and rarely used in meningioma surgery. An intraoperative MRI or CT scan is time-consuming and associated with logistic challenges as well as high costs⁸. Several spectroscopic techniques such as infrared and nuclear magnetic resonance spectroscopy^{9,10} as well as Raman spectroscopy (RS) are under investigation for this tissue diagnostics, especially the latter shows a great potential for tumor differentiation^{11–22}. The Raman effect occurs during the interaction with the specific vibrational mode of molecular functional groups, when photons either gather or loose energy (Stokes and Anti-Stokes

¹Centre Hospitalier de Luxembourg, National Department of Neurosurgery, 1210 Luxembourg City, Luxembourg. ²Medical Faculty, Saarland University, E66421 Homburg (Saar), Germany. ³University of Luxembourg, Luxembourg Center for Systems Biomedicine, 4362 Esch-sur-Alzette, Luxembourg. ⁴Luxembourg Institute of Health, 1445 Strassen, Luxembourg. ⁵Laboratoire National de Santé, Luxembourg Center of Neuropathology, 3555 Dudelange, Luxembourg. ⁶These authors contributed equally: Finn Jelke and Giulia Mirizzi ✉email: hertel.frank@chl.lu

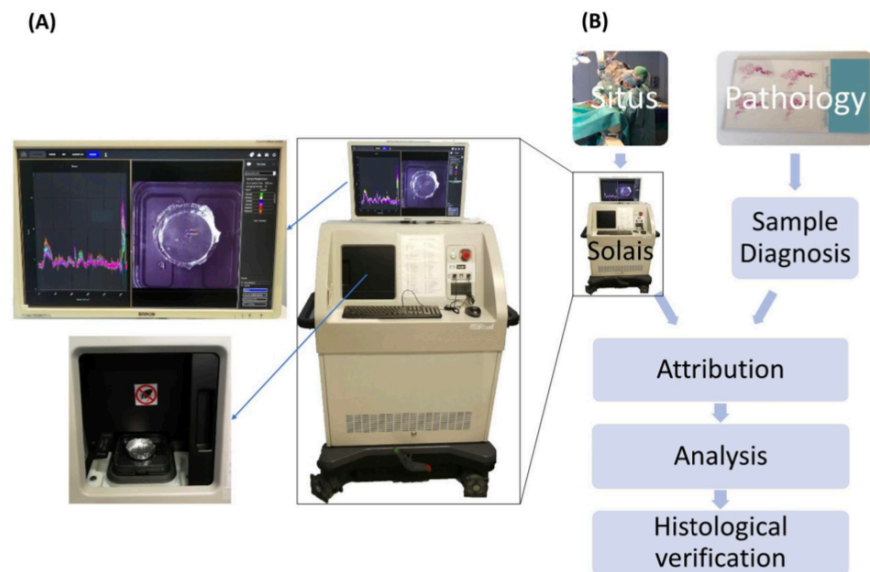


Figure 1. (A) Spectroscopic data acquisition and visualization system with robotized measuring spot navigation (Solais, Synaptive, Toronto, Canada). Upper left: Computer screen with the spectral curves on the left side and the white-light image on the right side. Lower left: Shows the robotized measurement chamber. (B) Flow chart of data flow.

effect). The resulting wavelength shift is characteristic for the vibrational mode of the underlying molecule. Thereby, heterogeneous tissues with a huge diversity of molecules result in characteristic complex spectra as a function of their biochemical compositions²³. With Raman Microscopy, a differentiation between snap-frozen meningioma tumor tissue and normal dura mater tissue was reported²⁴. Even RS of blood samples alone was described as suitable to identify meningioma patients by detection of specific spectra features²⁵. Several recent studies have demonstrated the potential of RS in oncologic diagnostics^{9,11,24–26}. However, there has been no report on the intraoperative application of RS for the diagnostics of meningiomas by help of macroscopic samples. In contrast to microscopic RS-techniques, non-microscopic RS could be used in situ without any further tissue processing. Handheld probes suited for intraoperative neurosurgical use of RS have been recently developed¹⁴. Therefore, this technology bears the potential for direct intraoperative resection control.

The Raman spectrometer applied in this paper (Solais, Synaptive, Toronto, Canada) offers the possibility to document in a fully robotized manner the defined measuring points with their exact coordinates on the tissue sample. The system is applicable without any kind of additional histology or tissue processing during the surgical procedure. After integrating it into a handheld probe, it could be used in the surgery cavity itself to indicate tumor borders.

Materials and methods

Applying the Solais™ Raman spectrometer intraoperatively, we take a close look on meningioma and healthy meningeal tissue and compare their Raman spectra. We use dimension reduction and classifier algorithms such as the t-distributed stochastic neighbor embedding (tSNE) and support vector machine (SVM) classifier^{27,28} for our analysis. Finally, we test the clinical applicability of our trained classifier on an extra sample consisting of dura mater and meningioma. The image thereof is superimposed by a tumor heat map generated by the trained classifier.

Intraoperative Raman spectrometry. The device used in our study enables robotized measuring spot navigation, spectral data acquisition and visualization in one unit (Solais, Synaptive, Toronto, Canada) (Fig. 1A). The system comprehends a movable stage, on which the sample can be placed and a visible-light-camera for the measuring point documentation. Furthermore, the measuring device is equipped with a 785 nm laser source operating at 50 mW and an optical coherence tomography (OCT) instrument. A coordination system enables to relocate retrospectively recorded measuring points in the visible light images (VLI) in a precise and reliable way. The data is acquired using an aluminum background due to its negligible inherent Raman spectrum. The average accumulation time was between 800 and 2000 ms with 6 to 30 acquisitions to enhance the signal-to-noise ratio.

Meningioma subtype	Patients	Patient's (n; %)		Measuring points (n; %)	
		Training set	Validation set	Training set	Validation set
Pure tumor tissue					
Transitional meningioma	13	10 (76.9%)	3 (23.1%)	171 (74.7%)	58 (25.3%)
Meningiothelial meningioma	19	15 (78.9%)	4 (21.1%)	197 (78.5%)	54 (21.5%)
Atypical meningioma	4	4 (100%)	0	62 (100%)	0
Fibrous meningioma	6	6 (100%)	0	69 (100%)	0
Meningioma, not otherwise specified	2	2 (100%)	0	20 (100%)	0
Secretory meningioma	1	1 (100%)	0	14 (100%)	0
Subtotal "MGMT"		23 (88.5%)	3 (11.5%)	336 (85.3%)	58 (14.7%)
Healthy dura mater	22	16 (72.7%)	6 (27.3%)	128 (79.0%)	34 (21.0%)
Tumor infiltration zone	Vide supra	Vide supra		371 (80.7%)	89 (19.3%)
Verification sample	1	1		108	
Total				1268	

Table 1. Data overview. Three classes were defined: Unequivocal meningioma tumor tissue, healthy dura mater and tumor-infiltrated dura mater samples. The data was split up in a training and validation set. The percentages indicate the corresponding portions of samples and measuring points, subdivided in the different tissue types. Upper table part: Meningioma samples. Middle table part: Origin of the probed healthy dura mater samples. Lower table part: Meningioma-infiltrated dura mater samples. Closing line: Total numbers of patients, samples and measuring points. Notice that, the infiltration zone samples belong to patients that were already considered in the other classes. The kept out surgical-site-simulating verification sample was of atypical meningioma tissue origin and was used for the subsequent classifier mapping study. Significant values are in bold.

For each spectrum, the Solais™ records 1603 single values, which are non-linearly mapping to a wavenumber range between 314 and 2994 cm^{-1} with an average resolution of 1.67 cm^{-1} .

Patient data. The INSITU study, Nr. 201804/08, was approved by the 'Comité National d'Ethique de Recherche' (CNER), the national ethics board of Luxembourg, and is handled accordingly to the 'EU General Data Protection Regulation (GDPR)' law from august 1st, 2018 and the study was in accordance with WMA Declaration of Helsinki-Ethical principles for medical research involving human subjects²⁹. Each recruited patient gave written informed consent.

Table 1 summarizes the statistics of all 59 patients, 1273 measuring points of 223 samples. Percentages in parentheses correspond to the training or validation set portions within the totality of the samples or the measuring points. We analyzed meningioma tissue from 48 patients as well as non-infiltrated dura mater from 11 patients of the same group. Dura mater samples were further analyzed from 11 patients that were operated for other pathologies (1 astrocytoma, 1 oligodendroglioma, 2 glioblastomas, 1 leiomyosarcoma, 5 metastases, 1 schwannoma). Within the meningioma group, 13 (36%) patients had transitional, 13 (36%) meningiothelial, 4 (11%) atypical, 4 (11%) fibrous, 1 (3%) not-otherwise-specified and 1 (3%) secretory meningioma. One appropriate anaplastic meningioma sample with macroscopically visible transition from tumor to dura mater was selected for additional histopathological verification as well as for testing the clinical applicability. Therefore, it was densely sampled with 108 individual RS measuring points.

Data acquisition, labelling and analysis. Figure 1B illustrates the workflow of the study. The tissue is collected intraoperatively. It is kept humid with physiological saline to avoid any tissue destruction due to drying. Before measuring, the tissue is not modified by any further fixation methods, neither chemically (e.g., formalin-fixed, paraffin embedded) nor physically (like cryopreservation). Samples were analyzed within 20 min after excision. The sample is then put on an aluminum dish, which is placed afterwards on the stage inside the Solais™. The output of the Raman-scan are the spectral curves corresponding to the tracked measuring points on the VLI. The tissue samples are afterwards stored, separately, in a formalin solution and sent for neuropathologic analyses. The detailed pathology report allows us to attribute the exact sample diagnosis to every spectrum with tags, considering the major tumor diagnosis and more detailed tissue properties. To avoid biases, the neuropathologist is blinded to the results of RS. The described procedure of the sample acquisition and measurement allows exact retracement and is relatively quick and non-destructive.

Data labelling and unsupervised analysis. For analytical purposes, the collected Raman spectra are examined with a custom-made MATLAB™ software. The Solais-preprocessed data (background removal, Savitzky Golay filtering) are checked for artefacts with the aid of an (in house designed) graphical user interface, called Raman-Labeler. Outliers and cosmic ray artifacts were removed and excluded from further analysis. The diagnostic information from the pathological analysis of tissue samples is linked to the spectra by manually assigning appropriate tags to each Raman spectrum. Next step is the spectral analysis of the pathologically defined groups.

Unsupervised learning techniques are employed for exploratory analyses, applying tSNE²⁷ as a dimension reduction cluster visualization tool.

Supervised machine learning classification. Before classifier training, the global data is split up in a training and a test set in an approximate ratio of 5:1, considering a patient-wise stratification and equilibrated acquisition parameters for both sides. Both sets have been carefully separated throughout the process avoiding any potential confounding variables. Importantly, the results are robust to the way of splitting (patient-wise or random split) and no pre-processing is required, indicating a high natural separability between MGM and DM. The tSNE was created with the training data set only. Supervised learning is carried out using a support vector machine (SVM) classifier²⁸ to predict the class labels (MGM or Dura) from the spectra. For visualization of the trained classifier performance, the VLI of a tissue sample can be overlaid with a posterior class probability heat map output of the classifier. As a case study to determine the suitability in larger tissue contexts, a large representative infiltration zone sample is analyzed. After Raman acquisition, this sample was formalin-fixed, paraffin-embedded and sliced into 21 consecutive hematoxylin & eosin (H&E) sections. Fiducial markers in the form of incisions guide the exact orientation. Because of the uneven sample-surface, the single sections were stacked and fused to map the entire sample with a surface profile. By superimposing the reconstructed surface H&E image with the VLI of the Raman acquisition, the individual RS-scanned points can be validated on a histological level (Fig. 5). The obtained composition image is overlaid with the classifier heat map of the meningioma probability. This way, the result of the classifier can be directly compared to the histology. Given the size of the specimen that is comparable with a surgical site of interest, this approach demonstrates the suitability for intraoperative use.

Ethics approval. The INSITU study, CNER Nr. 201804/08, is approved by the 'Comité National d'Ethique de Recherche' (CNER) on 2018-07-13 and is handled according to the law, state 1st august 2018 'EU General Data Protection Regulation GDPR'³¹, and to the WMA Declaration of Helsinki-Ethical principles for medical research involving human subjects. Each recruited patient gives a written informed consent.

Results

Exploratory data analysis. Figure 2 shows the average Raman spectra of all meningioma subtypes, as well as of dura mater. Differences between normal dura mater and the meningioma subtypes can be observed in the entire spectrum as well as in selected spectral subregions (Fig. 2B–D). The meningioma subtypes share most spectral characteristics when compared to dura mater. It is therefore possible to include all analyzed subtypes into a single class to build the classifier. The surgeon does not need to know the subtype prior to surgery in order to make use of this technique. Reduction to two dimensions using tSNE in Fig. 3 shows two well separable clusters. The first one corresponds to the dura mater measuring points (colored in red), whereas the second one includes all meningioma subtypes (multiple color-coded, except red). This clustering can be reached by the analysis of either the entire spectrum (Fig. 3A) in the high wavenumber region (HWNR) from 2800 to 3000 cm^{-1} (Fig. 3B) or using distinct peaks that are different between the entities (Fig. 3C). We used samples for the classifier training and validation that were homogenous in nature and either only tumor or only dura mater. For verification, we included infiltration zone (Suppl. Figs. S3 and S5) and found that those also clustered with either of the two described clusters in all three spectral sub-analyses.

Spectral difference analysis. We next wanted to know which areas of the spectrum show significant differences and what may be the underlying tissue composition. Figure 4 quantifies the differences of normalized mean meningioma vs. mean dura spectra. The significantly different Raman shifts, based on a p-value of $p \leq 0.01/1603 = 10^{-6}$ (Bonferroni-corrected Wilcoxon-Mann-Whitney test), are highlighted in yellow. The high wavenumber region (HWNR) between 2800 and 3000 cm^{-1} shows large and consistent differences between the groups. This area corresponds to the aromatic and aliphatic hydrogens in carbohydrates, indicating differences in the relation of sugar to fatty acids and therefore the relation of cytoplasm to cell membrane, cell size and cell density^{20,30}. A tSNE computed on this region leads to a good separation between tumor tissue and dura mater (Fig. 3B).

Several peaks that are characteristic for collagen (815, 855, 876, 938, 1003, 1033, 1250, 1319, 1450 and 1663 cm^{-1})³¹, are of higher intensity in dura mater compared to the meningioma spectra. In fact, if a tSNE clustering is performed solely based on these peaks, meningioma and dura mater separate well (see Fig. 3C). Therefore, the differences in collagen content are an important distinctive feature in the spectral analysis as it is in histopathology.

Machine learning based tissue classification. In order to train a classifier for tissue discrimination, disjoint classes had to be established. Samples need to be pure in that they do not contain infiltration zones. The first class corresponds to the pure meningioma samples, including all subtypes, and the second represents healthy dura mater. After exclusion of spectra altered by clear cosmic ray artifacts, the test set, the infiltration zone samples and the sample later used for a detailed histological case study, N = 529 spectra (422 meningioma, 107 dura mater spectra) remained for classifier training with a linear support vector machine (Suppl. Table S2). The classification was validated twice, once using fivefold-cross-validation from the full spectra (1603 features per Raman spectrum) and afterwards with the external test set, created by considering a patient-wise stratification.

For the fivefold cross validation, a validation set containing 1/5th of the randomized spectra was split from the data, and the classifier was trained on the remaining 4/5th of the data. The classifier performance was then evaluated on the held-out unseen test set. This procedure was repeated 5 times until all data were used once for

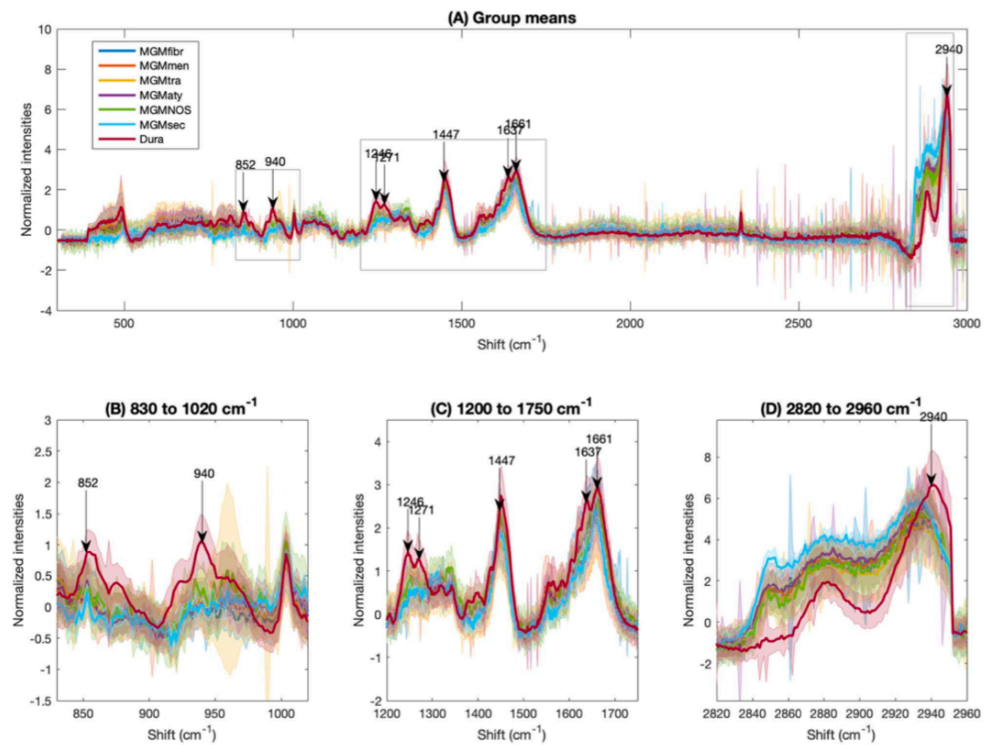


Figure 2. (A) Individual average spectra and standard deviation of meningioma subtypes and of dura mater. Based on 47 measuring points of fibrous meningioma (MGM_fibr, dark-blue), 110 of meningeothelial meningioma (MGM_men, orange), 159 of transitional meningioma (MGM_tra, yellow), 4 of secretory meningioma (MGM_sec, light blue), 56 of atypical meningioma (MGM_aty, purple), 25 of NOS-meningioma (MGM_NOS, green) and 117 of dura mater (Dura, scarlet). The spectra were z-score normalized. (B) to (D): Zoomed-in subintervals with focus on the spectral differences between the different meningioma subtypes and dura mater. (B) Subintervals from 830 to 1020 cm^{-1} , (C) from 1200 to 1750 cm^{-1} , (D) from 2820 to 2960 cm^{-1} . The arrows in (A) to (D) represent the distinctive peaks between meningioma and dura mater, partially in line with the collagen spectrum³⁸.

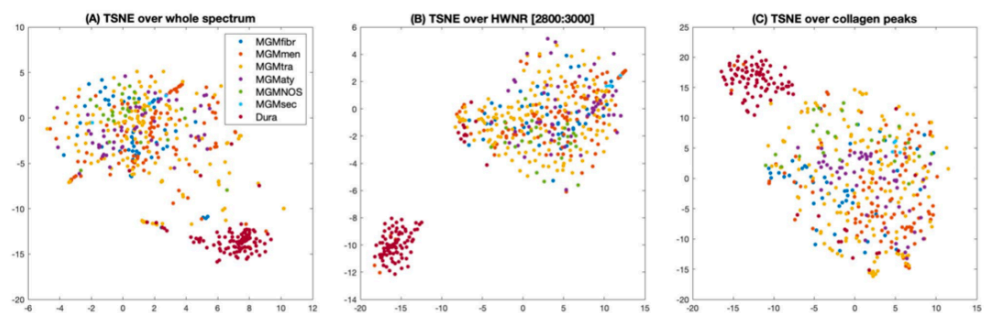


Figure 3. The tSNE-Cluster, based on the training data set, of meningioma subtypes and dura mater. The color-code is the same as in Fig. 2. (A), tSNE-Cluster of pathologically secured diagnoses over entire Raman spectrum of the chosen subclasses. (B) tSNE Cluster of pathologically approved diagnoses over high-wavenumber region (HWNR), interval 2800 cm^{-1} to 3000 cm^{-1} . (C) tSNE Clusters based on collagen peaks.

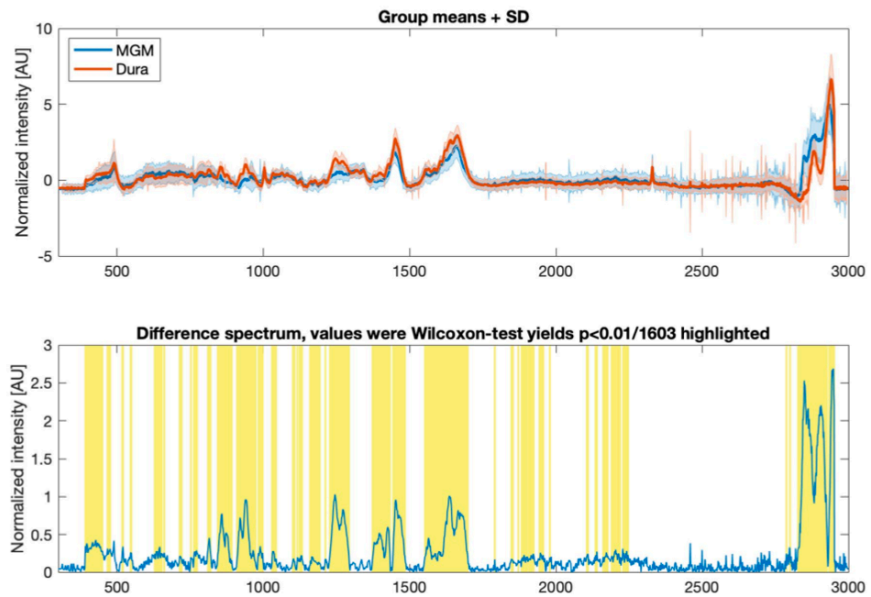


Figure 4. Top: Average spectra of all normalized (z-score normalized) meningioma and dura mater measurements; Bottom: Absolute difference spectrum of the previously plotted average spectra. Significant differences, calculated using Wilcoxon-Mann-Whitney-U test (Bonferroni-corrected p-value, resulting in $p \leq 0.01/1603 = 10^{-6}$), are highlighted in yellow.

testing. The performances of the optimized classifier on the cross-validated dataset are $96.06 \pm 0.03\%$ sensitivity and $95.44 \pm 0.02\%$ specificity (for ROC and PR-curves see Suppl. Fig. S4). The validation with the hold-out external validation data set yielded accuracy values of 100% for sensitivity and 93.97% for specificity.

While the training of the classifier relies on small samples containing only one class of tissue, the tool shall be used on larger specimens with mixed content, ideally in situ at a later point. Therefore, we verified the classifier on a histological level with a tissue sample consisting of tumor tissue as well as dura mater, resembling the situation in situ (Fig. 5). Macroscopically, it is impossible to distinguish tumor tissue reliably on this particular sample, however the surgeon needs histological precision of the sample's nature. The sample was systematically scanned point-by-point and sectioned in the same orientation afterwards. The surface was reconstructed from serial scans and histologically assessed. The classifier identified the tumor, as well as the dura reliably (sensitivity 93.0% and specificity 89.7%). In the infiltration zone, some measurements would be classified either as dura or tumor. Both classes were intermingled accordingly, resulting in some misclassified points where an exact retracement was not possible on the histological section.

Discussion

In tumor resection, there is a need for a non-destructive intraoperative tool to differentiate between tumor and healthy tissue in surgical disciplines. In meningioma surgery, an important challenge in this context is the differentiation between tumor and healthy non-infiltrated dura mater. Over the last decades, the potential of RS and also of stimulated Raman scattering microscopy for this issue has been increasingly recognized. Koljenovic et al. yield an accuracy of 1.0 for the detection of meningioma infiltration areas within dura mater by Raman microspectroscopy²⁴. Krafft et al. apply a similar spectroscopic method comparing it with IR spectroscopy. They identify tumorous features of meningiomas extracted from a Raman map⁸. Focusing on the Raman resonance effect, Zhou et al. are likewise able to discriminate between tumorous and healthy meningeal tissue with a sensitivity of 0.91²⁶. Aguiar et al. are able to produce similar results by applying conventional near-infrared RS¹¹. All aforementioned studies have in common, that their tissue specimens are cryopreserved and/or histologically processed before the measurements. Orringer et al. developed a prototype for fiber-laser-based stimulated Raman scattering microscopy which combines the advantages of microscopy with RS-based tissue contrast labeling³².

Our study shows that RS alone can properly discriminate between meningioma and dura mater with a sensitivity of $96.06 \pm 0.03\%$ and a specificity of $95.44 \pm 0.02\%$ for internal fivefold cross validation and 100% and 93.97% if validated with an external test set. We investigate intraoperative spot measurements on native samples without any kind of tissue processing. In contrast to Raman microscopy, the method can give direct feedback on tumor origin relying on the assessment of the trained classifier which does not require the presence of a

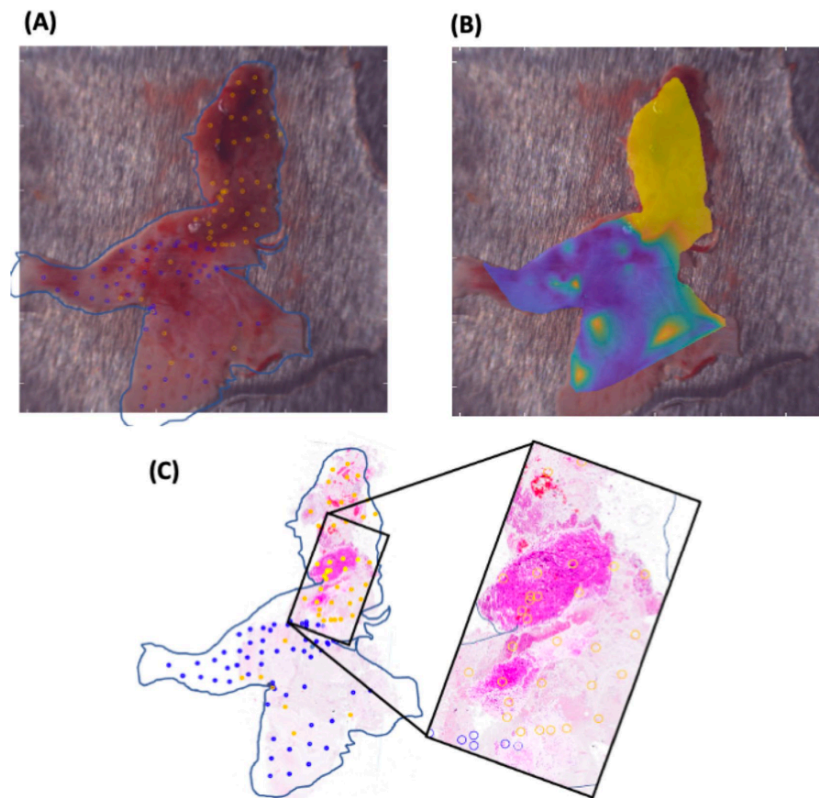


Figure 5. Histological verification of the meningioma-dura mater-classifier. (A) Visible Light Image (VLI) exported from the Solais with engraved measuring points and with a retraced frame. (B) Same VLI superimposed by a classifier heat map with color scale ranging from blue (not meningioma tissue) to yellow (meningioma). The greenish parts are the transition zones between the meningioma tissue and dura mater. (C) Superposition of 21 hematoxylin & eosin stained slides of the same sample with the tumor infiltration zoom-in window and measuring point specifications.

neuropathologic expert being familiar with microscopic analyses. This could potentially be a helpful tool for the surgeon for intraoperative resection control.

Furthermore, we analyzed the statistically significant spectral differences between meningioma and dura mater with a special focus on the biochemical composition. Characteristic peaks for collagen show a higher intensity in the dura mater spectra compared to those of meningioma and a simple TSNE plot, based only on the collagen peaks, shows distinct clusters for both entities. We conclude that the collagen content is an important distinctive feature between meningioma and dura mater, also discussed by Protasoni et al.³³. A closer look into the possible differentiation of meningioma-subtypes based on their collagen content should be examined in further studies.

We also examine the RS spectra with respect to the different meningioma subtypes. With our classifier, we are not able to distinguish them. By using more sophisticated machine learning algorithms, it may be possible in the future to discriminate between the different meningioma subtypes and also use the tool for tumor diagnostics. However, the fact that the meningioma subtypes share many spectral features when compared to dura mater is advantageous for the purpose of the tool as outlined here, as it is not critical to know the type of meningioma before analysis.

While metallic aluminum has a negligible Raman spectrum, its oxidized form shows a spectrum below 900 cm^{-1} ^{134,35}. We excluded this interval of small wavenumbers in our analyses as we noticed the influence especially in smaller samples. Other substrates with lower spectral interference exist, i.e., calcium fluoride (CaF_2) with only one Raman peak at 322 cm^{-1} ¹³⁶. CaF_2 is particularly suited for microscopic applications as it is translucent. In this study, we chose aluminum for its low intrinsic signal and good availability in the surgery room.

If applied on the surgical-site-simulating verification sample, our trained classifier was able to distinguish tumor from healthy areas of the sample that were different in histology but indistinguishable macroscopically. Even small clusters of tumor cells inside the dura mater are identified by the classifier (Fig. 5). A classification of infiltration zone as dura based on a single spot measurement would be problematic. From the surgeon's view, the accuracy of the classifier depends on the desired information: For the single spot measurement the classifier can be assumed to be true regarding the nearly 100% sensitivity but for a spacious evaluation of the infiltration zone, the accuracy will decrease because of the inherent nature of the infiltration zone. The infiltration zone contains tumor cell clusters in widespread distances whereas the rest consists of healthy dura mater. The challenge will be to detect exactly these tumorous areas, which leads automatically to a higher number of needed measurements per area unit. With single measurements, taking no longer than a few seconds, the surgeon will be able to identify the pure tumor and dura mater regions. By measuring point-by-point the surgeon receives direct feedback on the dignity of the tissue and thus he discovers whether he needs to resect further at this site. For proper detection of the extent of the infiltration zone, the number of measurements needs to be increased in a systematic way. This can be achieved by systematic scanning of the surgery site and potentially assisted by a robot-navigated probe holder that is integrated into the neuronavigation system. Complete mapping of the infiltration zone cannot be achieved because the infiltration zone is always of a three-dimensional extent in space but the scan is performed on the surface only.

Conclusion

Since tumor residues are often the reason for recurrence/progression of meningiomas, an appropriate, fast and reliable intraoperative tool to discriminate between neoplastic and healthy meningeal tissue is crucial. In this study, we present a new intraoperative RS application without the need of preanalytical tissue processing. The method complements the neuropathological analysis and extends it into the surgery room. It is less time-consuming, can be applied by non-neuropathologically-specialized staff and is therefore less expensive. The application has the potential to be included into the daily neurosurgical routine in the near future to aid residue-free resection of tumors, e.g. meningiomas. To ensure a smooth transition from the 'classical' neuropathological method to RS-based tumor-identification and removal, the preliminary diagnosis gained with the spectroscopic classifier should always be verified by a neuropathologist and, of course, a contrasted CT or MRI shall be done afterwards to verify a Simpson grade I resection. Our future goal is to extend RS-based tumor detection to further neuronal tissue entities i.e. to glioblastomas. Macroscopic RS could also lead to biochemical insights in tumor biology, as a direct and non-destructive assessment of Raman active metabolites and structural elements can be recorded. This may help to identify the most suitable personalized therapy of meningiomas and to predict the effectiveness of upcoming target therapies in the future³⁷.

In summary, we show that Raman spectroscopy can differentiate macroscopically between meningioma and normal dura mater. This is verified by means of neuropathological histological assessment. A series of systematic scanning of the tissue surface can reliably identify the tumor as well as infiltrated tissue if enough scans are done per area unit. The classifier visualization design with an overlaid transparent heat map on the macroscopic image (Fig. 5) might be applicable for the fade-in into a surgical microscope in the future. In vivo, a robotic device might be used to aid in systematic scanning of the infiltration zone. For the direct application in the operating field, a hand-held RS probe (integrated in a neuronavigation system and/or in the surgical microscope) might be available in the future¹⁴.

Data availability

The ethical approval does not permit public sharing of data. Interested parties are invited to contact the corresponding author for individual options.

Received: 21 March 2021; Accepted: 25 November 2021

Published online: 08 December 2021

References

1. International Agency for Research on Cancer. *WHO Classification of Tumours of the Central Nervous System*. World Health Organization Classification of Tumours (International Agency for Research on Cancer, 2016).
2. DeMonte, F., McDermott, M. W. & Al-Mefti, O. *Al-Mefti's Meningiomas* (Thieme Medical Publishers Inc, 2011).
3. Whittle, I. R., Smith, C., Navoo, P. & Collie, D. Meningiomas. *Lancet* **363**, 1535–1543 (2004).
4. Rockhill, J., Mrugala, M. & Chamberlain, M. C. Intracranial meningiomas: An overview of diagnosis and treatment. *Neurosurg. Focus* **23**, 1–7 (2007).
5. Gupta, S., Bi, W. L. & Dunn, I. F. Medical management of meningioma in the era of precision medicine. *J. Neurosurg.* **44**, E3 (2018).
6. Perry, A. Meningiomas. In *Practical Surgical Neuropathology: A Diagnostic Approach* 259–298 (Elsevier, 2018).
7. Nanda, A. *et al.* Relevance of Simpson grading system and recurrence-free survival after surgery for World Health Organization Grade I meningioma. *J. Neurosurg.* **126**, 201–211 (2017).
8. Ramina, R. *et al.* Optimizing costs of intraoperative magnetic resonance imaging. A series of 29 glioma cases. *Acta Neurochir. (Wien)* **152**, 27–32 (2010).
9. Krafft, C., Sobottka, S. B., Schackert, G. & Salzer, R. Raman and infrared spectroscopic mapping of human primary intracranial tumors: A comparative study. *J. Raman Spectrosc.* **37**, 367–375 (2006).
10. Li, T. & Deng, P. Nuclear Magnetic Resonance technique in tumor metabolism. *Genes Dis.* **4**, 28–36 (2017).
11. Aguiar, R. P. *et al.* Discriminating neoplastic and normal brain tissues in vitro through Raman spectroscopy. *Photomed. Laser Surg.* **31**, 595–604 (2013).
12. Yu, M. *et al.* Deep convolutional neural networks for tongue squamous cell carcinoma classification using Raman spectroscopy. *Photodiagn. Photodyn. Ther.* **26**, 430–435 (2019).
13. Hollon, T., Lewis, S., Freudiger, C. W., Xie, X. S. & Orringer, D. A. Improving the accuracy of brain tumor surgery via Raman-based technology. *Neurosurg. Focus* **40**, 1–9 (2016).

14. Jermyn, M. *et al.* Raman spectroscopy detects distant invasive brain cancer cells centimeters beyond MRI capability in humans. *Biomed. Opt. Express* **7**, 5129 (2016).
15. Chen, P. H. *et al.* Automatic and objective oral cancer diagnosis by Raman spectroscopic detection of keratin with multivariate curve resolution analysis. *Sci. Rep.* **6**, 1–9 (2016).
16. Jermyn, M. *et al.* Intraoperative brain cancer detection with Raman spectroscopy in humans. *Sci. Transl. Med.* <https://doi.org/10.1126/scitranslmed.aaa2384> (2015).
17. Brozek-Pluska, B., Kopec, M., Niedzwiecka, I. & Morawiec-Sztandera, A. Label-free determination of lipid composition and secondary protein structure of human salivary noncancerous and cancerous tissues by Raman microspectroscopy. *Analyst* **140**, 2107–2113 (2015).
18. Kairdolf, B. A. *et al.* Intraoperative spectroscopy with ultrahigh sensitivity for image-guided surgery of malignant brain tumors. *Anal. Chem.* **88**, 858–867 (2016).
19. Bentley, J. N., Ji, M., Xie, X. S. & Orringer, D. A. Real-time image guidance for brain tumor surgery through stimulated Raman scattering microscopy. *Expert Rev. Anticancer Ther.* **14**, 359–361 (2014).
20. Abramczyk, H. & Imiela, A. The biochemical, nanomechanical and chemometric signatures of brain cancer. *Spectrochim. Acta. A* **188**, 8–19 (2018).
21. Zhang, J. *et al.* Accuracy of Raman spectroscopy in differentiating brain tumor from normal brain tissue. *Oncotarget* **8**, 36824–36831 (2017).
22. Yang, Y., Chen, L. & Ji, M. Stimulated Raman scattering microscopy for rapid brain tumor histology. *J. Innov. Opt. Health Sci.* **10**, 1–12 (2017).
23. Morris, M. D. & Mandair, G. S. Raman assessment of bone quality. *Clin. Orthop. Relat. Res.* **469**, 2160–2169 (2011).
24. Koljenović, S., Schut, T. B., Vincent, A., Kros, J. M. & Puppels, G. J. Detection of meningioma in dura mater by Raman spectroscopy. *Anal. Chem.* **77**, 7958–7965 (2005).
25. Mehta, K., Atak, A., Sahu, A., Srivastava, S. & Murali Krishna, C. An early investigative serum Raman spectroscopy study of meningioma. *Analyst* **143**, 1916–1923 (2018).
26. Zhou, Y. *et al.* Human brain cancer studied by resonance Raman spectroscopy. *J. Biomed. Opt.* **17**, 116021 (2012).
27. Van der Maaten, L. & Hinton, G. Visualizing data using t-SNE. *J. Mach. Learn.* **9**, 2579–2605 (2008).
28. Cortes, C. & Vapnik, V. Support-vector networks. *Mach. Learn.* **20**, 273–297 (1995).
29. Kong, H. & West, S. WMA declaration of Helsinki: Ethical principles for scientific requirements and research protocols. *JAMA* **310**, 2191–2194 (2013).
30. Carey, P. *Biochemical Applications of Raman and Resonance Raman Spectroscopies Molecular Biology* (Elsevier Science, Amsterdam, 1982).
31. Nguyen, T. T. *et al.* Characterization of type I and IV collagens by Raman microspectroscopy: Identification of spectral markers of the dermo-epidermal junction. *Adv. Biomed. Spectrosc.* **7**, 105–110 (2013).
32. Oringer, D. A. *et al.* Rapid intraoperative histology of unprocessed surgical specimens via fibre-laser-based stimulated Raman scattering microscopy. *Nat. Biomed. Eng.* **1**, 1–13 (2017).
33. Protasoni, M. *et al.* The collagenic architecture of human dura mater: Laboratory investigation. *J. Neurosurg.* **114**, 1723–1730 (2011).
34. Thomas, P. V., Ramakrishnan, V. & Vaidyan, V. K. Oxidation studies of aluminum thin films by Raman spectroscopy. *Thin Solid Films* **170**, 35–40 (1989).
35. Kerr, L. T., Byrne, H. J. & Hennelly, B. M. Optimal choice of sample substrate and laser wavelength for Raman spectroscopic analysis of biological specimen. *Anal. Methods* **7**, 5041–5052 (2015).
36. Gee, A. R., O'Shea, D. C. & Cummins, H. Z. Raman scattering and fluorescence in calcium fluoride. *Solid State Commun.* **4**, 43–46 (1966).
37. Brozek-Pluska, B. *et al.* Distribution of phthalocyanines and Raman reporters in human cancerous and noncancerous breast tissue as studied by Raman imaging. *Technol. Cancer Res. Treat.* **11**, 317–331 (2012).
38. Movasaghi, Z., Rehman, S. & Rehman, I. U. Raman spectroscopy of biological tissues. *Appl. Spectrosc. Rev.* **42**, 493–541 (2007).

Acknowledgements

We would like to thank the whole neurosurgical team at CHL, especially the neurosurgeons for their support. In addition, we would like to express our gratitude to the team of the LNS for the histological preparation of the samples. With special regards, we thank the Fondation Cancer for their generous financing of the project.

Author contributions

The study was designed by F.H., F.K. and A.H. F.J., G.M., R.S., F.K., G.K., K.K. and F.H. cared for the acquisition of samples and data. Coding and machine learning was implemented by A.H. and L.M. F.J., G.M., F.K., A.H. and F.H. analyzed the data and searched for the right interpretation. The tissue samples were histologically processed by J.G. and the subsequent pathological diagnostics was achieved by M.M. The entire project was coordinated and supervised by F.H., M.M., F.K. and A.H. F.J. and G.M. wrote the first draft and share co-first authorship for this paper. All authors contributed to the final draft.

Funding

This work was enabled by the Fondation Cancer Luxembourg supporting FKB, AH and FH. MM received funding from the Luxembourg National Research Fund (FNR PEARL P16/BM/11192868).

Competing interests

The authors declare no competing interests.

Additional information

Supplementary Information The online version contains supplementary material available at <https://doi.org/10.1038/s41598-021-02977-7>.

Correspondence and requests for materials should be addressed to F.H.

Reprints and permissions information is available at www.nature.com/reprints.

Publisher's note Springer Nature remains neutral with regard to jurisdictional claims in published maps and institutional affiliations.



Open Access This article is licensed under a Creative Commons Attribution 4.0 International License, which permits use, sharing, adaptation, distribution and reproduction in any medium or format, as long as you give appropriate credit to the original author(s) and the source, provide a link to the Creative Commons licence, and indicate if changes were made. The images or other third party material in this article are included in the article's Creative Commons licence, unless indicated otherwise in a credit line to the material. If material is not included in the article's Creative Commons licence and your intended use is not permitted by statutory regulation or exceeds the permitted use, you will need to obtain permission directly from the copyright holder. To view a copy of this licence, visit <http://creativecommons.org/licenses/by/4.0/>.

© The Author(s) 2021

13 Curriculum vitae

Aus datenschutzrechtlichen Gründen wird der Lebenslauf in der elektronischen Fassung der Dissertation nicht veröffentlicht.

Tag der Promotion: 30.01.2024

Dekan: Univ.-Prof. Dr. med. Michael D. Menger

Berichterstatter: PD Dr. med. Frank Hertel

Prof. Dr. med. Joachim Oertel

Prof. Dr. med. Frank Schmitz